

© 2014

Minh T. Vu

All Rights Reserved

DENSIFICATION AND CHARACTERIZATION OF TRANSPARENT  
POLYCRYSTALLINE SPINEL PRODUCED BY SPARK PLASMA SINTERING

By

MINH T. VU

A dissertation submitted to the  
Graduate School – New Brunswick  
Rutgers, The State University of New Jersey  
in partial fulfillment of the requirements

for the degree of

Doctor of Philosophy

Graduate Program in Materials Science and Engineering

written under the direction of

Professor Richard A. Haber

and approved by

---

---

---

---

New Brunswick, New Jersey

October 2014

ABSTRACT OF THE DISSERTATION  
Densification and Characterization of Transparent Polycrystalline Spinel

Produced by Spark Plasma Sintering

by MINH T. VU

Dissertation Director:

Richard A. Haber

Polycrystalline transparent magnesium aluminate spinel ( $\text{MgAl}_2\text{O}_4$ ) is an important optical material due to its good mechanical properties combined with a high light transmittance over the visible and near infrared wavelength range. It shows promise for many applications including high energy windows and light-weight armors. Being a difficult-to-sinter material, the fabrication of transparent spinel often requires a pressure-assisted sintering method with the use of a sintering aid. Thanks to its high heating rate combined with a moderate pressure, spark plasma sintering (SPS) is capable of producing a fine-grain spinel without using a sintering aid. The densification dynamics of spinel in SPS processing and its influence on the transmittance and the microstructure of the material were of great interest.

Early in the course of study, it was determined that the mobility of the magnesium ions in spinel under an electric field at elevated temperatures was the major factor that caused discoloration in SPS-processed spinel. Controlling the SPS heating rate and soaking time after the sample reach 60% of its theoretical density was the decisive factor in attaining a high transmittance and minimizing discoloration. Later it was found that increasing the SPS processing time would diminish the transmittance of spinel in the visible

region, and at the same time exacerbated discoloration. Based on these observations, the SPS conditions for transparent spinel were determined and optimized.

Enhancement of the hardness of spinel by doping was also studied. A simple surface precipitation process was developed to coat alumina onto the spinel particles. Doping caused a reduction the transmittance of the material in the visible region but inserting an alumina layer between the graphite die and the powder compact to be sintered helped to solve this problem. By doping, the hardness of the material was increased by 3 – 6% compare to other SPS-processed spinels, and by about 8.5% compare to HIP-processed spinel of the same grain size.

The findings of this dissertation explained why SPS processed spinel could not reach its theoretical transmittance in the visible wavelength range. Simple solutions to minimize discoloration of SPS-processed spinel were determined. The experimental designs served as a platform to explore potential densification dynamics and interactions of other nonconductive ceramic materials in SPS processing.

## **Acknowledgement**

This work was carried out in the Department of Materials Science and Engineering at Rutgers University in the period of October 2010 to October 2014. I would like to thank people who have given me support, advice, encouragement, and friendship during my PhD journey. Without them this dissertation would have not been possible.

I would like to express my deepest appreciation to my advisor Professor Richard A. Haber for his invaluable mentorship and support, and for giving me the opportunity to work on such a fantastic PhD project. I would like to thank all other members of my dissertation committee, Professor Hasan Gocmez, Professor Richard Lehman, and Dr. Vladislav Domnich, for their advice and in-depth discussion throughout the years.

I would like to thank all the professors and staffs working in the Department of Materials Science and Engineering for creating a wonderful working-learning environment. I would particularly like to thank Professors Danforth, Harrington, Cosandey, Greenhut, Matthewson, Mann, and Dr. Klein for their guidance and help.

I gratefully appreciate the TEM work provided by Mahsa Sina at Rutgers University, and Dr. Kelvin Xie at Johns Hopkins University.

I would like to thank all members of Prof. Haber's group, past and present, for being there with me during my journey: Steve Miller, Mihaela Jitianu, Sara Reynaud, Fabio Nicodemi, Steve Mercurio, Steve Bottiglieri, Steve Baggenski, Dan Maiorano, Doug Slusark, Bob Bianchini, Rob Wadams, Fatih Toksoy, Vince DeLucca, Nick Ku, Tyler Munhollon, Metin Ornek, Anthony Etzold, Kanak Kuwelkar, Azmi Celik, Chawon Hwang, Sukanya Murali, and Yong Gao. I would like to give my special thanks to Vince DeLucca, who was always there when I needed help with the NDE and trouble shooting of the SPS and

other machines. Special thanks also go to Michelle Sole and Laura Chirichillo who offered invaluable support and deep understanding, and have been managing a wonderful family-like atmosphere in the group.

I sincerely thank the undergraduate students, Andrew Lichtenstein, Sameer Dharsee, Denise Orthner, Daniel Mohrfeld, and David Manoukian, who were lab technicians working along with me in this project.

I would like to acknowledge the financial support of the Vietnam Ministry of Education and Training for my first two years, and the financial support of the Center for Ceramic Research, an NSF funded research center, for the remainder of my time at Rutgers University.

My deepest appreciation goes to my parents and my brother, who always support and encourage me.

## Table of Contents

Abstract of the dissertation .....	ii
Acknowledgement .....	iv
List of Tables .....	x
List of Figures .....	xi
1. Introduction and literature reviews .....	1
1.1. Motivation.....	1
1.2. Magnesium aluminate spinel .....	4
1.2.1. History.....	4
1.2.2. MgO – Al <sub>2</sub> O <sub>3</sub> binary phase diagram .....	7
1.2.3. Crystal structure .....	9
1.2.4. Electronic structure .....	12
1.2.5. Optical properties.....	13
1.2.6. Mechanical properties.....	16
1.2.7. Electrical properties .....	20
1.3. Spinel powder synthesis.....	23
1.3.1. Fabrication of spinel powder .....	23
1.3.2. Powder properties and their influences on the fabrication and the properties sintered spinel .....	25
1.3.3. The availability and qualities of high-purity spinel powder in the current market .....	29
1.4. Fabrication principles for the production of ceramics with superior mechanical properties .....	30

1.5. Sintering additives and methods of introduction .....	32
1.5.1. Sintering additives in fabrication of transparent spinel .....	33
1.5.2. Methods of introducing sintering additives to spinel powder.....	35
1.6. Densification of transparent polycrystalline spinel.....	39
1.6.1. Densification of polycrystalline ceramics.....	39
1.6.2. Sintering kinetics of spinel.....	45
1.6.3. Sintering techniques.....	46
2. Experiment design .....	57
2.1. Selection of the starting powder and other chemicals .....	57
2.1.1. Spinel powder .....	57
2.1.2. Other chemicals .....	60
2.2. Optimization of the SPS conditions to produce transparent spinel.....	60
2.3. The process of coating alumina onto spinel particles by surface precipitation .....	64
2.4. Determine the effects of HIP post SPS on the properties of spinel .....	67
2.5. Sample preparation .....	67
2.5.1. Cleaning, grinding and polishing.....	67
2.5.2. Etching .....	69
2.5.3. Sputter coating .....	69
2.6. Characterization techniques.....	70
2.6.1. Particle size analysis .....	70
2.6.2. Differential scanning calorimetry (DSC) and thermogravimetric analysis (TGA).....	71
2.6.3. Density .....	72

2.6.4.	Spectrophotometry .....	73
2.6.5.	Fourier transform infrared spectroscopy.....	74
2.6.6.	X-ray diffraction (XRD) .....	75
2.6.7.	Scanning electron microscopy and energy dispersive spectroscopy (SEM/EDS) .....	77
2.6.8.	Transmission electron microscopy (TEM) .....	78
2.6.9.	Micro-indentation hardness .....	78
2.6.10.	Laser Raman spectroscopy .....	80
2.6.11.	Acoustic evaluation of the elastic properties .....	81
3.	Determination and optimization of the SPS condition for transparent spinel.....	83
3.1.	Characterization of the starting powder .....	84
3.2.	Effects of high SPS heating rate on the properties of spinel.....	88
3.3.	Determination of the critical sintering temperatures .....	103
3.4.	Effects of the SPS heating rate on the properties of the sintered spinel .....	107
3.5.	Effects of the dwell time on the properties of the SPS-processed spinel.....	115
3.6.	Effects HIP post SPS on the properties of SPS-processed spinel .....	121
3.7.	Summary .....	123
4.	Effects of doping on the properties of SPS-processed spinel .....	124
4.1.	Characterization of the alumina doped spinel powder.....	124
4.2.	Characterization of the doped samples after SPS processing .....	131
4.2.1.	Discoloration and transmittance .....	131
4.2.2.	XRD analysis .....	134
4.2.3.	Microstructural properties.....	135

4.2.4. Microindentation hardness.....	139
4.2.5. Laser Raman analysis .....	142
4.2.6. Ultrasound non-destructive evaluation (NDE) .....	146
4.3. Summary .....	147
5. Conclusions.....	148
6. Future work.....	150
References.....	152

## List of Tables

Table 1. Examples of the transmittance of spinel from different sources. ....	16
Table 2. Mechanical properties of spinel. ....	17
Table 3. Commercially available spinel powder for optical-grade spinel. ....	30
Table 4. Comparison of the sintering conditions and the properties of a hot pressed spinel and a spark plasma sintered processed spinel. ....	56
Table 5. Physical properties and chemical analysis of the main impurities in Baikowski spinel powders. * .....	58
Table 6. Chemicals used in the syntheses. ....	60
Table 7. Properties of samples SPS at various heating rates. ....	90
Table 8. Average relative density of the spinel samples during SPS processing. ....	106
Table 9. Effects of the heating rate on the sample properties .....	115
Table 10. Effects of the heating rate and the dwell time on the sample properties .....	120
Table 11. Properties of doped samples. ....	135
Table 12. Comparison of the obtained hardness with the data available in the literature. ....	140
Table 13. The Al <sub>2</sub> O <sub>3</sub> doping amounts, SPS temperatures and annealing temperatures for spinel. ....	142
Table 14. Comparison of the vibrational frequencies of the SPS spinel samples.....	143
Table 15. The A-scan measurement of the elastic properties for SPS spinel samples ...	146

## List of Figures

Figure 1. Binary phase diagrams of the MgO-Al <sub>2</sub> O <sub>3</sub> system. (a) MgO-rich spinel solid solution is not formed at elevated temperature. <sup>4</sup> (b) MgO-rich spinel solid solution is formed at elevated temperature. <sup>66</sup> .....	8
Figure 2. Illustration of the arrangement of the Mg, Al, and O atoms in a spinel unit cell. ....	10
Figure 3. Temperature dependence of the electrical conductivity of a nominally pure MgAl <sub>2</sub> O <sub>4</sub> single crystal. <sup>102</sup> .....	21
Figure 4. Schematic diagram of an agglomerate consisting of dense, polycrystalline primary particles. <sup>108</sup> .....	27
Figure 5. Schematic section through a growing MgAl <sub>2</sub> O <sub>4</sub> layer. <sup>133</sup> .....	35
Figure 6. Schematics of (a) ordered mixing and (b) random mixing. <sup>137</sup> .....	37
Figure 7. Changes in pore shape and size during sintering. Changes in pore shape do not necessarily require shrinkage. <sup>143</sup> .....	40
Figure 8. Alternate paths for matter transport during the initial stage of sintering. ....	41
Figure 9. Schematic of grain growth. (a) Structure of boundary; (b) energy change for atom jump. <sup>143</sup> .....	43
Figure 10. Schematic drawing of grain boundaries migration. The numbers indicate the number of sides of each grain. The arrows indicate the directions in which boundaries migrate. From J.E. Burke. <sup>143</sup> .....	44
Figure 11. Schematic of the hot pressing process.....	49
Figure 12. The schematic of the SPS process (taken from Ceramic Industry Magazine <sup>169</sup> ) .....	52
Figure 13. Thermal Technology's spark plasma sintering system. ....	61
Figure 14. Temperature profiles settings of the initial SPS runs .....	63
Figure 15. Illustration of the loading in the die. (a) without the alumina protective layers; (b) with the alumina protective layers .....	67
Figure 16. Buehler mounting press and polisher. (a) SimpliMet® 1000 Automatic Mounting Press; (b) EcoMet 250 Grinder-Polishers with AutoMet 250 Power Heads (picture courtesy Buehler, An ITW Company).....	68
Figure 17. Electron Microscopy Sciences EMS 150T ES Turbo-Pumped Sputter Coater/Carbon Coater. ....	70

Figure 18. Malvern Mastersizer 2000 Light Scattering Particle Sizer with Scirocco Dry Powder Feeder (front left) and Hydro S Small Volume Wet Dispersion Cell (front right) accessories.....	71
Figure 19. Thermo Scientific Evolution 300 UV-Vis spectrophotometer (picture courtesy Thermo Scientific). .....	73
Figure 20. Mattson Instruments Galaxy series FTIR 5000 spectrophotometer .....	74
Figure 21. PANalytical X-ray Diffractometer. ....	75
Figure 22. Zeiss Sigma field emission scanning electron microscope .....	77
Figure 23. Leco M-400-G3 micro-indentation hardness tester.....	79
Figure 24. Renishaw InVia Confocal Micro-Raman Spectrometer.....	81
Figure 25. Single transducer ultrasound system for measuring the elastic properties of the dense samples.....	81
Figure 26. FESEM image showing the agglomerates of the as-received spinel powder..	84
Figure 27. X-ray diffraction pattern of the as-received powder .....	85
Figure 28. The dependence of the particle size distribution on the ultrasonication time.	86
Figure 29. The DSC and TGA curves of the as-received powder. The sample was heated at the heating rate of 10°C/min in a nitrogen atmosphere.....	88
Figure 30. Photographs of samples SPS at the heating rate of 100°C/min to a transition point and then at 2.5°C/min to 1400°C, with a 10 seconds hold at 1400°C. The samples had a thickness of about 3 mm, and were placed at 4 cm above the text. ....	89
Figure 31. In-line transmittance of samples SPS at the heating rate of 100°C/min to a transition point and then at 2.5°C/min to 1400°C, with a 10 seconds hold at 1400°C. Data was normalized to the transmittance at the thickness of 1.8 mm.....	90
Figure 32. Photograph showing the difference in color of the surface and the center of the sample SPS at the heating rate of 100°C/min with a 10 minutes hold at 1400°C.....	91
Figure 33. FESEM images of the sample heated at the rate of 100°C/min: (a) taken at the center of the sample; (b) taken at the top of the sample. ....	92
Figure 34. XRD patterns taken at the top and the center of the sample SPS at the heating rate of 100°C/min with a 10 minute hold at 1400°C in comparison with the XRD pattern of the as-received powder: (a) full pattern; (b) zoomed-in pattern at the k-alpha peak. ....	94
Figure 35. TEM images of the sample SPS at the heating rate of 100°C/min.....	96

Figure 36. DC power supply during SPS processing: (a) current, (b) voltage, and (c) power supply calculated from (a) and (b). .....	99
Figure 37. High resolution TEM micrographs taken at (a) a pore and (b) a grain boundary of the top of the sample SPS at the heating rate of 100°C/min to 1400°C with a 10 minute hold at 1400°C.....	102
Figure 38. The contraction of the spinel samples during SPS processing. ....	105
Figure 39. Photographs showing the appearance of samples heated at the rate of (a) 100°C/min, and (b) 10°C/min. The samples had a thickness of about 3 mm and were placed at 40 mm above the text. ....	106
Figure 40. In-line transmittance of the samples SPS at the heating rate of 100°C/min and 10°C/min. The data was normalized to the transmittance at the thickness of 1.8 mm. ..	107
Figure 41. Photographs of the spinel samples SPS at the heating rate of 100°C/min until 1100°C and then at (a) 10°C/min, (b) 5°C/min, (c) 2.5°C/min, and (d) 1.25°C/min until 1350°C with a 10 minute hold at 1350°C. The samples were placed at 40 mm above the text.....	108
Figure 42. Effects of the SPS heating rate on the transmittance spinel. ....	108
Figure 43. FESEM images of spinel SPSed at the heating rate of 100°C/min until 1100°C, and then at lower rates until 1350°C, with a 10 minute hold at 1350°C.....	109
Figure 44. The grain size and porosity distribution samples SPS at different heating rates. ....	110
Figure 45. FESEM images of the fractured surface of the sample SPS at the heating rate of 100°C/min until 1100°C, and then at 1.25°C/min until 1350°C with a 10 minute hold at 1350°C.....	111
Figure 46. X-ray diffraction of the SPSed samples showing peaks shifting compared to the as-received powder .....	112
Figure 47. Effects of the controlled heating rates on the transmittance of the spinel.....	113
Figure 48. The real-time change in thickness of the sample SPS at 2.5°C/min in the range of temperatures from 1100°C – 1350°C.....	114
Figure 49. Photographs showing the effects of the dwell time on the transparency of SPS spinel.....	117
Figure 50. SEM images showing the effects of the dwell time on the microstructure of SPS spinel.....	118

Figure 51. Illustration of the effects of the SPS dwell time on the transmittance of spinel. .....	119
Figure 52. Photograph of the SPS-processed samples before and after HIP. ....	121
Figure 53. HIP post SPS did not improve the transmittance of SPS processed spinel. Data was normalized to the transmittance at the thickness of 1.8 mm.....	121
Figure 54. Photograph showing the inhomogeneity in the transparency of SPS-processed spinel after HIP. ....	122
Figure 55. FTIR spectra of the alumina coated powder.....	124
Figure 56. Illustration of the possibilities of how the newly formed Al <sub>2</sub> O <sub>3</sub> took part in the spinel powder. ....	126
Figure 57. TEM images of (a) the undoped powder, S30CR, and (b) the 10 wt% Al <sub>2</sub> O <sub>3</sub> doped powder, S10A.....	129
Figure 58. X-ray diffraction of an 10 wt.% alumina-doped spinel powder, S10A, compare to the as-received powder, S30CR. (a) No new phase was formed; (b) Peak shift at the low angles was less than peak shift at the high angles .....	130
Figure 59. Illustration of the transparency of alumina doped samples. From the left: S0A, S1A, S3A, and S5A. The samples on the first row were SPS without the alumina protective layer. The samples on the second row were SPS with the alumina protective layer.....	132
Figure 60. The in-line transmittance of the doped samples. (a) SPS without the alumina layer inserted between spinel powder and the graphite die; (b) SPS with the alumina layer inserted between spinel powder and the graphite die .....	133
Figure 61. XRD patterns of the doped samples compare to the undoped sample. ....	134
Figure 62. FESEM images of the doped samples. ....	136
Figure 63. TEM-EDX mapping of S10A.....	137
Figure 64. Line-scan STEM analysis of S10A. ....	138
Figure 65. Effects of Al <sub>2</sub> O <sub>3</sub> doping on the hardness of the samples. (a) Vickers hardness and (b) Knoop hardness. ....	141
Figure 66. Raman spectra of the samples SPS at 1300°C, taken with a 514 nm laser excitation line.....	144
Figure 67. Raman spectra of the samples SPS at 1350°C, taken with a 514 nm laser excitation line.....	145

## 1. Introduction and literature reviews

### 1.1. Motivation

Polycrystalline magnesium aluminate spinel ( $\text{MgAl}_2\text{O}_4$ ) is transparent in the visible and near infrared regions, and offers a unique combination of optical, mechanical and thermal properties. It has long been recognized as a potential candidate for light weight transparent armor and infrared window applications. One advantage of spinel over the conventional bullet-proof glass is that the mechanical strength of spinel is about three times higher than that of glass.<sup>1,2</sup> Another advantage is that spinel is more thermally stable at high temperatures: While glass melts at temperatures below  $1600^\circ\text{C}$ , spinel can remain in its solid state until  $2000^\circ\text{C}$ .<sup>3,4</sup> Although the mechanical strength of spinel is lower than that of other candidates such as AlON and sapphire, its much lower manufacturing cost due to a lower processing temperature makes it affordable and commercializable.<sup>2</sup> In addition, in the mid-wave infrared region from  $3\mu\text{m}$  to  $6\mu\text{m}$ , spinel exhibits a lower radiation absorption and a higher transmittance at elevated temperatures up to  $1000^\circ\text{C}$ .<sup>1</sup>

Interestingly, the structure of spinel is very flexible regarding to the cation sites. A wide range of divalent cations can take the place of the  $\text{Mg}^{2+}$  atoms to derive in a series of aluminate spinel.<sup>5,6</sup> Similarly, the  $\text{Al}^{3+}$  cations can be substituted by almost any trivalent cation and some tetravalent cations. The cation exchange also happens between  $\text{Mg}^{2+}$  and  $\text{Al}^{3+}$  resulting in a disorder on the cation sub-lattice and accommodating non-stoichiometry at high temperatures. As can be seen in the binary phase diagram of the  $\text{MgO} - \text{Al}_2\text{O}_3$  system,<sup>4</sup> although  $\text{MgAl}_2\text{O}_4$  with an exact equimolar fraction of  $\text{MgO}$  and  $\text{Al}_2\text{O}_3$  is the only intermediate compound, a wide range of the spinel phase from 0.5 to 0.9 in mole fraction of  $\text{Al}_2\text{O}_3$  is also exhibited at elevated temperatures. Noticeably, it was seen on both single

crystalline spinel and polycrystalline spinel that non-stoichiometric spinels are harder and stronger than the stoichiometric ones.<sup>7, 8</sup>

Although investigations on the production of transparent polycrystalline spinel was initiated in the late 1960's,<sup>9, 10</sup> the maturity of transparent spinel manufacture is still in the advancement progress, and the availability of commercial spinel armors is still limited. Many efforts regarding powder synthesis, methods of sintering, and polishing have been carried out to fabricate a polycrystalline spinel product with an excellent optical and mechanical performance. However, a complete solution has not been well satisfied because there has always been a trade-off between the transparency and the strength of spinel. This trade-off is primarily associated with the densification technique selected. Hot-pressing (HP) and hot-isostatic-pressing (HIP) post sintering have been used to produce a fully dense spinel with excellent transparency: up to 85% in the visible region, and up to 90% in the near infrared region.<sup>7, 11-14</sup> However, due to the low heating and cooling rates ( $< 10$  °C/min) and the high sintering temperatures (1500 – 1650°C) of these techniques, the grain size of the sintered products is large, normally in the range of 5 – 100µm depending on the heating profile.<sup>14, 15</sup> It has been documented that the hardness of polycrystalline ceramics depends on the average grain size in a tendency that a decrease in the average grain size results in a noticeable increase in the hardness.<sup>16-18</sup> Therefore, an alternative sintering technique that can help to minimize grain growth during sintering has been sought. The spark plasma sintering (SPS) technique, so-called field-assisted sintering technique (FAST), features a much faster heating and cooling rate (up to 600°C/min or more), and requires a lower sintering temperature (1300 – 1350°C) for spinel, therefore it helps to minimize grain coarsening. However, the SPS condition for producing transparent spinel

has not been optimized, and transmittance of the SPS spinel samples in the visible region remains low, mostly less than 70%, due to light absorption and discoloration.<sup>19-28</sup>

Another effort to lower the sintering temperature and shorten the processing time is to use sintering additives. Chemicals that have low melting temperatures, such as LiF, CaF<sub>2</sub>, BaF<sub>2</sub>, ZnF<sub>2</sub>,<sup>15, 29-31</sup> have been used to promote the densification of spinel via a liquid-phase sintering mechanism. Other additives, including CaO,<sup>32</sup> TiO<sub>2</sub>, B<sub>2</sub>O<sub>3</sub>,<sup>31, 33</sup> Dy<sub>2</sub>O<sub>3</sub>,<sup>34</sup> Y<sub>2</sub>O<sub>3</sub>,<sup>35-37</sup> MgO, La<sub>2</sub>O<sub>3</sub>,<sup>35,36</sup> ZnO and MnO<sub>2</sub>,<sup>38</sup> that favor either liquid-phase sintering or solid-state sintering were also studied. Although the densification was enhanced, it was not clear whether an optical-grade spinel can be obtained in all cases. In many cases, the existence of a glassy phase at the trigranular junctions and excessive grain growth was potentially detrimental to the strength of spinel.

This work seeks to develop a better understanding of the densification of transparent polycrystalline spinel during spark plasma sintering. The SPS processing parameters were manipulated to produce dense samples from a high-purity spinel powder. The correlation between the microstructure and optical properties of the dense samples was analyzed to determine the processing factors that are critical to the densification of spinel in the SPS. From this understanding, the SPS conditions was optimized for spinel so that the material can reach its highest transmittance without an excessive grain growth in the shortest processing time.

This work also seeks to improve the hardness of transparent polycrystalline spinel by using alumina to engineer the grain boundary. The ability of spinel to intake alumina with an increase in the strength but without a change in the crystal structure was utilized. Alumina was coated onto spinel particles via a precipitation method to ensure a

homogeneous distribution of alumina among spinel particles. The ability of the SPS to facilitate a very high heating/cooling rate was employed to produce a transparent spinel without excessive grain growth which is detrimental to the strength and the hardness of the material. The microstructural, optical and mechanical properties of the doped samples after SPS was analyzed to determine the amount of alumina that helps to improve the hardness without a significant degradation of the transmittance of the samples.

## **1.2. Magnesium aluminate spinel**

### **1.2.1. History**

Pure single crystalline magnesium aluminate spinel is colorless and transparent but impurities give rise to a range of colors including red, purple, pink, violet, indigo, blue, green and black, and make the history of spinel full of misidentification. Natural spinel crystals are actually gemstones, not only because of their various brilliant colors but also because of their high hardness. Spinel has a hardness of up to 8 on the Mohs scale.<sup>39</sup> However, red spinels were mistaken for rubies, and blue spinels were mistaken for sapphires for a long time because of a similarity of color, and because they were sometimes found together in the same quarry. Two thousand years ago, Plinius described *carbunculus* (from Latin meaning small piece of carbon) as the first-order red gemstone. Accordingly, the term *carbunculi* was a collective designation of red gems. It was not until the thirteenth century that Albertus divided *carbunculus* into *balagius*, *granatus* and *rubinus* which presumably correspond to today's spinel, garnet and ruby, respectively.<sup>40, 41</sup> Two of the most famous examples of misidentification are the "Black Prince's ruby" in the Imperial

State Crown and the “Timur ruby” of the Royal collection of the Queen of England. These two legendary “rubies” are actually red spinel.<sup>42</sup>

Spinel was recognized by the Burmese as a distinct species of gem in the sixteenth century.<sup>43</sup> However, it was not until 1908 that spinel was distinguished from ruby by chemical composition when synthetic spinel crystals were advertently produced in an attempt to produce blue sapphire crystals.<sup>44</sup> The name spinel probably derives from the Latin *spinella* meaning “little thorn” in allusion to the spine-shaped octahedral crystals.<sup>39</sup>

A group of minerals that share the chemical formula  $AB_2X_4$  and crystallize in the face centered cubic system was named after spinel.<sup>5, 6</sup> Popularly, A is a divalent cation, B is a trivalent cation, and X is oxygen. However, the chemical composition of the minerals in this group is very flexible. In many cases, A and B can be a suitable combination of divalent, trivalent and/or tetravalent cations, and X can be sulfur, selenium, tellurium or cyanide<sup>45</sup>. Some examples of the minerals in the spinel group include spinel  $MgAl_2O_4$ , magnetite  $FeFe_2O_4$ ,<sup>46, 47</sup> ringwoodite  $(Mg, Fe)_2SiO_4$ ,<sup>48</sup> and cuprokalinitite  $CuCr_2S_4$ .<sup>49</sup>

Magnesium aluminate spinel is a refractory material because it has a melting temperature as high as 2122°C.<sup>4</sup> Little was known about the production of spinel refractories until the 1920's. Since natural spinels were rare, and the flux-grown synthetic spinel was expensive,<sup>44</sup> different synthesis techniques have been developed to produce spinel for the heat-resistant application. In 1923, a patent was granted to Tone<sup>50</sup> for his invention of producing a rock-like spinel by fusing a mixture containing alumina and magnesia in an electric furnace. After that, Rieke and Blicke<sup>51</sup> demonstrated that synthetic spinel could be produced by heating a mixture of alumina and magnesia at elevated temperatures. In its early years, spinel and spinel containing refractories was used in the

electric steel furnace,<sup>52, 53</sup> sulfate recovery furnace,<sup>54</sup> oil-gas generator,<sup>55</sup> and glass melting crucibles.<sup>56</sup> However, because of a high production cost, little use was made of spinel refractories until the 1970's, when the cement industry started to use magnesia spinel refractory for clinker rotary kilns. Beside electrofused spinel, synthetic spinels were produced in several other forms, including sintered spinel clinker, sintered magnesia-spinel co-clinker and calcined spinel. They were used mostly in the steel and cement industries in forms of monolithic and/or fired bricks.<sup>57</sup> Spinel and spinel containing refractories have become more popular since the 1990's when concerns about the toxicity of the chromite-based refractory, a lower-cost substitution, became intensified.<sup>58-60</sup>

Once being pure and fully dense, polycrystalline spinel is an excellent candidate for transparent armors because of its unique combination of the mechanical and optical properties. The elastic modulus of polycrystalline spinel is 287 GPa,<sup>7</sup> and the Knoop micro-hardness with a one kilogram load is up to 13 GPa.<sup>17</sup> An in-line transmittance of about 85% was observed on the transmission window from 0.2  $\mu\text{m}$  to 6.5  $\mu\text{m}$ .<sup>61</sup>

The physical properties of spinel were known from synthetic crystals available from Linde Air Products since around 1950.<sup>62</sup> Investigations on the production of transparent polycrystalline spinel were initiated in the late 1960's when a hard, strong, transparent material was needed for windows acting as a protection against armor piercing projectiles.<sup>9,</sup><sup>10</sup> However, the lack of a suitable raw material was the major deterrence to success in many laboratories until the 1980's when a high purity spinel powder derived from sulfate solutions became available from the Baikowski Corporation.<sup>61</sup> Since then, numerous government funded research projects and development contracts on producing transparent spinel have been carried out at different US research institutions and companies, including

Coors Ceramics, Raytheon Research Division, Alpha Optical Systems, RCS Technologies, TA&T and Surmet. The leading figure in the development of transparent polycrystalline spinel was Don Roy who started doing research on transparent spinel at Coors Ceramics in the late 1960s and succeeded in producing transparent spinel dome by hot pressing in the early 1980s.<sup>62</sup>

Since the late 2000's, another burst of activity has been developed, focusing on improving the mechanical strength of transparent polycrystalline spinel by minimizing final grain size. Investigations toward this goal followed two main directions, one was examining the use of nano-size spinel powder, while the other focused on shortening the sintering cycle using the spark plasma sintering technique.<sup>19-25, 36, 63, 64</sup>

### 1.2.2. MgO – Al<sub>2</sub>O<sub>3</sub> binary phase diagram

Figure 1 (a) is the binary phase diagram of the MgO – Al<sub>2</sub>O<sub>3</sub> system.<sup>4</sup> Both of the end components are refractory substances: MgO melts at 2825°C while Al<sub>2</sub>O<sub>3</sub> melts at 2054°C. The mineral of MgO, periclase, crystallizes in the cubic system, space group Fm3m, with a density of 3.58 g/cm<sup>3</sup>. The commonly occurs mineral of Al<sub>2</sub>O<sub>3</sub> is corundum,  $\alpha$ -Al<sub>2</sub>O<sub>3</sub>. It crystallizes in the hexagonal system, space group R3c, with a density of 3.997 g/cm<sup>3</sup>.<sup>39</sup>

The two components form spinel (MgAl<sub>2</sub>O<sub>4</sub>) at their equimolecular proportion, and this is the only intermediate compound formed in the system. Spinel is also a refractory substance with a melting point at 2122°C. It crystallized in the cubic system, space group Fd3m, with a density of 3.578 g/cm<sup>3</sup>.<sup>39</sup> The reaction between magnesia (MgO) and alumina (Al<sub>2</sub>O<sub>3</sub>) was found to proceed slowly with a substantial reaction-expansion.<sup>65</sup>

The formation of spinel divides this binary phase diagram into two independent eutectic systems. Those are  $\text{MgO} - \text{MgAl}_2\text{O}_4$  and  $\text{MgAl}_2\text{O}_4 - \text{Al}_2\text{O}_3$ . The eutectic point of the  $\text{MgO}$ -rich part is at  $1985^\circ\text{C}$  and  $0.36 \text{ Al}_2\text{O}_3$  in mole fraction, while the eutectic point of the  $\text{Al}_2\text{O}_3$ -rich part is at  $1994^\circ\text{C}$  and  $0.79 \text{ Al}_2\text{O}_3$ .<sup>4</sup>

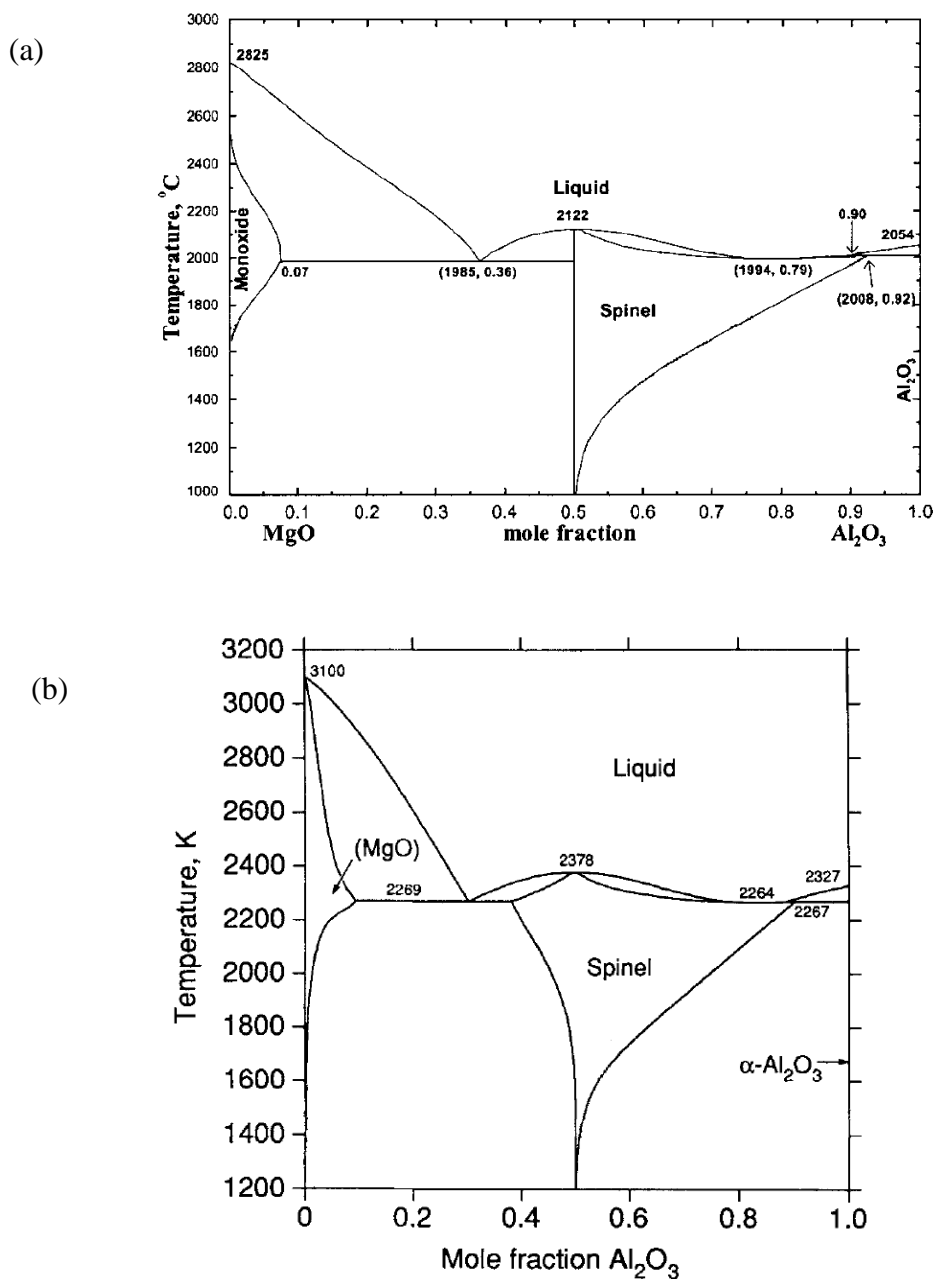


Figure 1. Binary phase diagrams of the  $\text{MgO}-\text{Al}_2\text{O}_3$  system. (a)  $\text{MgO}$ -rich spinel solid solution is not formed at elevated temperature.<sup>4</sup> (b)  $\text{MgO}$ -rich spinel solid solution is formed at elevated temperature.<sup>66</sup>

Off-stoichiometric spinel phase forms only in the alumina rich region starting at about 1000°C. The dissolution of Al<sub>2</sub>O<sub>3</sub> into the spinel solid solution increases as the temperature increases, and it reaches the highest point at 2008°C with 0.92 mole of Al<sub>2</sub>O<sub>3</sub> in one mole of the spinel solid solution. The solid solution at this point could be expressed as MgAl<sub>23</sub>O<sub>35.5</sub> or MgO.11.5Al<sub>2</sub>O<sub>3</sub>.

Another MgO-Al<sub>2</sub>O<sub>3</sub> phase diagram of interest is the one showing the MgO- rich solid solution at elevated temperatures (Figure 1(b)). The degrees at which MgO participates in the solid solution is lower than that of Al<sub>2</sub>O<sub>3</sub> at the same temperature. Disagreement on the formation of MgO-rich solid solution was due to the fact that there was no measurable change in the lattice parameter when MgO dissolved into spinel.<sup>66</sup>

### 1.2.3. Crystal structure

The crystal structure of the mineral spinel is quite complicated due to the participation of a large number of atoms. A spinel unit cell is made up of 8 molecules of MgAl<sub>2</sub>O<sub>4</sub>.<sup>46,47</sup> Each of the Mg sites is surrounded by four oxygen atoms, forming an MgO<sub>4</sub> tetrahedron. Meanwhile, each of the Al sites is surrounded by six oxygen atoms, forming an AlO<sub>6</sub> octahedron.

Figure 2 illustrates the arrangement of the Mg, Al and O atoms in a unit cell. Each of the MgO<sub>4</sub> tetrahedra shares the oxygen atoms at its vertices with four adjacent AlO<sub>6</sub> octahedra. Meanwhile, each of the AlO<sub>6</sub> octahedra shares its edges with other AlO<sub>6</sub> octahedra to satisfy the population of the oxygen atoms in the unit cell. Referring to the space group *Fd3m*, Mg, Al and O atoms in the spinel structure occupy the equivalent positions 8a (0, 0, 0), 16d ( $\frac{5}{8}, \frac{5}{8}, \frac{5}{8}$ ) and 32e ( $\frac{3}{8}, \frac{3}{8}, \frac{3}{8}$ ), respectively.<sup>6,67</sup> Because of a large

number of the  $\text{MgAl}_2\text{O}_4$  molecules in a unit cell, the lattice parameter,  $a$ , of spinel is large.

As measured by Finger et.al.,<sup>68</sup> the lattice parameter of a natural spinel was  $0.80898 \text{ \AA}$ .

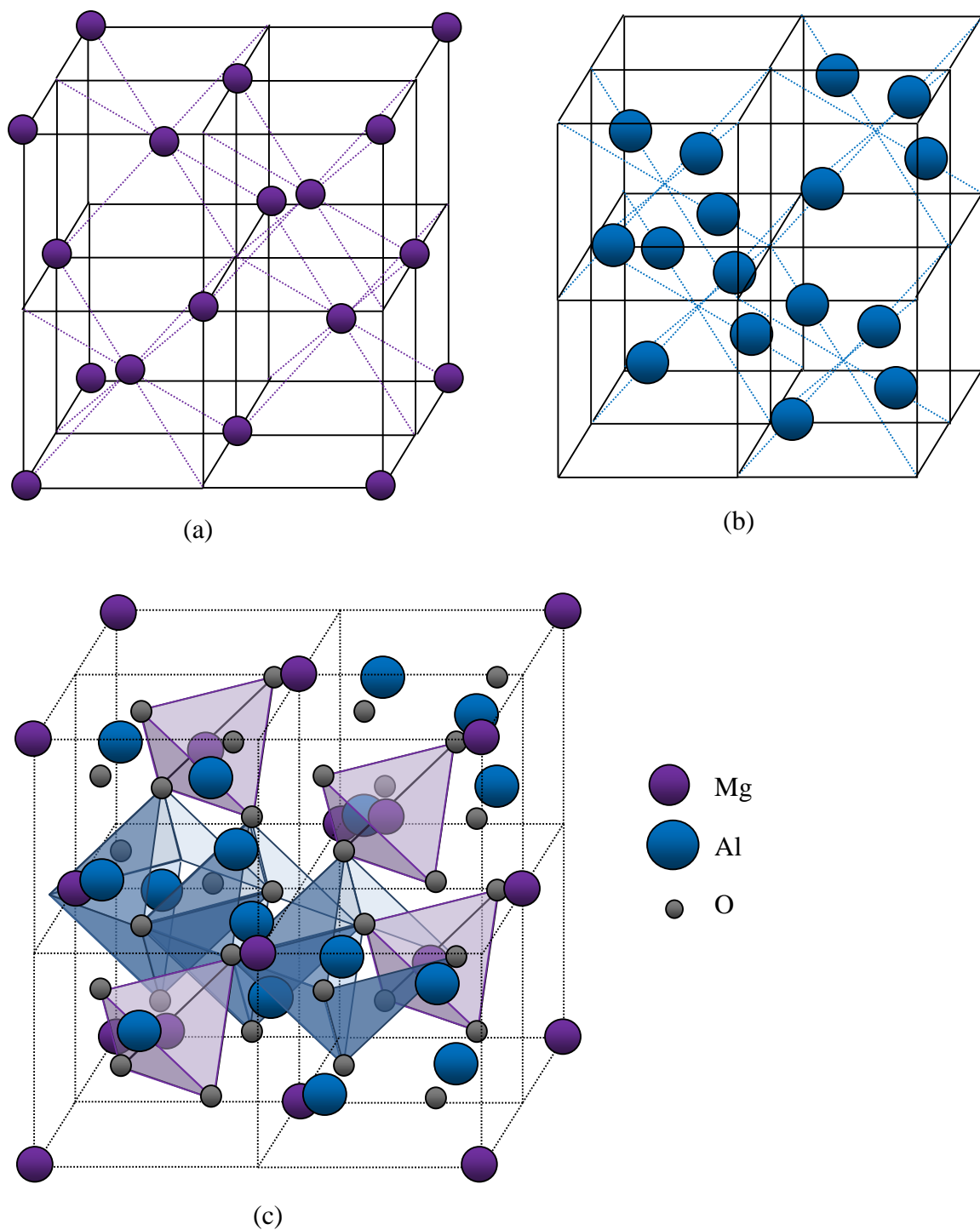


Figure 2. Illustration of the arrangement of the Mg, Al, and O atoms in a spinel unit cell. (a) Arrangement of the Mg atoms; (b) Arrangement of the Al atoms; (c) The  $\text{MgO}_4$  tetrahedra and the  $\text{AlO}_6$  octahedra in a unit cell. (adapted from Nishikawa<sup>47</sup>)

Similar to other minerals in the spinel group, the structure of spinel is very flexible regarding to the cation sites. A wide range of cations can take the place of  $Mg^{2+}$  and  $Al^{3+}$ . The cation exchange also happens between  $Mg^{2+}$  and  $Al^{3+}$  resulted in a disorder in the cation sub-lattice. Barth and Posnjak<sup>69</sup> suggested that the spinel structure may possess variate atom equipoints with a portion of the  $Mg^{2+}$  cations residing on the octahedral sites, and an equal number of the  $Al^{3+}$  cations residing on the tetrahedral sites. The resulted antisite defects can be presented using the Kroger-Vink notation:<sup>70</sup>



where  $Mg_{Mg}^{\times}$  is a magnesium ion sitting on the magnesium site with neutral charge,  $Al_{Al}^{\times}$  an aluminum ion sitting on the aluminum site with neutral charge,  $Mg'_{Al}$  is a magnesium ion sitting on the aluminum site with singular negative charge, and  $Al^0_{Mg}$  is an aluminum atom sitting on the magnesium site with singular positive charge.

The cation exchange between  $Mg^{2+}$  and  $Al^{3+}$  becomes the central role in accommodating non-stoichiometry at high temperatures. As proposed by Murphy *et.al.*,<sup>71</sup> the incorporation energy per cation for  $Al_2O_3$  excess was lower than that for  $MgO$  excess, therefore  $Al_2O_3$  – rich spinel was favored beyond the equimolar point of  $MgAl_2O_4$ . The neutrality in an  $Al_2O_3$  – rich spinel is achieved by the compensation of oppositely charged point defects but not between opposite cation antisite defects. As the result, this compensation creates three types of defect clusters,  $\{O_i'' : 2Al_{Mg}^0\}^{\times}$ ,  $\{V_{Mg}'' : 2Al_{Mg}^0\}^{\times}$  and  $\{V_{Al}''' : 3Al_{Mg}^0\}^{\times}$ , where  $O_i$  is the interstitial site occupied by an oxygen atom,  $Al_{Mg}$  is the Mg site occupied by an Al atom,  $V_{Mg}$  is the Mg site being vacant, and  $V_{Al}$

is the Al site being vacant. The sign  $\times$  indicates that the cluster has a neutral charge, the sign  $'$  stands for a negative charge, and the sign  $^{\circ}$  stands for a positive charge. The dissolution of these defect clusters is facilitated at elevated temperatures, therefore alumina-rich spinel is observed on a large area of the MgO-Al<sub>2</sub>O<sub>3</sub> phase diagram. The current study employed the ability of spinel to intake more Al<sup>3+</sup> cations to add Al<sup>3+</sup> cations into the sub-grain boundary of a polycrystalline spinel and examine the changes in hardness and transmittance of the material.

#### 1.2.4. Electronic structure

A number of experimental and computational approaches have been made to investigate the electronic structure of spinel, but a consistent result has not been achieved. By comparing the optical data of MgAl<sub>2</sub>O<sub>4</sub> and MgO, Bortz *et.al.*<sup>72</sup> predicted that the electronic structures of these oxide were very similar, and their measurement on a synthetic basal plane spinel gave a ( $\Gamma$ - $\Gamma$ ) direct band gap value of 7.8 eV. The calculations of Khetana *et.al.*<sup>73</sup> and Sampath *et.al.*<sup>74</sup> showed a ( $\Gamma$ - $\Gamma$ ) direct band gap but the calculations of Xu and Ching<sup>75</sup> and Hosseini<sup>76</sup> gave also indirect band gaps, ( $\Gamma$ -X) and ( $\Gamma$ -L). Besides, those works did not get agreements in the band gaps and bandwidth values. The difficulty in getting a consistent electronic structure can be addressed to the complicated crystal structure and charge distribution of spinel. It can also be addressed to the computational method selected.

## 1.2.5. Optical properties

### 1.2.5.1. Definitions

Transmittance,  $T$ , is the transmitted spectral radiant power,  $P_\lambda$ , through a particular path length,  $l$ , divided by the spectral radiant power incident on the sample,  $P_\lambda^o$ .<sup>77</sup>

$$T_l = \frac{P_\lambda}{P_\lambda^o} \quad \text{Eq. 2}$$

The spectral radiant power,  $P_\lambda$ , is the derivative of radiant power,  $P$ , with respect to wavelength,  $\lambda$ .

### 1.2.5.2. Optical properties of single crystalline spinel

Spinel is transparent in the visible and infrared regions. It has a transmission window of 0.2–6  $\mu\text{m}$  in wavelength.<sup>1</sup> The transmittance of a 0.08-inch-thick single crystal spinel measured by Blodgett *et.al.* was 82% at 632.8 nm and 88% at 3.39  $\mu\text{m}$ .<sup>78</sup> The dispersion equation for the refractive index ( $n$ ) of a bulk crystalline (or polycrystalline) stoichiometric spinel in the visible and IR transparent region is:

$$n^2 - 1 = \frac{18.96 \times 10^9}{100080^2 - \nu^2} + \frac{1.2234 \times 10^6}{527.18^2 - \nu^2} \quad \text{Eq. 3}$$

where  $\nu$  is the frequency in wave numbers.<sup>79</sup>

Owing to its high symmetrical crystalline structure, spinel is optically isotropic. Light waves are transmitted with equal velocity in all directions as they pass through a

spinel crystal, and gives only one image regardless of the viewing angle.<sup>80</sup> This feature makes polycrystalline spinel transparent and is preferred for optical windows.

#### *1.2.5.3. Optical properties of polycrystalline spinel*

Polycrystalline spinel is a compact mass composed of randomly oriented individual microscopic spinel crystals. Theoretically, the optical properties of a cubic crystal are equal in every direction, the light is not scattered (refracted and reflected) at the grain boundary as it passes through one grain to another inside a polycrystalline spinel.<sup>1</sup> As a result, polycrystalline spinel inherits the optical properties of the single crystalline spinel in both the visible and the infrared regions. In practice, light transmittance of polycrystalline ceramics is affected by various scattering factors such as the presence and amount of the second phase and impurities, grain boundaries, porosity, and the surface condition.

Impurities tend to aggregate at the crystalline grain boundaries because they are precluded from the grain structure during crystallization and form a region with a chemical composition that is different from the bulk nearby. This region normally has a different morphology and a different refractive index. When the light passes from one grain to another, it is reflected and refracted at the grain boundary causing a scattering effect that lowers the transmittance of light through the material.<sup>1</sup>

The most important light scattering origins in polycrystalline ceramics are rough surface, pores and grain boundaries.<sup>81, 82</sup> In case of spinel, Krell *et.al.*<sup>83</sup> demonstrated that a small amount (< 0.01%) of nano-scale pores could diminish the in-line transmittance of spinel in a wide range, from the UV region to the IR region. The existence of the micro-

cracks along the grain boundaries is another factor that diminishes the light transmittance of the sintered spinel. The dependence of transmittance on the amount of micro-cracking in a polycrystalline spinel could be expressed as a linear relationship between the natural logarithm of light transmittance and micro-cracked grain boundary surface area per unit volume: <sup>84</sup>

$$T \cong (1 - R)^2 \exp(-\beta' S_v^{Mc} t) \quad \text{Eq. 4}$$

where T is the transmittance, R is the reflectance,  $\beta'$  is a constants,  $S_v^{Mc}$  is the micro-cracked grain boundary surface area per unit volume, and t is the thickness of the sample.

$$R \cong \frac{(\bar{n} - n_a)^2}{(\bar{n} + n_a)^2} \quad \text{Eq. 5}$$

where  $\bar{n}$  is the mean reflective index of a single crystalline spinel, and  $n_a$  is the reflective index of air ( $n_a \cong 1$ ).

A fully dense polycrystalline spinel fabricated from a high-purity starting powder would have a transmittance that is almost close to the transmittance of the natural single crystalline spinel. However, the present of the micro-cracks can diminish the transmittance of the material due to the scattering phenomenon discussed above. Table 1 presents the transmittance of polycrystalline spinel fabricated by different sintering techniques.

Table 1. Examples of the transmittance of spinel from different sources.

Types of spinel (fabrication method)	Thickness, mm	Grain size, nm	Transmittance, % (wavelength)	
			Visible	Infrared
Single crystalline (natural spinel) <sup>78</sup>	2.032		82 (632.8 nm)	88 (3.39 $\mu\text{m}$ )
Polycrystalline (HIP post HP) <sup>11</sup>	2.54		80 (300 nm)	86 (3.0 $\mu\text{m}$ )
Polycrystalline (HP) <sup>85</sup>	2.2	10,000 – 20,000		> 85 (1.4 $\mu\text{m}$ )
Polycrystalline (SPS) <sup>28</sup>	2.3	250 – 450		> 80 (1.5 $\mu\text{m}$ )

### 1.2.6. Mechanical properties

Harris<sup>1</sup> showed that the strength of a material depends on the type and quality of surface finishing, material fabrication method, material purity, test method and specimen size. Spinel is not an exception.

Table 2 collects the mechanical properties of spinel from different sources. For  $\text{MgO} \cdot n\text{Al}_2\text{O}_3$  spinel single crystal, there is a trend that the material gets stronger as  $n$  increases from 1 to 3.5 because its elastic modulus, Young's modulus, bulk modulus and shear modulus are all slightly increased.<sup>8</sup> This trend was also observed in polycrystalline spinel.<sup>7, 37</sup>

The effects of the stoichiometry on the mechanical properties of spinel suggest that if  $\text{Al}_2\text{O}_3$  is added into a stoichiometric spinel, the mechanical properties of the material might be improved. However, if  $\text{Al}_2\text{O}_3$  is not distributed homogeneously and stays as a second phase, it will cause light scattering and diminish the transmittance of the material. This work, therefore, added different amounts of  $\text{Al}_2\text{O}_3$  into spinel to investigate their

effects on the properties of the final products. In order to avoid inhomogeneity, a thin layer of the alumina additives was coated on the spinel particles by the precipitation method.

Table 2. Mechanical properties of spinel.

Properties	Single crystal	Polycrystalline spinel		
	Ref. <sup>8 (b)</sup>	Ref. <sup>37 (c)</sup>	Ref. <sup>86</sup>	Ref. <sup>7 (d)</sup>
Elastic modulus , GPa	118; 123; 124		273	287.3; 292.9
Young's modulus , GPa	295; 303; 308			
Bulk modulus , GPa	197; 204; 206		192	
Shear modulus, GPa	118; 121; 123		110	
Poisson ratio	0.25		0.26	
Fracture toughness, GPa		1.4		
Compressive strength, MPa		364; 470	2690	
Biaxial flexure strength, MPa			172	157.3; 176.8
Hardness <sup>(a)</sup> , GPa				
HK <sub>0.1</sub>	-	-	13.7	-
HK <sub>0.5</sub>	-	-	-	-
HK <sub>1</sub>	-	-	-	-
HK <sub>2</sub>	-	-	-	12.2; 12.3
HV <sub>0.5</sub>	-	-	-	-
HV <sub>1</sub>	-	-	-	-
HV <sub>2.5</sub>	-	15.2; 16.8	-	-

<sup>(a)</sup> Test load in kilogram

<sup>(b)</sup> As  $n$  increases from 1 to 2.6 and 3.5

<sup>(c)</sup> As the average grain size decreases from 2.1  $\mu\text{m}$  to 345nm

<sup>(d)</sup> As  $n$  increases from 1 to 1.2 and the average grain size increases from 488 nm to 1018 nm

For polycrystalline spinel, besides the chemical composition, the microstructure of the material greatly affects the mechanical behavior of the material. This complication will be discussed further via the hardness of spinel in the following sub-sections.

### 1.2.6.1. Hardness of single crystalline spinel

Among the mechanical properties of a ceramic, hardness is extremely important because it is the measure of the material's resistance to permanent deformation or damage.<sup>87</sup> *"It correlates with many other properties as reflected in compressive strength, ballistic performance of armor, machining behavior, and friction and wear phenomena"*.<sup>88</sup> Therefore, the hardness of spinel is discussed in this section.

Although spinel is optically isotropic, its hardness is anisotropic. Akimune and Bradt<sup>89</sup> demonstrated that the Knoop micro-hardness with a 0.1 kg load on the (100) plane varied in a range from 14.7 GPa to 17.7 GPa depending of the indenter orientation. The maximum occurred when the indenter was parallel to the plane (001) and the minimum occurred when the indenter was parallel to the plane (011). However, the Knoop micro-hardness on the (111) plane was constant,  $KV_{0.1} = 14.8$  GPa, and independent of the indenter orientation. The dependence of hardness on the indented plane and the indenter orientation was also observed on several other f.c.c crystals, including aluminum<sup>90</sup>, MnSe<sup>91</sup> and diamond<sup>92</sup>.

The nature of anisotropy in hardness was due to the crystal structure and the primary slip systems that accommodate dislocation during indentation. For stoichiometric spinel, Hornstra<sup>93</sup> predicted that the dislocation glide would occur parallel to the {111} plane with two almost-coincide Burgers vectors  $\frac{1}{4}a_0\sqrt{2}$  in the  $\langle 110 \rangle$  direction, forming the {111}  $\langle 110 \rangle$  primary slip system. This prediction was later confirmed by Hwang et.al.<sup>94</sup> and others<sup>89</sup>. Although the {111} $\langle 110 \rangle$  slip system was predominant in the stoichiometric spinel, the {110} $\langle 110 \rangle$  slip system was observed in all type of Al-rich non-stoichiometric

spinel<sup>8, 95-97</sup>. Brookes *et.al.*<sup>98</sup> developed an expression that related the hardness with the effective resolved shear stress,  $\tau'_e$ , in bulk of the crystal beneath the indenter:

$$\tau'_e = \frac{1}{2}(F/A)\cos\lambda \cos\phi(\cos\psi + \sin\gamma) \quad \text{Eq. 6}$$

where F is the applied force, A is the cross-sectional area of the specimen,  $\lambda$  is the angle between the stress axis and slip direction,  $\phi$  is the angle between the stress axis and the normal to the slip plane,  $\psi$  is the angle between the face of an adjacent facet and the axis of rotation for a given slip system, and  $\gamma$  is the angle between the slip direction and the axis of rotation for a given slip system. The minimum values of  $\tau'_e$  on specific planes correspond to the maximum hardness and vice versa. Although this expression did not give an absolute value of hardness, it indicated that the anisotropy in hardness was controlled by the performance of dislocation on the primary slip system.

#### *1.2.6.2. Hardness of polycrystalline spinel*

Unlike single crystalline spinel, polycrystalline spinel does not possess a primary slip system. Like other polycrystalline ceramics, a polycrystalline spinel is composed of randomly oriented microscopic crystalline grains, and the size of these grains is normally much smaller than the size of the indents. When an indenter is pressed against a polycrystalline spinel, the resulted stresses act parallel to the slip plane of some grains and to the non-slip planes of the others. They also act on the grain boundaries, where impurities segregate during the crystallization of the material and cause a hardening and

embrittlement.<sup>99</sup> Therefore, the hardness of a polycrystalline spinel depends very much on the microstructure of the material rather than on the indenter orientation.

Due to the existence of multiple grains under the indenter, the hardness (H) of a polycrystalline spinel depends on the average grain size (G) of the material. The H – G relation has two trends: H decreased with increasing G for finer G due to the Hall – Petch effect (e.g.  $H \propto G^{-1/2}$ ),<sup>16, 100</sup> but decreased with decreasing G for larger G. The intermediate grain size where H reaches its minimum varies depending on the load and the type of the indenter being used. For Knoop indentation, Rice *et.al.*<sup>18</sup> obtained the H minimum at  $G \sim 100\mu\text{m}$  and between  $5 - 20 \mu\text{m}$  for the 500 g – and the 100 g – loads, respectively. For Vickers hardness indentation, the H minimum was measured at larger grain sizes for both loads. They suggested that when the grain and the indent were similar in size, the local crack around the indent tended to reach a maximum effect, hence H reached its minimum. Therefore, control of grain size is crucial for obtaining a high hardness sample.

The hardness of polycrystalline spinel also depends on the indentation size in a trend that a lower load gives a higher hardness value. The hardness-load curve of a spinel with bimodal grain-size distribution obtained by Patel *et.al.*<sup>101</sup> showed higher hardness values at the lower loads (100g, 200g, and 300g), and that the hardness decreased slightly as the load decreased from 500g to 1000g and 2000g.

### **1.2.7. Electrical properties**

Spinel is electrically non-conductive at room temperature but its conductivity increases slightly at elevated temperatures.<sup>102-107</sup> It appeared that the conductivity behavior of spinel was quite complicated, and that it was more complicated in polycrystalline spinel

than in single crystalline spinel. The conductivity of a single crystalline stoichiometric spinel could be resolved into three linear sections on a plot of the logarithm of the conductivity versus the reciprocal of the temperature (Figure 3).<sup>102</sup> The transition between them was at about 950 K and 1400 K. However, the conductivities of single crystalline non-stoichiometric spinels have a simpler temperature dependence than found in the stoichiometric one. The conductivity of the non-stoichiometric spinel could be fitted very well (on plots of the logarithm of the conductivity versus the reciprocal of the temperature), with two linear segments. The change in slopes appeared at 800°C.<sup>103</sup>

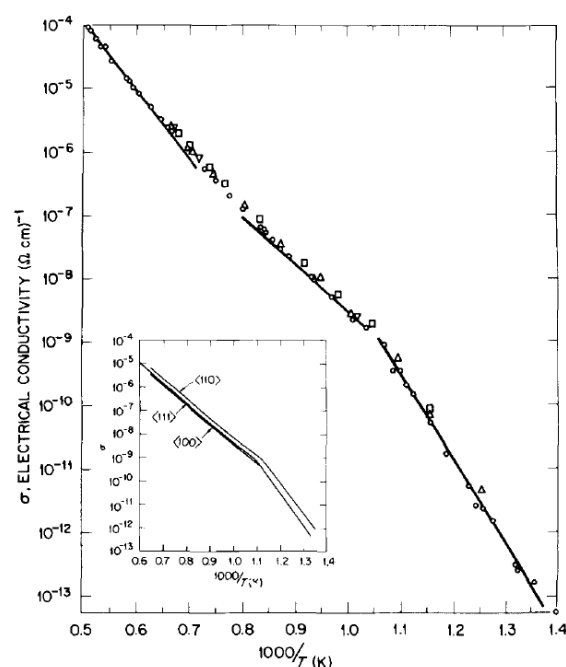


Figure 3. Temperature dependence of the electrical conductivity of a nominally pure  $\text{MgAl}_2\text{O}_4$  single crystal.<sup>102</sup>

In an independent study, Bates and Garnier<sup>105</sup> found that the electrical conductivity of a single crystalline spinel was lower than that of a sintered polycrystalline spinel. They also found that the conductivity of the polycrystalline spinel was dependent of the

atmosphere and time of the applied voltage, but the conductivity of the single crystalline spinel was independent of those factors.

The conductivity of spinel depends not only on the temperature but also on the heat treatment time. Sonder and Weeks<sup>107</sup> demonstrated that the conductivity of spinel increased with the heat treatment time. This behavior was similar to that observed for MgO and could lead to thermal runaway.

The complication of the conductivity behavior of spinel was difficult to interpret with simple models. A possible explanation was that magnesium ions became mobile when spinel was heated in an electric field. Quantitative measurement performed by Martinelli et.al.<sup>106</sup> showed that there were changes in the elemental concentrations near the cathode and anode surfaces after a spinel crystal was heated in an electric field at approximately 1000°C. An MgO – rich layer was formed at the cathode surface, and was compensated by a slight reduction in the  $[Mg]/[Al]$  ratio in the bulk. It indicated that  $Mg^{2+}$  ions became mobile at elevated temperatures, and  $Mg^{2+}$  vacancies became the current carriers in spinel. Another explanation was that current carriers in spinel at elevated temperature were  $Mg^{2+}$  vacancies produced by the presence of excess alumina.<sup>104, 105</sup> The binary phase diagram of the MgO-Al<sub>2</sub>O<sub>3</sub> system showed that the spinel phase can easily be produced with excess Al<sub>2</sub>O<sub>3</sub>, thus making a large magnesium vacancy concentration possible. As spinel takes an excess of Al<sub>2</sub>O<sub>3</sub> into its solid solution, the concentration of the  $Mg^{2+}$  vacancies was increased, causing an increase in the conductivity of non-stoichiometric spinels.

### **1.3. Spinel powder synthesis**

Like most ceramics, the fabrication of spinel bodies starts from a powder obtained from commercial sources, and is followed by green body forming, sintering and finishing. Knowledge of the nature of the starting powder is of great importance because it influences the subsequent processing stages, and they, in turn, influence the properties of the final product. Any defect existing in the powder will not be cured via these processes. In addition, sintering can serve to exacerbate the existing defects or create other defects. The powder characteristics that are of greatest interest include chemical composition, extent of chemical homogeneity, purity, crystalline phase(s), particle size, particle size distribution, surface area, degree of agglomeration, and quality of agglomeration. These qualities are governed by the method that is used to produce the powder.

The fabrication methods for producing ceramic powders can be divided into two categories: mechanical methods and chemical methods. The mechanical methods involve predominantly grinding or milling for the reduction in size of a coarse, granular material. They are generally used to prepare powders for traditional ceramics from naturally occurring minerals. The chemical methods involve chemical reactions under carefully controlled conditions for the formation of chemicals with desired properties. They are generally used to prepare powders of advanced ceramics from synthetic materials or from naturally occurring materials.<sup>108</sup>

#### **1.3.1. Fabrication of spinel powder**

Although magnesium aluminate spinel is a naturally occurring mineral, the use of the mineral to produce infrared windows and transparent armor is not practical because the

mineral is fairly rare. In addition, natural spinels have various colors due to the presence of the trace impurities which act as the chromophores.<sup>109</sup> The color arises when the trace molecules absorb certain wavelengths in the visible region and transmit or reflect others. Natural spinel rocks are indeed gemstones and very expensive. Growing spinel single crystals via chemical routes is also impractical because they are time-consuming, costly, and difficult-to-control processes.<sup>110, 111</sup> The synthesis of a high purity spinel powder via a chemical route is a much cheaper and easier-to-control process.

Commercially available spinel powders can be divided into two grades: refractory spinel aggregates and high-purity spinel powders. The former is used to produce monolithic and fired refractories for cement rotary kilns, steel-making furnaces, and glass tank regenerators. The latter is used in the production of advanced ceramics such as high energy laser windows and transparent armors. The synthesis of refractory spinel aggregates normally starts from firing a powdered mixture of bauxites and magnesias, and is followed by crushing and grinding of the sintered product.<sup>51</sup> While the purity of refractory spinel aggregates is important regarding to its mechanical, chemical and thermal properties, it is not as critical as in case of the high-purity spinel powder used to produce transparent ceramics.

Since purity is crucial for transparent spinel products, the synthesis of spinel powder requires high purity starting materials and contamination-free techniques. Popularly, a spinel powder is synthesized using a sol-gel method followed by calcination and comminution processes. The most commonly used precursors are alkoxides, nitrates, and sulfate. Wang *et.al.* synthesized spinel powder from aluminum isopropoxide and magnesium methoxide precursors via a freeze-drying method.<sup>112</sup> Cook *et.al.* used

aluminum sec-butoxide and magnesium acetylacetonate with a surface modification technique.<sup>113</sup> Debsikdar produced non-crystalline stoichiometric magnesium aluminate gel-monolith by chemical polymerization reaction between aluminium alkoxide and magnesium salt.<sup>114</sup> Ganesh et.al. used a solid mixture containing aluminum nitrate, magnesium nitrate, and urea with a microwave-assisted combustion technique.<sup>115</sup> Gromov et.al. synthesized spinel powder by burning magnesium nitrate, aluminum nitrate, urea, glycine, and sugar.<sup>116</sup> Nakagawa prepared a spinel powder from an equimolar aqueous solution of magnesium and aluminum sulfates via a freeze-drying method.<sup>117</sup>

### **1.3.2. Powder properties and their influences on the fabrication and the properties sintered spinel**

The important characteristics of a powder can be divided into four categories: chemical composition, phase composition, physical characteristics and surface characteristics.<sup>108</sup> Each of these characteristics has a great influence on the processing of spinel.

#### *1.3.2.1. Chemical composition and phase composition*

The chemistry and phase composition of the starting powder have great influence on the processing, microstructure development, and the final properties of spinel.

As expressed in its molecular formula,  $MgAl_2O_4$ , there are three elements in spinel: magnesium (Mg), aluminum (Al), and oxygen (O). A pure  $MgAl_2O_3$  powder is ideal for obtaining a high optical transmittance for spinel. Any impurities can be excluded from the bulk and accumulate at the grain boundary during recrystallization at firing.<sup>118</sup> The grain

boundary phases then become scattering centers that negatively affect the optical properties of spinel.<sup>62</sup> In practice, trace impurity elements at concentrations less than a few hundred parts per million are unavoidable even in the cleanest powders.<sup>108</sup>

Besides the chemistry, concerns are raised about the morphology of the starting powder. Because the chemical composition of an equimolecular mixture of a pure magnesia and a pure alumina is the same as the chemical composition of a pure stoichiometric spinel, it is difficult to conclude if a powder containing Mg, Al and O is spinel. If magnesia and alumina present as the major or minor phases in a powder, there are four possibilities of what happen to them during firing: (1) they interact and form a new spinel phase, (2) they diffuse into the spinel structure and form a solid solution, (3) they participate in both of the said events, or (4) a part of them participate in the above events while the rest stays as separate phases and become light scattering centers in the sintered product. As a result, a high optical transmittance will not be obtained. Therefore, knowledge of the morphology of the starting powder is of great importance.

As presented in the binary phase diagram of the MgO – Al<sub>2</sub>O<sub>3</sub> system, the spinel phase is highly tolerant. A large amount of Al<sub>2</sub>O<sub>3</sub> can dissolve into the spinel phase at high temperatures (> 1000°C) and form an Al<sub>2</sub>O<sub>3</sub>-rich solid solution. Because this solid solution is stable at high temperatures, care should be taken in the cooling stage of the sintering process to avoid dissolution of the excess Al<sub>2</sub>O<sub>3</sub>.

#### *1.3.2.2. Physical properties*

Physically, a powder is a relatively dry, undispersed accumulation of particulate matter with a macroscopic consistency. It consists of small units, referred to as particles.

The structure of a particle can be fairly complex. Most commonly, particles are divided into two sub-groups, namely, primary particles and agglomerates. A primary particle is the smallest unit in the powder with a clearly defined surface. It can be either a single crystal or a polycrystalline particle, or a glass, and is unbreakable by ultrasonic agitation in a liquid. If any pores are present, they are isolated from each other. An agglomerate is a cluster of primary particles held together by surface forces, by liquid or by a solid bridge. Agglomerates are porous with the pores being interconnected. Figure 4 illustrates the structure of an agglomerate consisting of dense, polycrystalline primary particles.<sup>108, 119</sup>

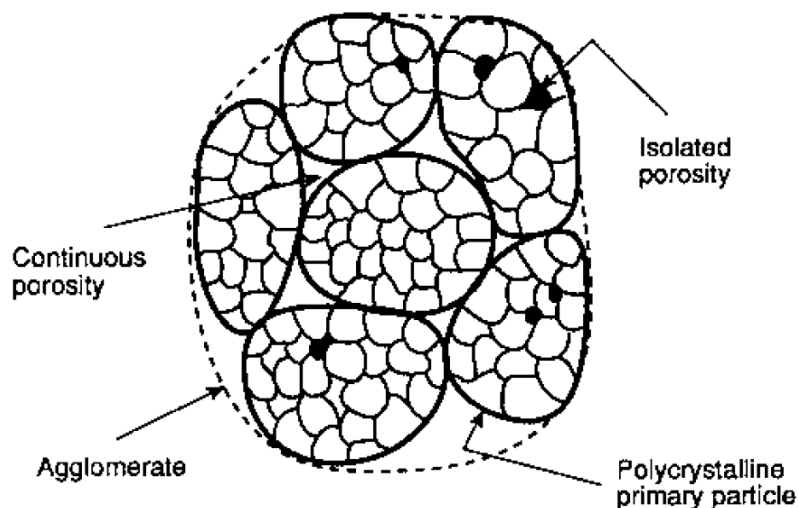


Figure 4. Schematic diagram of an agglomerate consisting of dense, polycrystalline primary particles.<sup>108</sup>

Agglomerates are classified into two types: soft agglomerates and hard agglomerates. A soft-agglomerate is a cluster of primary particles held together by fairly weak surface forces, and can be broken down into primary particles by ultrasonic agitation in a liquid. A hard-aggregate consist of primary particles that are chemically bonded by solid bridges, and cannot be broken down into primary particles by ultrasonic agitation in a liquid.<sup>108</sup>

Densification behavior of a powder compact is mainly influenced by the hardness and the extent of agglomeration of the starting powders. Hard agglomerates retard the compaction of the powders, and cause porosity inhomogeneity in the green compacts.<sup>120</sup> Moreover, because of the strong bonds between the primary particles in a hard agglomerate, the shrinkage rate during sintering is different inside and outside of the agglomerate. This can lead to the formation of microstructural defects such as large inter-agglomerate pores and inhomogeneous grain size distribution in the sintered bodies.<sup>121, 122</sup> Therefore, hard agglomerates are undesirable in the production of ceramics with high density and fine grain. These are two of the key qualities of a high strength transparent spinel.

Other physical properties of a powder including particle shape and particle size distribution have profound effects on powder packing, which, in turn, affects the consolidation of the powder at firing.

Particle shape influences the flow properties and packing of a powder. The trend in ceramic processing is toward increasing the use of spherical or equiaxial particles because they produce better packing uniformity in a powder compact.<sup>108</sup>

Most starting powders for ceramics fabrication have a continuous distribution of particle sizes. The particle size distribution influences the packing of a powder in a trend that a wider particle size distribution gives a higher packing density. An optimum packing occurs when the particle size distribution can be described by the equation:<sup>108, 123</sup>

$$W = \frac{D^n - D_s^n}{D_L^n - D_s^n} \quad \text{Eq. 7}$$

where  $W$  is the cumulative mass fraction of particle finer than a size  $D$ ,  $D_s$  is the smallest particle size in the distribution,  $D_L$  is the largest particle size in the distribution, and  $n$  is an empirical constant used to fit the experimental size distribution.

#### *1.3.2.3. Surface properties*

Surface area, surface structure and surface chemistry are three important characteristics of a powder. The surface chemistry has the most profound influence on the sintering of the powder. Surface impurities may lead to the formation of a small amount of liquid phase at the sintering temperature, which causes selected growth of large individual grains. As a result, a fine uniform grain size would be impossible.<sup>108</sup> Surface impurities can be intrinsic or extrinsic. While intrinsic impurities belong naturally to the powder, the extrinsic impurities are normally chemicals introduced to the powder to assist the sintering process. For instance, lithium fluoride (LiF) is an extrinsic impurity added to spinel powder to promote the liquid phase sintering mechanism in hot pressing. Selection of the sintering additives for spinel should be done carefully because they may give rise to the formation of second phase at grain boundary or color centers the structure of spinel.

#### **1.3.3. The availability and qualities of high-purity spinel powder in the current market**

The commercially available powders for optical grade spinel possess a high purity with more than 99 wt.% being the spinel phase. Table 3 presents the properties of three of the commercial spinel powders. It was mentioned in the literature that Baikowski spinel

was a sulfate-derived powder.<sup>11</sup> However, to the knowledge of the author, the production methods of these powders have not been published.

Table 3. Commercially available spinel powder for optical-grade spinel.

Spinel powder (Manufacturer)	Purity, wt% of the spinel phase	Particle size, $\mu\text{m}$	Surface are, $\text{m}^2/\text{g}$ (BET method)
TSP 15 (Taimei Chemical) <sup>21</sup>	> 99.97	0.1 – 0.3 <sup>(a)</sup>	
S30CR (Baikowski) <sup>124</sup>	> 99.9	0.2 <sup>(b)</sup>	30 ± 5
AHPA (Ceralox) <sup>125</sup>	> 99.99	0.7 – 35 <sup>(b)</sup>	< 10

<sup>(a)</sup> From SEM image      <sup>(b)</sup> Median particle size D<sub>50</sub>

#### 1.4. Fabrication principles for the production of ceramics with superior mechanical properties

The microstructural design of ceramics for applications where outstanding mechanical properties are required involves principally the control of density, grain size and the amount and distribution of any grain boundary phases. In the first place, a high density with controlled grain size and without a glassy phase at the grain boundaries is required for a good mechanical strength. Small grains are the major concerned of high strength ceramics, while coarse grains are desired for a good creep resistance. Secondly, particular microstructures have detailed requirements on particle size, distribution and volume fraction to exploit toughening mechanisms such as phase transformation and micro-crack propagation (crack deflection, crack bowing, and crack tip shielding).<sup>126</sup>

Typically, the fracture strength,  $\sigma_f$ , is plotted against the grain size,  $d$ , as  $\sigma_f$  versus  $d^{-1/2}$ . There were two possible reasons for plotting fracture data in this way. Firstly, it was because of the Hall-Petch equation:<sup>16, 100, 127</sup>

$$\sigma_f = \sigma_y + k_y d^{-1/2} \quad \text{Eq. 8}$$

where  $\sigma_y$  is the yield stress for the easiest slip system of a single crystal and  $k_y$  is a constant. Secondly, it was because of the Griffith equation that predicts the relations between the fracture stress and the critical crack length,  $c$ . The fracture stress of a brittle solid under plane stress is

$$\sigma_f = \left( \frac{2E\gamma}{\pi c} \right)^{1/2} \quad \text{Eq. 9}$$

and under plane strain is

$$\sigma_f = \left( \frac{2E\gamma}{\pi(1-\nu^2)c} \right)^{1/2} \quad \text{Eq. 10}$$

where  $E$  is the Young's modulus,  $\gamma$  is the surface energy per unit area, and  $\nu$  is the Poisson's ratio of the solid.<sup>127, 128</sup> These equations results in the  $\sigma_f$  versus  $d^{-1/2}$  relation:<sup>127</sup>

$$\sigma_f = \frac{K_{IC}}{Y} d^{-1/2} \quad \text{Eq. 11}$$

where  $K_{IC}$  is the toughness of the solid, and  $Y$  is a constant.

Generally, efforts to obtain high density products can take one or more of four alternative paths, namely, the use of solid solution additives, the use of very carefully prepared powders, the use of conventional sintering methods, and the use of second phase additives.<sup>126</sup> Each method has its own advantages and disadvantages. The method of using solid solution additives is convenient as was found in the alumina/magnesia system,<sup>129, 130</sup> but the number of system for such additives is small. The method of using fine, sinterable powder with attention to quality factors such as purity, morphology, particle size, degree of agglomeration, quality of agglomeration, and extent of chemical homogeneity is a very effective way to achieve high density. Its disadvantage is that the powder can become very expensive. The method of using conventional sintering methods, such as hot press, hot iso-static press, and controlled rate sintering, is perhaps the most reliable way to obtain high density product. However, it can be expensive, and there might be a limitation in the size of the products as in case of spark plasma sintering. The method of using second phase additives normally involves formation of a liquid phase while firing. This is the cheapest, most convenient and most commonly used method to attain a high density, but the presence of the second phase can degrade the mechanical and optical properties of the products. In each of these methods, a mechanism is provided to enhance the rate of densification.

### **1.5. Sintering additives and methods of introduction**

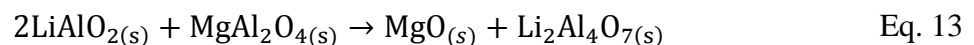
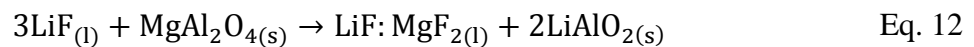
The purpose of adding impurities, either sintering additives or dopants, to a pure spinel powder is normally to improve the performance of the sintering process and/or to enhance or change the qualities of the product. Although the use of sintering additives and dopants in the fabrication of transparent spinel is limited, certain type of chemicals are

usable. They can be solid-solution sintering additives such as MgO and Al<sub>2</sub>O<sub>3</sub> that can diffuse into the spinel grains without changing their crystalline structure, or they can be liquid-phase sintering additives that do not form grain boundary phases and color centers in the sintered product. These chemical should be distributed homogeneously in the powder to have the best effects without degrading the mechanical and optical properties of the final product.

### 1.5.1. Sintering additives in fabrication of transparent spinel

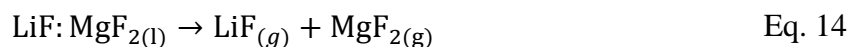
#### 1.5.1.1. Lithium fluoride

The most commonly used sintering additives for transparent spinel produced by HP and HIP is lithium fluoride, LiF. The mechanism by which LiF assisted the sintering process as proposed by Rozenburg et.al.<sup>29, 131</sup> was that LiF played the role of a liquid-phase sintering additives: Just before the melting point of LiF, it begins to react with MgAl<sub>2</sub>O<sub>4</sub> to form LiAlO<sub>2</sub> or LiAl<sub>4</sub>FO<sub>6</sub> along with a fluoride melt:

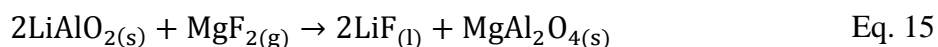


Spinel containing Li impurities would contain oxygen vacancies that might be able to enhance diffusion of the atomic components of MgAl<sub>2</sub>O<sub>4</sub>. Therefore, the formation of the fluoride melt at the grain boundaries would be expected to promote sintering or coarsening at the late stage of sintering.

The presence of the fluoride melt (LiF:MgF<sub>2</sub>) facilitated the rearrangement of the spinel particles and enhanced diffusion of the atomic components of MgAl<sub>2</sub>O<sub>4</sub>. Upon further heating, the vapor pressures of the fluoride melt increased, and the following reaction took place:



As the temperature approaches 1000°C, LiF began to leave the powder compact, and then highly active MgF<sub>2</sub> reacted with LiAlO<sub>2</sub>, leading to the reformation of spinel:



Once LiF completely leaves the powder compact at higher temperatures, its benefit as a sintering additive is no longer present.

The removal of LiF from the spinel powder compacts during sintering is of extreme importance for the mechanical and optical properties of the sintered products. White and Kelkar<sup>132</sup> demonstrated that the fracture behavior of a hot pressed spinel was negatively affected by the residual LiF at its grain boundary. Villalobos et.al.<sup>30</sup>, on the other hand, showed that the formation of LiAlO<sub>2</sub> accompanied by MgO-rich regions that did not sinter well and resulted in opaque white regions in the otherwise transparent matrix.

Factors that govern the presence of the residual LiF in the sintered spinel include the amount of LiF that is added to the starting powder, the method by which these two components are mixed together to form a homogeneous mixture, and the firing conditions.

### 1.5.1.2. Solid-solution sintering additives

As the crystal structure of spinel is highly tolerant, solid-state reactions forming  $\text{MgAl}_2\text{O}_4$  occur by counter-diffusion of the  $\text{Mg}^{2+}$  and  $\text{Al}^{3+}$  ions through the relatively rigid oxygen lattice of the spinel.<sup>133</sup> The chemical process of these reactions is presented in Figure 5.

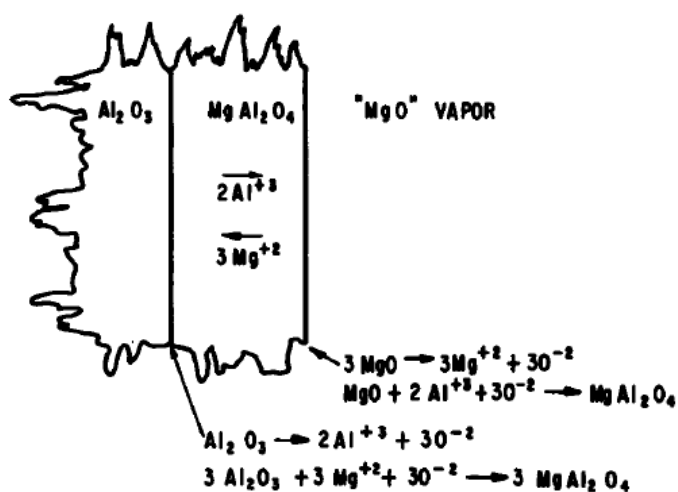


Figure 5. Schematic section through a growing  $\text{MgAl}_2\text{O}_4$  layer.<sup>133</sup>

Off-stoichiometric transparent spinels were generally produced in the alumina rich side because of the improved strength and/or hardness. In these cases, the starting powder was either a mixture of a pure spinel, alumina and magnesia powders,<sup>12</sup> or a mixture of precursors containing Mg and Al.<sup>7</sup>

### 1.5.2. Methods of introducing sintering additives to spinel powder

Sintering additives and dopants can be introduced to spinel powder by mixing or via colloidal processing. Each method has its own advantages and disadvantages. Mixing, either in a dry state or in an aqueous medium, is a simple technique but it might cause

inhomogeneity locally. Colloidal processing is more complicated because it requires a chemical process, heat treatment and pulverization. However, this method can be employed to uniformly distribute a small amount of the dopant to a powder.

#### *1.5.2.1. Mixing*

The most commonly used method for adding LiF to spinel powders is by dry mixing. It can be as simple as by mixing/grinding using a mortar and pestle,<sup>30</sup> or ball milling with alumina media in a polyethylene container,<sup>29</sup> or shaking in a high density polyethylene container with or without high purity alumina mixing balls.<sup>14, 134</sup>

There are three components in a mixing process, namely, the transfer of groups of adjacent particles from one location in the mass to another – ‘convective mixing’, the distribution of particles over a freshly developed surface – ‘diffusive mixing’, and the setting up of slipping planes within the mass – ‘shear mixing’.<sup>135, 136</sup>

Historically, most ceramic fabrication processes involving mixing of the starting powders or of the main powders with a sintering additives. The simplest mixing methods are agitating, shaking and milling of the dry powders. These methods are likely to develop a mixture with a randomly distributed clusters of the minor component as illustrated in Figure 6(b). As a result, the solid produced from this mixture is not homogeneous and has poor final properties. Ideally, the disperse components are expected to be organized into a pattern as shown in Figure 6(a) to minimize any variation in the powder mixture.

Factors that affect the effectiveness of powder mixing include the volume fraction of the various ingredients, the present of moisture in the powder, the humidity of the environment, the surface condition of the powder, the shape and size of the aggregates and

primary particles, the electrostatic properties of the powders, the tendency of the powders to disintegrate during handling, mixing time and mixing equipment used.

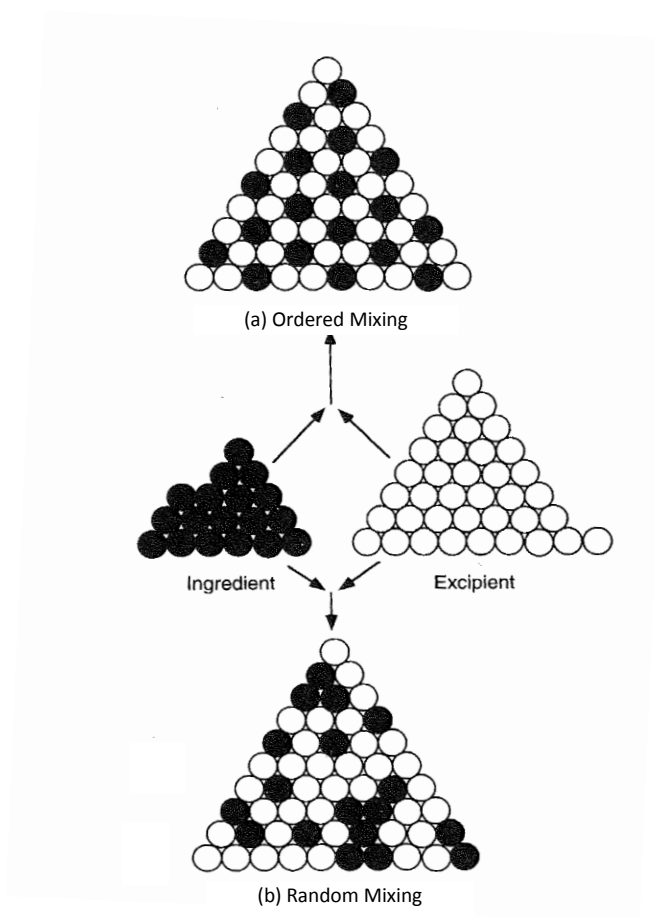


Figure 6. Schematics of (a) ordered mixing and (b) random mixing.<sup>137</sup>

Wet mixing, which is the agitation of the powders in a liquid, improves the dispersion of the powder particles and reduces clustering but the homogeneity of resulted mixture is still poor. The most commonly used liquid for wet mixing is water. By adding a sufficient amount of the liquid into an agitating mixture, the solid surfaces of the particles in lateral motion are separated by the liquid. Subsequently, the dry friction between solid particles is eliminated and a lubricated friction is developed. As a result, the dispersion of the powder particles is improved. The introduction of surfactants in wet mixing reduces

agglomeration thereby further reduce the inhomogeneity of the resulted mixture but does not fully address the issues of clustering and agglomeration.

In ceramic production, a sintering additives is normally added to the powder to be sintered in form of a finely ground powder, and a very small amount of the sintering additives is used to avoid degradation of the final product. For instance, the typical amount of LiF added to HP and HIP processed spinel is 0.5 – 1 wt%.<sup>14, 15, 29</sup> The introduction of a small amount of very fine sintering additives into a ceramic powder would result in a heterogeneous mixture due to clustering and agglomeration caused by the cohesiveness of the powder. It is not expected in transparent ceramics where an extreme homogeneity is a must to avoid the formation of any light scattering centers. Therefore, alternative strategies for introducing the sintering additives to the powder to be sintered have been sought.

#### *1.5.2.2. Introduction of the sintering additives via colloidal processing*

Encapsulation of a powder by a dopant is the most effective way to completely disperse the two components. Sometimes mixing of a very fine powder and a very coarse powder is very successful despite the expectation that the fines would segregate through the assembled mixture at the end of the mixing process. In such case, the finer powder is electrostatically attached to the coarser fine particles to produce a heterogeneous microencapsulated system.<sup>138</sup> However, coating would be more homogeneous via a colloidal process. In this case, the powder to be coated is dispersed into a solution of the precursor that contains the ions of the dopant. The surface of the powder plays the role of a heterogeneous nucleation site where the precipitates of the dopant grow once they are formed. The precursor is then chemically treated so that nuclei of the precipitates

containing the ions to be doped are formed and grow. The subsequent process is to heat treat the resulted material to remove the unwanted chemicals, i.e. solvents. Using this coating method, a monolayer or multilayers of the dopant is assembled on the surface of the host particles. As a result, the formation of the dopant clusters observed in powder mixing is avoided. This method is popularly used in producing semiconductors, fuel cell materials and other ceramics,<sup>139-142</sup> and was used in this work to dope  $\text{Al}_2\text{O}_3$  into the spinel powder.

## **1.6. Densification of transparent polycrystalline spinel**

### **1.6.1. Densification of polycrystalline ceramics**

The fabrication of a polycrystalline ceramic is normally a firing process that increases the density and the strength of a fine-grained, porous compact of ceramic particles by bonding adjacent particles into a solid. Changes that occur during firing of the compact can be quite complicated depending on the properties of the particular material being used as well as the processing method being employed. The initial changes that may occur consist of the evaporation of the existing volatiles and the decomposition or combustion of certain chemicals, including the binder being used. At higher temperatures, phase changes and polymorphic transformations might present. On further heating, either a viscous liquid or sufficient atomic mobility in the solid particles is developed to permit chemical reactions, grain growth and sintering.<sup>143</sup>

There are not as many changes as mentioned above that occur during the firing process of transparent polycrystalline spinel. It is because the fabrication of this material is normally started with a high-purity crystalline spinel powder. Since spinel is refractory and

monomorphous, there is no phase change or polymorphic transformation during firing. Besides, the use of binders is eliminated and the addition of sintering aids is minimized to avoid the formation of any second phase that can diminish the transparency of the host material. Therefore, decomposition, combustion, and chemical reactions are not likely to occur during firing. In this case, sintering and grain growth are of great importance.

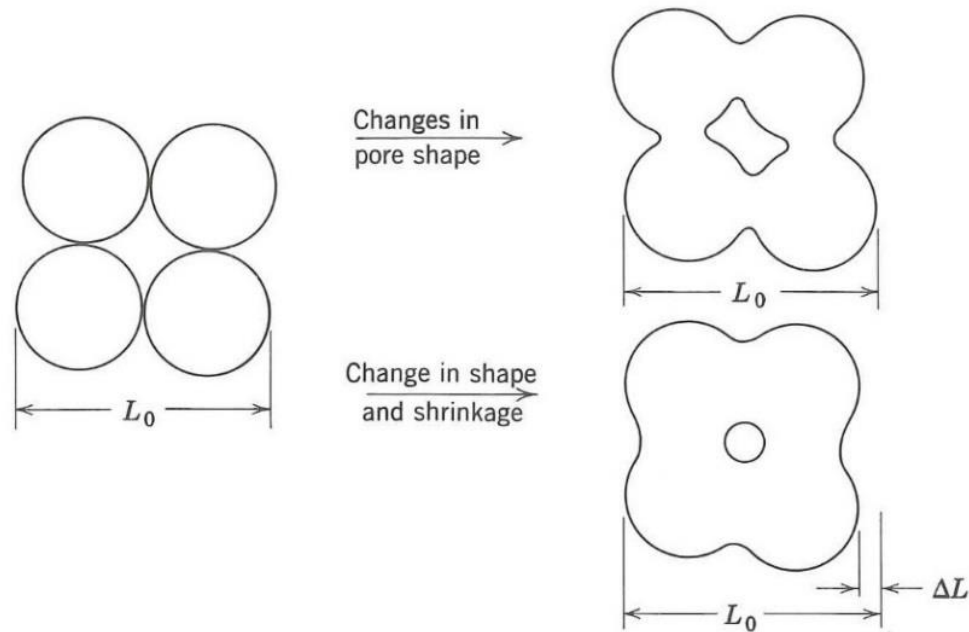
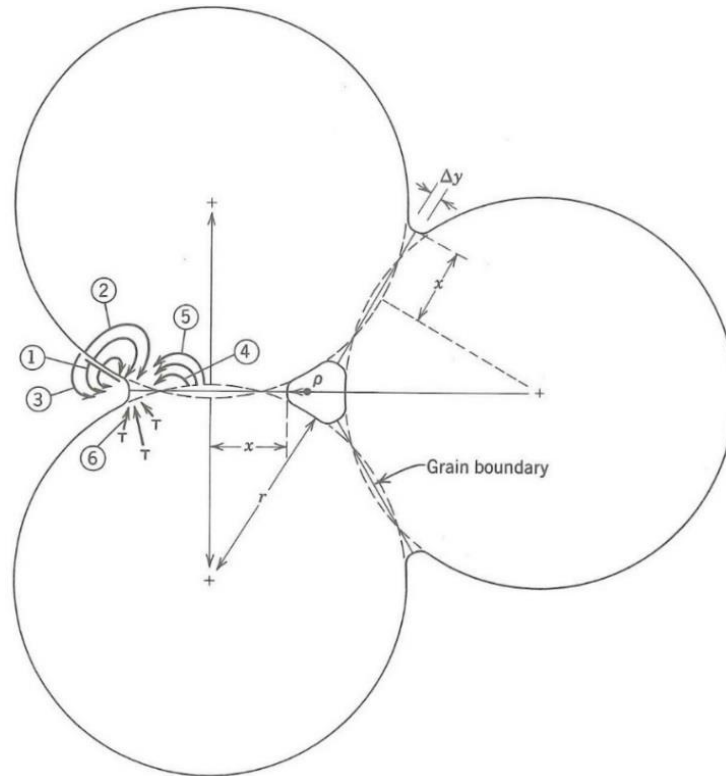


Figure 7. Changes in pore shape and size during sintering. Changes in pore shape do not necessarily require shrinkage.<sup>143</sup>

Three major changes that occur during sintering include an increase in the grain size, a change in the pore shape, and a decrease in the porosity. These changes are illustrated in Figure 7. The initial shapes of the pores change into channels or isolated spheres. Although a change in the pore shape does not necessarily require a change in the pore size, both size and shape of the pores eventually change during the firing process. The pores become more spherical in shape and smaller in size. As the result, the porosity of the compact is reduced and the density is increased. The driving force for sintering is a decrease

in the surface free energy of the powdered compact by replacing solid-vapor interfaces by solid-solid interfaces. The driving forces for grain growth process is the difference in free energy of material on the two sides of a grain boundary that allows the grain-boundary to move toward its center of curvature.<sup>143</sup>



Mechanism Number	Transport Path	Source of Matter	Sink of Matter
1	Surface diffusion	Surface	Neck
2	Lattice diffusion	Surface	Neck
3	Vapor transport	Surface	Neck
4	Boundary diffusion	Grain boundary	Neck
5	Lattice diffusion	Grain boundary	Neck
6	Lattice diffusion	Dislocations	Neck

Figure 8. Alternate paths for matter transport during the initial stage of sintering.  $x$  is the radius of the neck, and  $r$  is the diameter of the particle. (From M.A. Ashby)<sup>143</sup>

At the initial stage of the sintering process, there is a matter transport because of the differences in vapor pressure and concentration at various parts of the system. The pressure of vapor in equilibrium is less at a concave than at a flat surface, and less at a flat surface than at a convex surface as based on the Kelvin's equation:<sup>144</sup>

$$p = w - \frac{T\sigma}{\rho - \sigma} \left( \frac{1}{r} + \frac{1}{r'} \right)$$

where  $p$  is the pressure of vapor in equilibrium at a curved surface the condense phase,  $w$  is the pressure of vapor in equilibrium at a flat surface of the condense phase,  $T$  is the surface tension,  $\sigma$  is the density of the vapor,  $\rho$  is the density of the condense phase, and  $r$  and  $r'$  are principal radii of curvatures of the surface bounding the two phases, reckoned positive when concave towards the vapor. Therefore, matter evaporates from the surfaces that have larger positive radius of curvatures and deposits on the ones that have smaller radius of curvatures. This kind of mater transfer is illustrated as mechanism number 3 in Figure 8. In addition to the evaporation-deposition path, matter can be transferred from the particle surface, particle volume or from the grain boundary between particles by surface, lattice, or grain boundary diffusion. Matter transfer increase the contact area between particles and decrease the distance between particles centers. However, only transfer of matter from the particle volume or from the grain boundary between particles causes shrinkage and pore elimination. The shrinkage of a compact is proportional to the two fifths power of time:<sup>143</sup>

$$\frac{\Delta V}{V_0} = 3 \left( \frac{20\gamma a^3 D^*}{\sqrt{2}kT} \right) r^{-6/5} t^{2/5} \quad \text{Eq. 16}$$

where  $\Delta V$  is the change in volume of the compact,  $V_o$  is the initial volume of the compact,  $\Delta L$  is the change in length of the compact,  $L$  is the initial length of the compact,  $\gamma$  is the surface tension,  $a^3$  is the atomic volume of the diffusing matter,  $D^*$  is the self-diffusion coefficient,  $k$  is the Boltzmann constant,  $T$  is the temperature,  $r$  is the radius of the initial particle, and  $t$  is the time.

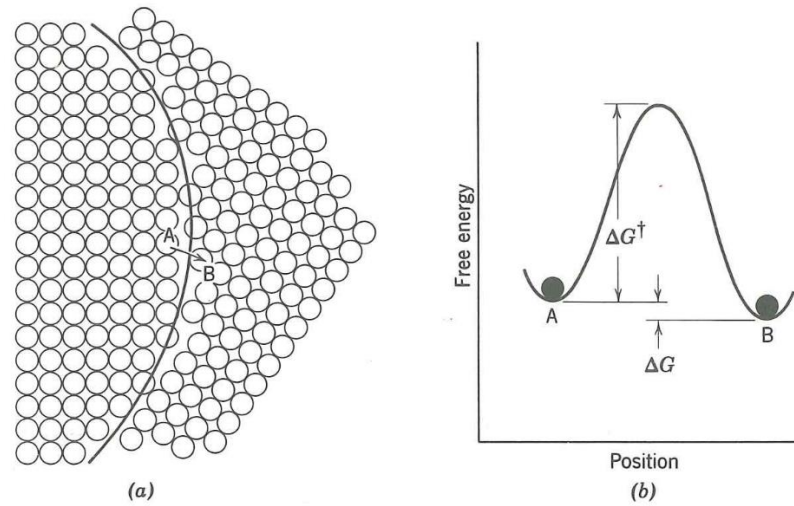


Figure 9. Schematic of grain growth. (a) Structure of boundary; (b) energy change for atom jump.<sup>143</sup>

Besides the reduction in volume and porosity of the powder compact, a number of grains shrink and disappear while the others grow causing an increase in the average grain size. The driving force for this process is the decrease in total interface energy. An interface energy is associated with the boundary between individual grains. There is a free-energy difference across a curved grain boundary which is given by:<sup>143</sup>

$$\Delta G = \gamma \bar{V} \left( \frac{1}{r_1} + \frac{1}{r_2} \right) \quad \text{Eq. 17}$$

where  $\Delta G$  is the change in energy on going across the curved interface,  $\gamma$  is the boundary energy,  $\bar{V}$  is the molar volume, and  $r_1$  and  $r_2$  are principal radii of curvature. The difference in the free energy of material on the two sides of a grain boundary is the driving force that makes the boundary move toward its center of curvature (Figure 9). The rate at which a boundary moves is proportional to its curvature and to the rate at which atoms can jump across the boundary.

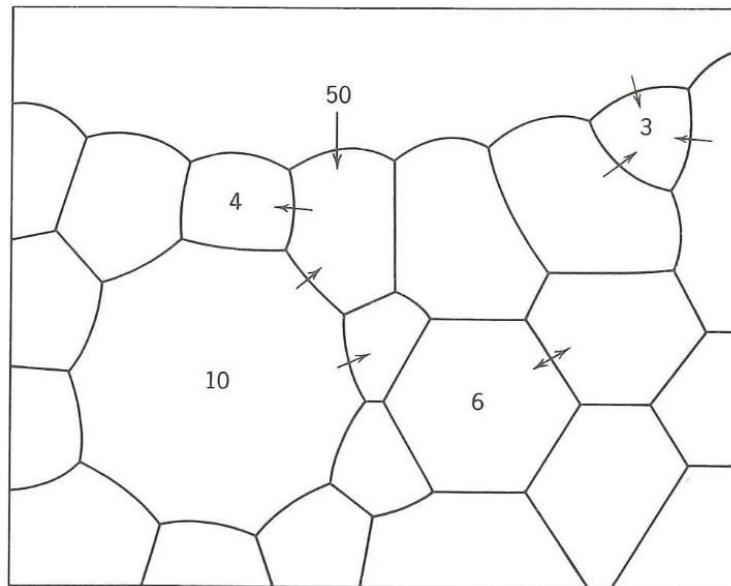


Figure 10. Schematic drawing of grain boundaries migration. The numbers indicate the number of sides of each grain. The arrows indicate the directions in which boundaries migrate. From J.E. Burke.<sup>143</sup>

For oxide ceramics, the traditional sintering practice is to heat the powder compact to its sintering temperature at a certain rate and hold it at this temperature until the maximum density is reached. The final stage of this sintering cycle is often accompanied with secondary recrystallization, so-called exaggerated grain growth. This phenomenon is likely to occur when continuous grain growth is inhibited by the presence of minor amounts of second phases or by porosity. Under these conditions, only boundaries with a much

larger curvature than the average are able to move (Figure 10), thereby the grains with highly curved boundaries are able to grow whereas the matrix material remains uniform in the grain size. The driving force for secondary recrystallization is the lower surface energy of the large grains compare to the higher surface energy of the adjacent smaller grains.<sup>143,</sup>

145

### 1.6.2. Sintering kinetics of spinel

According to Coble,<sup>129</sup> sintering could be divided into three stages: The initial stage begins with inter-particle diffusion and lasts until the contact area increased from zero to  $\cong$  0.2 of the cross-sectional area of the particle; The intermediate stage begins after grain growth; The final stage begins when the pore phase is eventually pinched off.

Braton<sup>146, 147</sup> demonstrated that sintering of spinel powders was governed by volume diffusion, and the temperature dependence of the apparent diffusion coefficient,  $D$ , could be presented by:

$$D = D_0 e^{\left(\frac{-E}{RT}\right)} \quad \text{Eq. 18}$$

where  $D_0$  is the maximum diffusion coefficient (at infinite temperature),  $E$  is the activation energy,  $R$  is the universal gas constant,  $R = 1.9872 \times 10^{-3} \text{ kcal.K}^{-1}.\text{mol}^{-1}$ , and  $T$  is the absolute temperature. The values of  $D_0$  and  $E$  were dependent of the stage of sintering. In the initial stage of sintering,  $D_0 = 18.6 \text{ cm}^2/\text{s}$ , and  $E = 116 \text{ kcal/mol}$ .<sup>146</sup> In the intermediate stage sintering,  $D_0 = 157 \text{ cm}^2/\text{s}$ , and  $E = 118 \text{ kcal/mol}$ .<sup>147</sup> Although these studies used spinel powders of different sources with different average particle sizes, the activation energy was

fairly consistent. Thus, it was concluded that a volume diffusion mechanism was operative for both stages of densification.

Grain growth for  $\text{MgAl}_2\text{O}_4$  followed the expression: <sup>147</sup>

$$G^2 - G_0^2 = Kt \quad \text{Eq. 19}$$

where  $G_0$  is the initial grain size in  $\mu\text{m}$ ,  $t$  is the duration in minutes, and  $K$  is the rate constant,  $\text{cm}^2/\text{s}$ . The temperature dependence of  $K$  was given by:

$$K = 51.3e^{-\frac{E}{RT}} \quad \text{Eq. 20}$$

where  $E$  is the activation energy of grain growth, for spinel  $E = 110 \text{ kcal/mol}$ ,  $R$  is the universal gas constant,  $R = 1.9872 \times 10^{-3} \text{ kcal.K}^{-1}.\text{mol}^{-1}$ , and  $T$  is the absolute temperature. The mobility of the grain boundary in magnesia-rich spinel was found to be greater than that in stoichiometric and alumina-rich spinels by two to three orders of magnitude. Within the alumina-rich field, the mobility varies by less than a factor of 10 over the composition range  $1 < n < 1.56$ . Nearly stoichiometric spinels ( $1 < n < 1.07$ ) from a variety of sources and starting materials exhibit boundary mobility within a factor of 5 at a fixed temperature, showing an impurity tolerance which has not been found in other ionic solids. <sup>148</sup>

### 1.6.3. Sintering techniques

Transparent spinel is a difficult-to-sinter material because it requires a high sintering temperature and no second phase is permitted. The liquid phase of a stoichiometric spinel is not formed until  $2122^\circ\text{C}$  during a heat treatment.<sup>4</sup> Therefore,

physical and/or chemical sintering aids are needed in order to lower the sintering temperature and promote the sintering process. In ceramics processing, the least expensive way to promote sintering is to use sintering additives. However, care should be taken when using sintering additives for advanced ceramics because the sintering aid once becomes the second phase in the product might have negative effects on the qualities of the product. The other method is to apply pressure-assisted sintering techniques, such as hot-press, hot iso-static press, and spark plasma sintering. Multi-stage sintering has also been developed.

The most commonly used sintering aid for transparent spinel is lithium fluoride, LiF. It has been used widely for HP and HIP of spinel because it helped to obtain a near-theoretical density at reduced sintering temperatures.<sup>7, 134</sup> Other types of sintering aids were also used but the transparency of the final product was not as good as the one with LiF. Bratton was able to obtain a total transmittance of 67-78% in the visible region by sintering spinel at 1800 – 1900°C with CaO addition.<sup>149</sup> However, a glassy phase was observed at trigranular junctions. Tsukuma was able to reduce the HIP temperature drastically to 1300°C by adding a small amount of B<sub>2</sub>O<sub>3</sub>.<sup>150</sup> Although a transmittance of above 70% was obtained in the visible region, irregular grain growth was also observed. Mroz *et.al.* has recently succeeded in using Y<sub>2</sub>O<sub>3</sub> as a dopant to improve the mechanical strength for spinel-based infrared windows/domes, but it was not clear if they could obtain a high transmittance in the visible region.<sup>35</sup>

HP and HIP with or without pre-sintering are of the most reliable sintering techniques for high density ceramics. However, due to their limited heating rates, they are energy consuming and not capable of grain growth restraining. Exacerbated grain growth, so called secondary recrystallization, is normally harmful to the mechanical properties of

the material. It has been well documented that the strength of meso-scopic grains (typically 10-1000  $\mu\text{m}$ ) and micro-scopic grains (typically 0.01 - 10 $\mu\text{m}$ ) is strongly size-dependent in a trend that a larger grain size results in a lower strength.<sup>7, 151, 152</sup> Therefore, alternative sintering routes is needed to shorten the sintering time and/or to lower the sintering temperature, thereby reducing the grain growth.

Spark plasma sintering (SPS), so-called field-assisted sintering, has recently been taken into consideration because this technique allows much faster heating and cooling rates (up to 600°C/min or more), which help to minimize grain coarsening.<sup>19-27</sup>

Chen and Wang<sup>145</sup> proposed a two stage sintering cycle, in which an yttria powder compact was heated to a higher temperature to achieve an intermediate density, then cooled down and held at a lower temperature until it is fully dense. They achieved samples with 60 nm average grain size, and concluded that the intermediate densities higher than 75% were adequate for the second step sintering of yttria. Bosisova et.al.<sup>153</sup> also used a similar two-stage sintering process for alumina and found that the intermediate density should be about 92%. However, the highest density obtained by their process was only 98.8% of the theoretical density. In another practice on alumina, Reddy et.al.<sup>154</sup> developed a multi-stage spark plasma sintering, in which a porous powder compact was heated up and held for 5 minutes at different temperatures, 0.45  $T_m$ , 0.5 $T_m$  and 0.55 $T_m$  (where  $T_m$  is the melting point in °C). They were able to increase the hardness for alumina but the samples were not fully dense. The final density of their samples was only 97-98% of the theoretical density.

### 1.6.3.1. Hot pressing of transparent spinel

Hot pressing, as being defined by German<sup>155</sup>, is a “*high-pressure, low-strain-rate forming of a powder or powder compact at a temperature high enough to induce sintering and creep processes*”.

A hot press is shown schematically in Figure 11. The material to be sintered is placed in a die set which includes a die, a die sliding sleeve, two punches and spacers. The die is heated up by a high frequency electromagnetic field generated from an induction coil. The pressure applied on the punches is controlled independently from the inductive power. Since the penetration of the magnetic field into the die is just a few millimeters, the thermal energy transferred through the die is mostly by conduction. The heating is normally controlled at a low rate in order to avoid a high temperature difference between the surface and the core. Because of its low productivity and a high maintenance cost for the die, the use of a hot press in ceramic fabrication is limited.

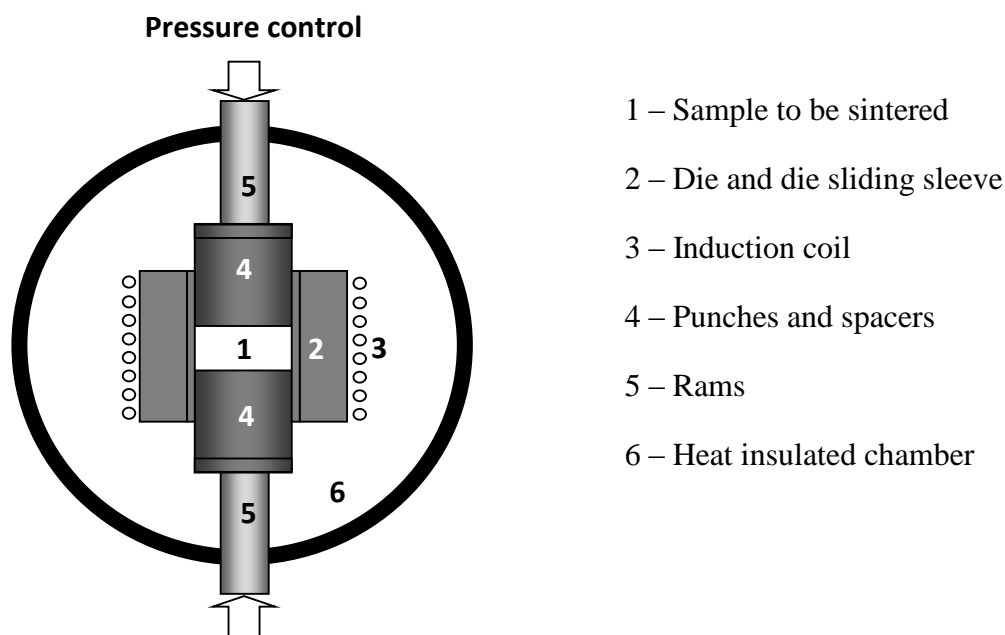


Figure 11. Schematic of the hot pressing process.

For hot-press processing of transparent spinel, the heating rate is quite low, typically lower than 10°C/min, and the soaking time at the sintering temperature is long. For example, Reimanis et.al. heated a LiF-doped spinel powder at the rate of 2°C/min and held at 1550°C for 2 hours to obtain a transparent spinel with an average transmittance of 85%.<sup>14, 85</sup> Due to the long processing time at high temperatures, the HP-processed spinel normally has a large average grain size, typically in the range of micrometers, or sometimes hundreds of micrometer.

#### *1.6.3.2. Hot isostatic pressing of transparent spinel*

Hot isostatic pressing (HIP) is a process that heats a powder compact in a pressurized containment vessel at a temperature high enough to induce sintering and creep processes.

A hot isostatic press often requires pre-sintering to obtain a dense ceramic product. A mixture of the powder to be sintered and a binder is pre-formed before sintering. The most commonly used pre-form methods are cold isostatic press and slip casting. The pre-formed powder compact will then be fired to provide it with a strength and to burn out the binder. HIP-post-sintering of transparent spinel is carried out at a high pressure and a high temperature, typically in the range of 150-200MPa and 1300-1500°C, respectively.<sup>12, 83, 156-159</sup> Another method is to HP the powder prior to HIP.<sup>7, 15</sup> The advantage of the HIP over the HP and the SPS techniques is that it can sinter products with complicated shapes.

### *1.6.3.3. Spark plasma sintering of transparent spinel*

Spark plasma sintering (SPS) is a short-time sintering technique that simultaneously applies a uniaxial pressure and a high-density direct current to a conductive die that contains the powder to be sintered. The technique was developed based on the invention of Inoue<sup>160, 161</sup> in the early 1960s. However, the original idea was much older with a patent granted in 1933 describing a method in which an electric current was passed through a metal powder compact to assist the sintering process.<sup>162</sup> The idea of Inoue's invention was to use the spark in an electric discharge machine to assist the sintering of metal or ceramic powders. The machine was designed so that a pulsed direct current was applied simultaneously with a uniaxial pressure to consolidate a porous powder compact in a conductive die set. The hypothesis of this technique was that the spark discharge within the powder compact would develop an electrical spark between particles thereby partially ionize the particles at their mutually contacting surface. Together with the mechanically applied pressure, a firm fusion was expected to occur. Even if the ionization did not take place, the spark discharge would result in a concentration of a sufficiently high temperature at the region of discharge to cause interfusion. After the initial fusion, the bonding between particles was presumably further secured by the passage of the electric current through the body without a substantial development of sparking to result in the Joule heating effect. The die set would also be heated up due to the Joule effect as the electric current passed through it. The heat from the die would be transferred to the powder compact and contribute to the sintering process.

After the patent of Inoue's invention was expired, various companies in Japan, Germany and America started manufacturing the SPS equipment based on the invention.

Although Inoue recommended this technique for producing relatively porous or low density bodies, the current development of the SPS equipment has demonstrated that it can be used for producing fully dense samples, of which transparent polycrystalline spinel is an example.

Figure 12 is the schematic of the SPS process. It is similar to the HP process but its heat source is different from that of the HP process. In case of the SPS, a low-voltage high-density pulsed DC current is applied through a conductive die and thus acts as the heat source by the Joule effect. Since Joule heating provides a high heating rate, the processing time of the SPS is much shorter than that of the HP or HIP processes. The mechanical pressure that is applied on the sample together with the electrical energy also contributes to shortening the consolidation times, and thereby prevents the development of a coarse microstructure.<sup>163-168</sup>

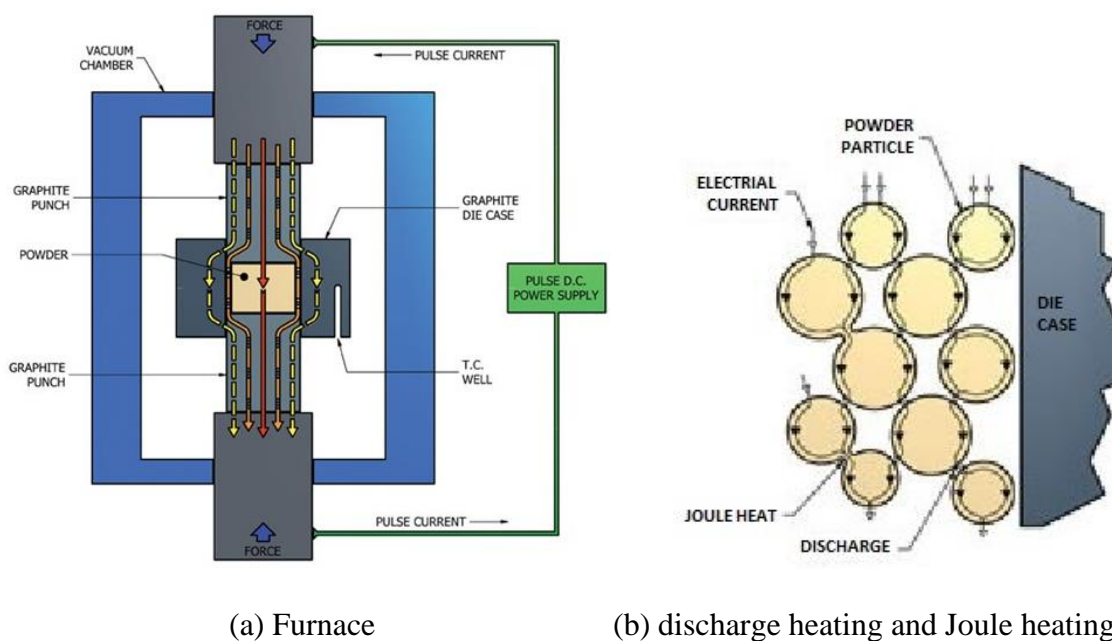


Figure 12. The schematic of the SPS process (taken from Ceramic Industry Magazine<sup>169</sup>)

Although sparking or plasma was expected during the SPS process, there was no direct evidence of their existence. Furuya et.al.<sup>170</sup> were able to detect an electric noise during SPS and presumed that it corresponded to the plasma generation. Yamaki et.al.<sup>163</sup> proposed that the plasma was generated among powder particles of the material to be sintered and activated the particle surfaces. Shen et.al.<sup>171</sup> also suggested that the densification was enhanced in the initial part of the sintering cycle by a local spark-discharge among contacting particles. However, Hulbert et.al.<sup>172</sup> claimed that there was no plasma, sparking or arcing present during the SPS process, either during the initial or in the final stages of sintering, for both conductive and non-conductive materials.

A series of investigations led by Munir et.al.<sup>173-175</sup> was carried out in an attempt to better understand the SPS process. The direction of the pulsed current was found to have no effect on the thickness of the product layer in a Mo-Si-Mo multilayer assembly. In addition, the growth rate of the product layer was found to be independent of the pulse pattern. They suggested that the current did not alter the reaction mechanism because the activation energies for the growth of the product phase with and without current were the same, even though the growth rate of the product layer under a current was significantly higher than that in the absent of the current. They also simulated a complicated distribution of the current and the temperature in the radial and axial directions of the SPS process. In the axial direction, the highest current density was seen at the exposed portions of punches. In the radial direction, the current did not pass through alumina, but it passed through copper with the highest density observed at the lateral surface of the sample. Consequently, the temperature distribution across alumina was not constant while it tended to become homogeneous across copper.

The SPS has been used for producing transparent spinel since the late 2000's but a standard SPS process has not been well defined for a high-strength transparent spinel. The consolidation of spinel was found to finish at a relatively low temperature, typically in the range of temperature from 1250°C to 1350°C without using a sintering additives. Although most of the samples reached a transmittance of approximately 80% in the infrared region, they did not reach the theoretical transmittance in the visible region. Nanometer-size pores were found at the triple point junctions of spinel. These pores play the role of the light scattering centers that lower the transmittance of SPS spinel to less than 70% in the visible region.<sup>19-28</sup> As the transmittance of spinel in the visible region is also important for many applications, besides the quality of the starting powder needing to be enhanced, the SPS conditions need to be optimized to produce samples with a better transmittance in the visible region.

One of the parameters that can be manipulated to optimize the SPS condition is the heating rate. Morita et.al.<sup>22</sup> have demonstrated that for the fabrication of transparent spinel with a sub-micron grain size, a low SPS heating rate was more effective than a high SPS heating rate: At the 550 nm wavelength, the transmittance of the 1.8 mm-thick samples heated at the rate  $\leq 10^\circ\text{C}/\text{min}$  could reach approximately 50%, while the transmittance of the samples heated at the rate  $\geq 50^\circ\text{C}/\text{min}$  could not reach 25%. Their work, however, did not investigate the effects of the dwell time on the properties of the samples. In an independent work, Bonnefont et.al.<sup>28</sup> demonstrated that the sample could reach a transmittance of 74% at the 550nm wavelength with a heating rate of 100°C/min to 800°C, 10°C/min from 800°C to 1100°C, 1°C/min from 1100°C to 1300°C without soaking at the highest temperature, and with a subsequent annealing at 1000°C for 10 minutes. Although

this transmittance value was higher than those published before,<sup>19, 24, 25, 176</sup> it was uncertain if the described heating profile was optimal because besides the heating rate, the samples were also sensitive to the impurity of the starting powder.

Black, gray, brownish and yellowish discoloration was a typical phenomenon in the SPS-processed ceramics,<sup>26, 63, 177-179</sup> but the interpretation of the causes of this issue has not been unified. According to Roy,<sup>61</sup> the residual sulfur in the sulfate derived spinel powder may result in a yellow discoloration of the product if it is not sintered under vacuum. Anselmi-Tamburini et.al.<sup>180</sup> interpreted this phenomenon as was due to the formation of color centers in the form of oxygen vacancies after exposing to a reducing environment at high temperatures. Bernard-Granger et.al.<sup>26</sup> considered the diffusion of carbon from the graphite die as the main source of light absorption in SPS-processed spinel. Wang and Zhao<sup>19</sup> attributed this phenomenon to the stress-induced dislocations formed during the fast densification in the SPS. These interpretations looked at the problem without considering the similarity between the HP method and the SPS method as well as the difference in the transmittance of the products consolidated by these method. The presence of the pulsed direct current that was passing through the SPS system was not taken into account, either.

Table 4 compares the sintering conditions and the properties of two polycrystalline spinels produced from Baikowski spinel powder, S30CR, one was sintered by HP and the other was sintered by SPS.

Table 4. Comparison of the sintering conditions and the properties of a hot pressed spinel and a spark plasma sintered processed spinel.

Firing conditions	Hot press <sup>11</sup>	SPS <sup>28</sup>
Max. temperature, °C	1550	1300
Heating rates, °C/min	N/A	100°C/min to 800°C, 10 °C/min to 1100°C, and 1 °C/min to 1300°C
Pressure, MPa	50	72
Soaking time	3 hours at 1550°C	10 minutes at 1000°C when cooling
Die material	graphite	graphite
Sintering aids	LiF, 1%	none
Transmittance	80% at 300nm, (2.54 mm thick)	74% at 550nm, (1.8 mm thick)

This work used a SPS machine as the tool to produce dense spinel samples without promoting the grain size to the micrometers range. The fact that SPS-processed spinel could not reach the theoretical transmittance in the visible region due to the existence of nano-size pores at the grain boundary triple points as described by Morita et.al.<sup>22</sup> and Bonnefont et.al.<sup>28</sup> was challenging. Since the densification of pure spinel is difficult, and a short-time sintering process might close the pores early and leave them unfilled, different loading schedules will be applied to investigate the effect of the heating rates and soaking times on the properties of the final products so as to determine the optimal SPS condition for spinel.

Undoped and doped samples undergone fast SPS cycles was also reheated in a HIP to study the effects of HIP post SPS on the properties of the samples.

## **2. Experiment design**

The goal of this research, as stated in the introduction, was to develop a better understanding of the densification of transparent polycrystalline spinel during spark plasma sintering. In order to achieve this goal, a number of objectives was achieved. At first, a high purity but easy-to-be-sintered spinel powder was selected and characterized to ensure that no second phase would be present in the sintered product. Secondly, the SPS conditions was determined and optimized to consolidate the spinel powder to its theoretical density without excessive grain growth and discoloration. Thirdly, the hardness of spinel was improved by engineering the grain boundary of spinel using alumina ( $\text{Al}_2\text{O}_3$ ) as the dopant. The addition of alumina in this case was based on the difference in the hardness between the stoichiometric spinel and the non-stoichiometric spinel. Alumina was coated on spinel particles via a surface precipitation process, and the dopant amount was determined based on the changes in hardness and transmittance as the amount of the dopant is increased. Appropriate characterization techniques were used to analyze and validate the optimal SPS condition and determine the sufficient dopant amount.

### **2.1. Selection of the starting powder and other chemicals**

#### **2.1.1. Spinel powder**

Based on the availability of high purity spinel powders in the market, the S30CR spinel powder produced by Baikowski International Corporation was chosen as the starting powder for the experiment. This powder was especially developed for transparent spinel, combining high chemical/phase purity and fine agglomeration to enable full transparency and high resistance. It has been popularly used in research and production of transparent

spinel.<sup>11, 19, 28, 181</sup> This commercial spinel powder is, however, not very consistent in terms of the physical properties and sinterability that caused a difference in the transmittance of the dense product after SPS processing.<sup>28</sup>

To begin with, powders from two different lots, 2JM-1611-1 and 2JM-3409-1, were examined. These powder comprised more than 99.9 wt% being the spinel phase. Their main impurities and the physical properties are listed in Table 5. The former had a tapped density of 0.28 g/cm<sup>3</sup>, while the later had a higher tapped density, > 0.5 g/cm<sup>3</sup>. It was not practical to use the powder of lot 2JM-1611-1 because it required a die which was more than ten times higher than the thickness of the expected dense sample. Therefore, powder of lot 2JM-3409-1 was used as the starting powder in this work.

Table 5. Physical properties and chemical analysis of the main impurities in Baikowski spinel powders.\*

Lot number	2JM-3409-1	2JM-1611-1
Chemical analysis, wt.%		
Na <sub>2</sub> O	0.0018	0.0014
SiO <sub>2</sub>	0.0047	0.0044
Fe <sub>2</sub> O <sub>3</sub>	0.0016	0.0002
CaO	0.0005	0.0013
K <sub>2</sub> O	0.0036	0.0024
Physical properties		
Surface area (BET method), m <sup>2</sup> /g	27.30	23.94
Median particle size diameter, μm	0.409	0.664
Tapped density, g/cm <sup>3</sup>	> 0.5	0.28

\* Data provided by the manufacturer. The impurities were determined by inductively coupled plasma spectrometry (Thermo Fisher Model 6300)

The crystalline phase of the as-received powder was examined by X-ray diffraction. The XRD pattern was obtained using a PANalytical X'Pert diffractometers. The lattice parameter,  $a$ , and the crystallite size,  $\tau$ , were analyzed using the Jade 9.0 software.

The degree of agglomeration in the spinel powder is crucial for a homogeneous doping of the aluminum oxide. In order to semi-quantitatively estimate the degree of agglomeration, the dependence of the particle size distribution on the ultrasonic agitation time was measured. A Malvern Mastersizer 2000 series Hydro 2000S particle size analyzer was used for this purpose. One gram of the spinel powder was dispersed into 50 ml of deionized water and ultrasonic agitation was applied before the suspension was added into the sample cell of the instrument. The ultrasonic agitation time was increased by a 30 second step and similar measurements were carried out.

The microstructure of the agglomerates was studied using the FESEM imaging technique. An amount of 0.01 grams of spinel powder was immersed into 20 ml of methanol, ultrasonicated for 10 minutes before one drop of the suspension was placed on a clean aluminum SEM stud. The stud was then put into a vacuum dryer to dry out the methanol solvent. Images of the spinel particles were taken using a Zeiss Sigma Field Emission SEM with Oxford INCA PentaFETx3 EDS system (Model 8100).

The weight lost and heat lost on heating of the as received powder was measured using a SDT Q600 V20.9 Build 20 DSC/DTA instrument. Samples were heated up from room temperature to 1100°C at a rate of 10°C/min in a nitrogen atmosphere. The change in mass and heat of the sample was plotted against the temperature on the same graph. Information of the weight lost at firing of the material was important because the processing time in the SPS might be very fast, if the volatiles in the powder was not

removed completely before sintering, they would become a gas phase at high temperatures and impede the sintering process once pores are partially closed.

### 2.1.2. Other chemicals

Aluminum nitrate (> 99wt%, Acros Organics) was used as the precursor for the aluminum oxide coated on the spinel particles. An analysis-grade ammonium hydroxide (25wt%, Acros Organics) was used for precipitating and pH adjusting purposes. All chemicals were commercially available and were used without further purification. Table 6 presents all chemicals used in the syntheses.

Table 6. Chemicals used in the syntheses.

Chemical	Formula	Purity	Supplier
Magnesium aluminate	$MgAl_2O_4$	>99.9 wt%	Baikowski
Aluminum nitrate nonanhydrate	$Al(NO_3)_3 \cdot 9H_2O$	>99%	Acros Organics
Ammonium hydroxide	$NH_4OH$	Analysis, 25wt%	Acros Organics

## 2.2. Optimization of the SPS conditions to produce transparent spinel

It has been well-known that the SPS is capable of heating up a sample at a very high heating rate (up to 1000°C/min).<sup>167</sup> This feature can be utilized to shorten the processing time, thereby restrain the grain growth of spinel during sintering. However, a high heating rate might not be applicable for the whole SPS cycle, because matter transport during sintering is often the rate limiting step. As discussed in section 1.6.1, the shrinkage of a compact is proportional to the two fifths power of time, the high heating rate is more likely applicable before sintering starts. The parameters of concerned in this study was the

heating rate and the soaking time, and their influences on the microstructure and optical properties of the sintered bodies.



Figure 13. Thermal Technology's spark plasma sintering system.

The spinel powder was sintered using a Thermal Technology's SPS system Model 10-4. The system was equipped with a 4000 amp power supply and tons 10 of force. A graphite die having a 20 mm inner diameter and a 50 mm outer diameter was used with 4 grams of the powder. The inner wall of the die was lined with a 0.13 mm-thick graphite foil to prevent reaction with the powder. The outer wall of the die was wrapped with a 7 mm-thick graphite felt to restrain any heat losses from the surface. The consolidation was made under vacuum. The powder was pre-pressed with a uniaxial pressure of 5 MPa. The pressure was increased at a constant rate from the beginning of the SPS process until it reached 80 MPa. At that point, the temperature of the process reached 750°C. After that,

the pressure was kept at 80 MPa, and was released when the cooling stage started. The powder was heated to the desired temperatures at several heating rates, and was held at these temperatures for different periods of time to examine the effects of the heating rate and the soaking time on the properties of the final product. The cooling rate of the process was 200°C/min. During SPS processing, the temperature was measured using a thermocouple with the measuring junction placed inside the lower punch of the die. The junction of the thermocouple was about 3 mm far away from the powder to be sintered. The SPS chamber was kept under vacuum during firing.

The parameters that were adjusted for a SPS run included the heating rate, the sintering temperature and the soaking time. The SPS conditions were optimized by investigating the effects of these parameters on the light transmittance and the density of the sintered bodies. The microstructural properties of the sintered bodies were also studied in order to explain the observed phenomena.

An initial run was set up such that the die was heated up at the rate of 100°C/min to 1400°C. The uniaxial pressure applied on the powder compact was increased at the rate of 10 MPa/min, and reached 80 MPa at 750°C. The die was held at 1400°C and under the pressure of 80MPa for 10 seconds before being cooled down at the rate of 200°C/min. Because of the high heating rate, this sample was expected to be porous and possibly discolored as had been observed.<sup>19, 22, 63</sup> In order to find the critical temperature where beyond that point high heating rates were disadvantageous to the optical performance of the sinter bodies, the heating rate at the high temperatures range was reduced to 2.5°C/min. Three transition points were considered, 1300°C, 1200°C, and 1100°C, as presented in Figure 14.

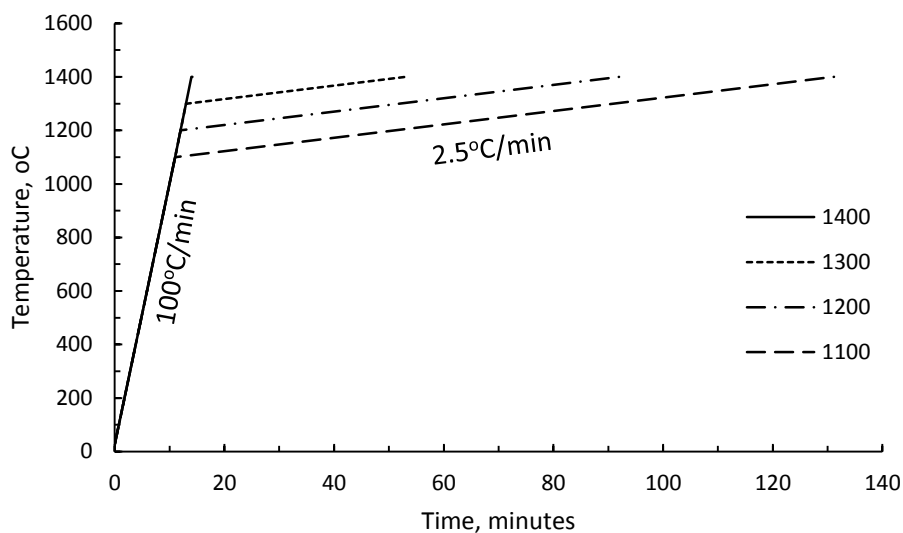


Figure 14. Temperature profiles settings of the initial SPS runs

The highest sintering temperature was estimated by observing the real time change in thickness of the powder compact during SPS processing. It was possible to measure this change because the Specview software accompanied with the SPS system was capable of recording the displacement of the electrode. The thermal expansions of the punches and spacers were eliminated by subtracting the displacement of the electrode when the die was run with the spinel powder to that when run without the powder. Two sets of samples were run for this measurement, one was run at the heating rate of 100°C/min and the other was run at the heating rate of 10°C/min to 1400°C with a 10 minute hold at 1400°C before cooling down. The empty die was also run using these settings.

From the above experiments, two critical points were obtained: one was the temperature where beyond that point, the heating rate should be lowered, and the other was the temperature at which the sintering process was completed. The effects of the heating rate between these critical points on the properties of the sintered bodies were studied. Four

heating rates were taken into consideration: 10°C/min, 5°C/min, 2.5°C/min and 1.25°C/min. This work also studied the influences of the soaking time on the properties of the sintered bodies. Three soaking times were considered: 10 minutes, 60 minutes, and 120 minutes. The optimal SPS condition was the run that produced the sample with the highest density, transmittance, and hardness but shortest processing time.

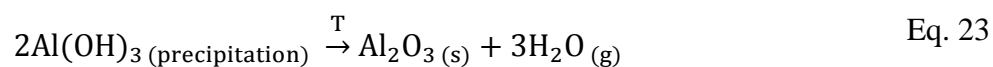
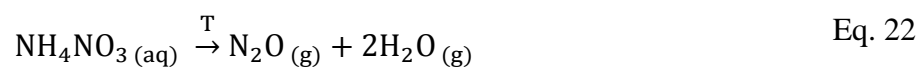
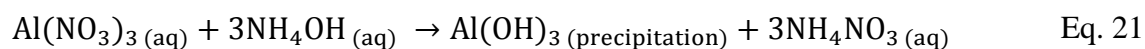
For comparison, the SPS condition developed by Bonnefont et.al.<sup>28</sup> was run using the selected starting powder. Their SPS cycle was chosen because it was able to produce polycrystalline spinel with the highest transmittance to date.

### **2.3. The process of coating alumina onto spinel particles by surface precipitation**

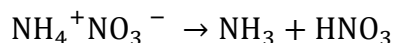
Distributing the alumina dopant homogeneously among spinel particles is challenging in this work. Mechanical mixing of a spinel powder with a small amount of alumina powder might result in a mixture with clusters of the alumina aggregates among spinel particles. Although alumina can diffuse into the spinel crystals at elevated temperatures to result in a non-stoichiometric spinel, this reaction might not complete after a short-time SPS processing, and alumina would stay as a separate phase in the sintered bodies. Therefore, an alternative way should be employed for doping such that alumina can later diffuse completely into the spinel structure.

The method that was chosen was to coat aluminum hydroxide precipitate onto spinel particles with using a colloidal process. A subsequent heat treatment was applied to dehydrate the precipitate to form aluminum oxide in the solid state. The experiment was set up such that the spinel powder was immersed into a solution of aluminum nitrate and de-ionized water to form a slurry with 25wt% solid loading. The slurry was then agitated

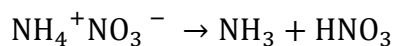
by ultrasonication in five minutes to break down soft agglomerates. Ammonium hydroxide was added drop-wise to the constantly stirred slurry until a pH > 8.5 was reached to ensure a complete precipitation. After an hour stirring for equilibration, the slurry was heated up to 500°C and held at this temperature for an hour to completely evaporate the exceeded NH<sub>4</sub>OH and decompose nitrate substances. The resultant material was crushed and ground using an agate mortar and pestle. The powder was finally calcined at 1200°C for an hour to completely dehydrate Al(OH)<sub>3</sub> leaving a nominally thin layer of Al<sub>2</sub>O<sub>3</sub> on the spinel particles. An undoped powder was also heat treated at 1200°C for an hour, and was labeled as S0A. The heating rate and the cooling rate was controlled at 15°C/minute. Doping at four levels, 1wt%, 3wt%, 5wt%, and 10wt% was prepared using the described method. These samples were labeled as S1A, S3A, S5A, and S10A, respectively. The chemical process can be summarized using the following equations:

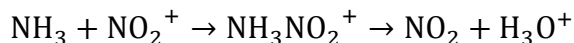
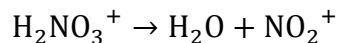


Eq. 22 presents the net result of a series of reaction.<sup>182</sup> The first step was the endothermic dissociation of ammonium nitrate to ammonia and nitric acid.

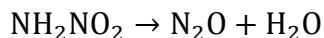
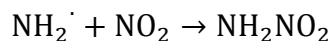
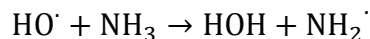
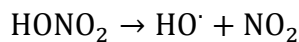


Below 290°C, the subsequent reaction was ionic with formation of NO<sub>2</sub><sup>+</sup>:





Above 290°C, the decomposition was taken over by the homolytic mechanism:



As could be seen on the binary phase diagram of the MgO-Al<sub>2</sub>O<sub>3</sub> system,<sup>4</sup> above 1000°C, Al<sub>2</sub>O<sub>3</sub> can diffuse into spinel to form an alumina-rich solid solution:



where n is a positive number, and  $1 \leq n \leq 11.5$  depending on the processing temperature.

To study the effects of the carbon contaminant, which might diffuse from the graphite die into spinel at firing,<sup>26</sup> a layer of 0.75 grams of alumina powder was placed between the punch and the spinel powder (Figure 15). After SPS processing, the alumina layers were removed using a surface grinder. Alumina was chosen because it is one of the constituents of spinel. Therefore, the inter-diffusion of alumina and spinel, if happens, would result in a spinel solid solution instead of color centers in spinel.

In additions, as demonstrated by Sonder and Weeks,<sup>107</sup> under moderate dc electric fields at temperatures near 1200°C, alumina maintained its insulating properties over time

while the insulating properties of spinel degraded rapidly, and magnesium cations could leave their places in the lattice and become ionic current carriers. The protective alumina layer in this case would act as a current barrier that slows down the degradation of spinel.

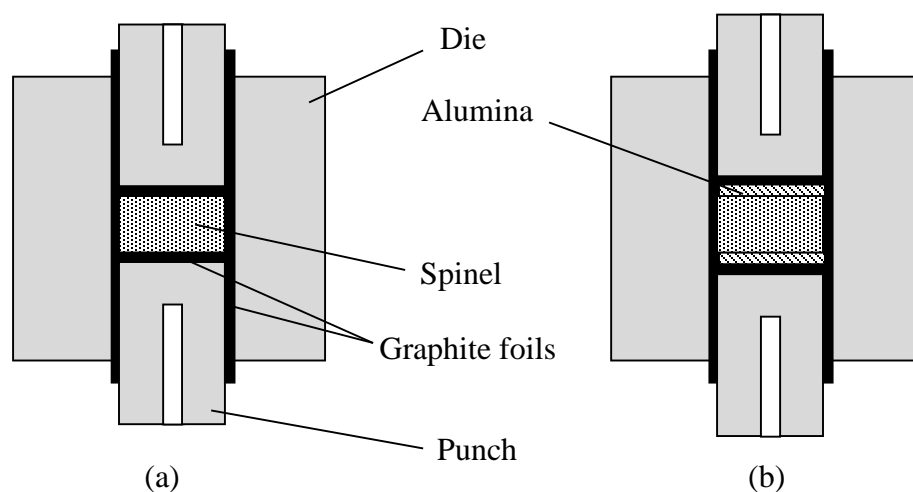


Figure 15. Illustration of the loading in the die. (a) without the alumina protective layers; (b) with the alumina protective layers

#### 2.4. Determine the effects of HIP post SPS on the properties of spinel

Selected samples were sent to Armorline Corporation for HIP processing. The samples were HIP at 1750°C under a pressure of 30ksi (207 MPa) for 12 hours. This was to see if HIP cures or exacerbates discoloration of SPS processed spinel.

#### 2.5. Sample preparation

##### 2.5.1. Cleaning, grinding and polishing

The surface of the samples after SPS was cleaned in a sandblaster. The graphite foils attached to the surface of samples were removed by a blast of compressed air carrying sand blown toward the surface of the samples. The samples were then surface ground with

a 325 grit resin bonded diamond wheel (North Jersey Diamond Wheel, Cedar Grove, NJ) on a Unison surface grinder, Model 306-0000 (Unison Corporation, Ferndale, MI).



Figure 16. Buehler mounting press and polisher. (a) SimpliMet® 1000 Automatic Mounting Press; (b) EcoMet 250 Grinder-Polishers with AutoMet 250 Power Heads (picture courtesy Buehler, An ITW Company)

After grinding, the sample was mounted on an epoxy block. For whole sample polishing, the epoxy was made from two parts of the Buehler SamplKwick resin and one part of the Buehler SamplKwick hardener (Buehler, An ITW company, Lake Bluff, IL). The sample was placed on the bottom of a plastic cup. The cup was then filled with the epoxy mixture. Upon curing, the sample mounted epoxy block was removed from the cup. For hardness testing, smaller pieces were cut from the main sample using a Leco VC50 slow speed saw (St. Joseph, MI). Pieces were then cleaned with acetone and mounted in the Buehler Epomet F epoxy using a Simplimet 1000 mounting press (Figure 16(a)).

The sample-mounted epoxy blocks were loaded in a Buehler EcoMet 250 variable speed grinder/polisher (Figure 16(b)). Polishing was started with a Buehler 125 micron diamond embedded disc to remove the excess epoxy on the surface of the samples. A

Buehler 45 micron diamond embedded disc took place until the pullouts observed under a microscope were smaller than 45  $\mu\text{m}$ . The Buehler 15 micron diamond embedded disc was then used until the pullouts was smaller than 15  $\mu\text{m}$ . These discs were used with tap water as an extender. Fine polishing was then continued using Buehler 9, 6, 1 and 0.25 micron diamond slurries and MetaDi Fluid as an extender on micro-cloth covered discs. Final polishing was performed using a Buehler 0.06 micron silica colloidal on a micro-cloth covered disc for five minutes. A five pound load was applied on each sample during polishing.

### **2.5.2. Etching**

Chemical etching using a Fisher Scientific 85% phosphoric acid was performed in order to remove the grain boundary phase for examining the microstructural properties of the spinel samples in a FESEM. A pyrex glass beaker containing the acid was heated up on a Fisher Scientific Isotemp® hot plate. The temperature of the hot plate was set at 250°C. The samples were immersed into the hot acid for 90 second for lightly etching, or for 120 seconds for a better exposure of the grain boundary.

### **2.5.3. Sputter coating**

Since spinel is an electrically non-conductive material, the specimens tend to charge when scanned by the electron beam in the FESEM, causing scanning faults and other image artifacts.

Therefore, an Electron Microscopy Sciences EMS 150T ES Turbo-Pumped Sputter Coater/Carbon Coater (Figure 17) was used to apply a 2 nm thick layer of gold onto the spinel specimens before FESEM imaging.

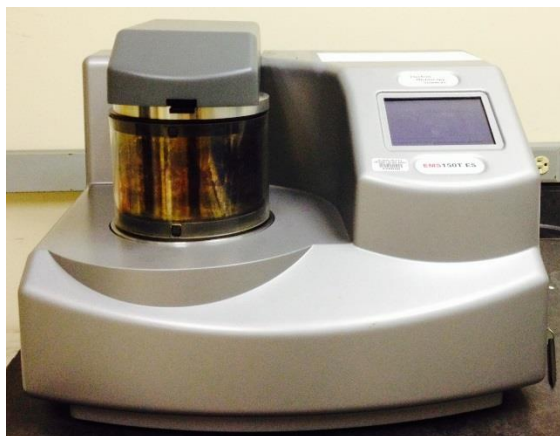


Figure 17. Electron Microscopy Sciences EMS 150T ES Turbo-Pumped Sputter Coater/Carbon Coater.

## **2.6. Characterization techniques**

### **2.6.1. Particle size analysis**

The particle size distribution of the powder was measured using a Malvern Mastersizer 2000 (Malvern Instruments Ltd., Worcestershire, UK). The machine uses a laser diffraction technique to measure the size of the particles.<sup>183</sup> It does this by measuring the intensity of light scattered as a laser beam passes through a dispersed particulate sample. This data is then analyzed to calculate the size of the particles that creates the scattering pattern.

The instrument was designed so that the powder can be analyzed either in the dry form using the Scirocco dry powder feeder or in form of the powder dispersed in a solvent using the Hydro S dispersion cell (Figure 18). This work used the Hydro S dispersion cell to feed the powder into the instrument. The powder was dispersed into deionized water,

stirred well and then ultrasonicated before analysis. For most measurements, the ultrasonication time was 5 seconds. When analyzing the breakage of the powder agglomerates by ultrasonication, the ultrasonication time varied from 0 seconds to 10 minutes.



Figure 18. Malvern Mastersizer 2000 Light Scattering Particle Sizer with Scirocco Dry Powder Feeder (front left) and Hydro S Small Volume Wet Dispersion Cell (front right) accessories.

### **2.6.2. Differential scanning calorimetry (DSC) and thermogravimetric analysis (TGA)**

The differential scanning calorimetry (DSC) and the thermal gravimetric analysis (TGA) are thermoanalytical techniques used to investigate the thermal characteristics of a substance. The DSC is used to measure the heat energy consumed or emitted by the sample as the function of temperature, while the TGA is used to measure the weight loss or gain as a function of temperature. Using the DSC it is possible to obtain important quantities

such as fusion, crystallization, glass transition temperatures as well as the events of oxidation and other chemical reactions.

Simultaneous measurement of weight change (TGA) and true differential heat flow (DSC) of the as-received spinel powder were performed on the instrument SDT Q600 V20.9 Build 20 (TA Instruments, New Castle, DE). The sample was heated at the heating rate of 10°C/min in a nitrogen atmosphere to 1100°C. The DSC and TGA curves were plotted on the same graphs.

### 2.6.3. Density

Density of the samples was measured using the Archimedes displacement method, following the ASTM standard (B962-13).<sup>184</sup> The polished samples were carefully cleaned with acetone before measurement. Samples were then allowed to dry before weighing in air. The samples were boiled in distilled, deionized water containing a few drops of Photoflo (to prevent air bubbles) for an hour. After cooling to the room temperature, suspended weights were taken by weighing the samples while they were suspended in distilled, deionized water. A damp paper towel was then used to remove the water from the surface, and saturated weights were taken. Five weights were taken for each sample for dry, water saturated, and suspended measurements.

The density of the samples was computed using the following equation:

$$D = \frac{m_d \rho_w}{m_s - m_w} \quad \text{Eq. 25}$$

where  $m_d$  is the mass of the dry sintered sample in air,  $m_w$  is the mass of the water-saturated sample in air,  $m_s$  is the mass of the water-saturated sample suspended in water, and  $\rho_w$  is the density of water.

#### 2.6.4. Spectrophotometry

Spectrophotometry is the quantitative measurement of the transmittance, absorbance or reflectance of a material as a function of wavelength. This technique involves the use of a spectrophotometer that by-passes a beam of radiated energy through a sample and measures the intensity of the radiated energy reaching a detector.



Figure 19. Thermo Scientific Evolution 300 UV-Vis spectrophotometer (picture courtesy Thermo Scientific).

A Thermo Scientific Evolution 300 UV-Vis spectrophotometer (Thermo Fisher Scientific Inc., Waltham, MA) was used to measure the transmittance of the sintered spinel samples in a wavelength range from 250nm to 1100nm (Figure 19). The transmittance of the samples were normalized to the transmittance at a thickness of 1.8 mm using the following equation:<sup>28</sup>

$$T_{d_2} = (1 - R_s) \left( \frac{T_{d_1}}{1 - R_s} \right)^{d_2/d_1} \quad \text{Eq. 26}$$

where  $R_s$  is the total normal surface reflectance ( $\approx 0.14$ ),  $T_{d_1}$  and  $T_{d_2}$  is the in-line transmittance of a sample at the thickness  $d_1$  and  $d_2$ , respectively.

### 2.6.5. Fourier transform infrared spectroscopy

Fourier transform infrared spectroscopy (FTIR) is one of the instrumental methods used to study the interaction of the infrared light with matter. The technique uses a mathematical process named after Joseph Fourier to convert the signals from an interferometer into a spectrum.<sup>185</sup>

A Mattson FTIR Spectrophotometer Galaxy series 5000 (Mattson Instruments Inc., Madison, WI) was used to measure the transmittance of light through the sintered spinel samples in the mid-infrared region, from 2.5 to 6.5  $\mu\text{m}$  wavelength (Figure 20). The transmittance of the samples were normalized to the transmittance at a thickness of 1.8 mm using Eq. 26.

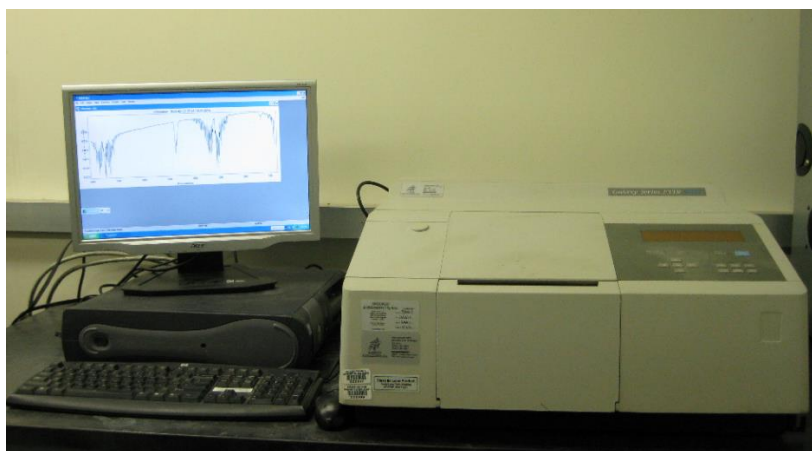


Figure 20. Mattson Instruments Galaxy series FTIR 5000 spectrophotometer

The instrument was also used to detect the existence of the impurities in the alumina-coated spinel powder. The powder samples used for this experiments was prepared by heating the  $\text{Al}(\text{OH})_3$  -coated powder to 400°C, 600°C, 800°C, and 1000°C with a ten minute hold at these temperatures. The heating rate and cooling rate were 20°C/min. The heat-treated powder was then mixed with potassium bromide (KBr) using a set of agate mortar and pestle, and pressed into a pellet. The weight percentage of spinel in KBr was 1%. The thickness of the pellet was approximately 1 mm.

#### 2.6.6. X-ray diffraction (XRD)

X-ray diffraction is the analytical method to determine the atomic and molecular structure of crystalline materials.



Figure 21. PANalytical X-ray Diffractometer.

This work used a PANalytical X-ray Diffractometer Model PW3040/60 to obtain the X-ray diffraction patterns of the spinel materials, including the as-received powder and the dense samples (Figure 21).

Powder samples was prepared by filling a necessary amount of powder into the standard sample holder. The sintered samples were mounted in a dense sample holder using sticky tack. All sintered samples were polished before X-ray diffraction to obtain a smooth surface finish. Care was taken to keep the surfaces of the sample clean, flat and parallel with the holder to prevent avoidable displacement errors.

The generation of X-rays was controlled at a working level of 45KV/40mA. The sample holders were spun while measuring the diffraction.

The data collected from the diffractometer were analyzed using the Jade software developed by Materials Data Inc.. This is a state-of-the-art computer program that allows to clean up the raw data, identify phase, solve the crystal structure, and do quantitative analysis.

The degree of agglomeration,  $N$ , of the powder is the average number of grains in a particle, and can be estimated using the equation:<sup>186</sup>

$$N = \frac{d_{\text{BET}}^3}{d_{\text{XRD}}^3} \quad \text{Eq. 27}$$

where  $d_{\text{BET}}$  is the average particle size from surface area, and  $d_{\text{XRD}}$  is the average crystallite size from XRD peak broadening.

### 2.6.7. Scanning electron microscopy and energy dispersive spectroscopy (SEM/EDS)

A scanning electron microscope (SEM) is a type of electron microscope that produces the image of a sample by scanning a focused electron beam over a very small spot on the sample and detecting the current leaving the object.

This work used a Zeiss Sigma Field Emission SEM with Oxford INCA PentaFETx3 EDS system (Model 8100) to image the microstructure of the spinel powder and the dense spinel samples (Figure 22). Pictures of the samples was taken under an acceleration voltage of 2kV with a 30  $\mu\text{m}$  aperture.

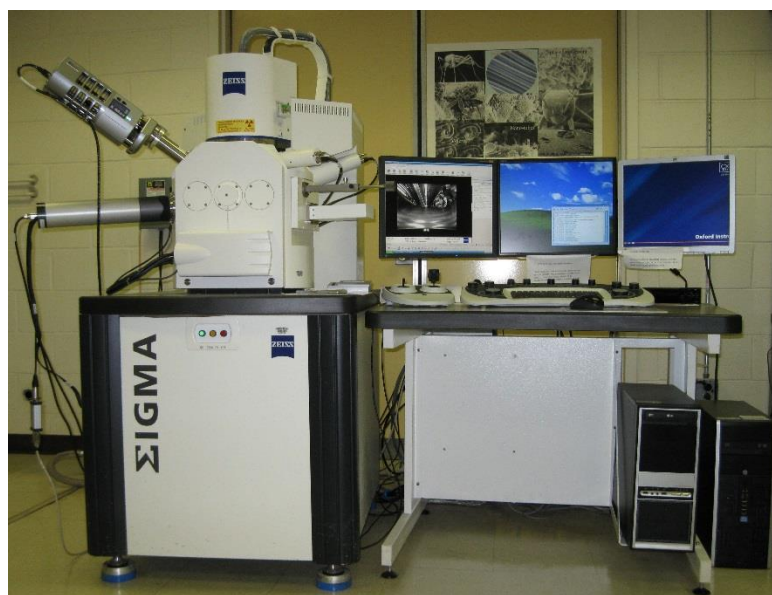


Figure 22. Zeiss  $\Sigma$ igma field emission scanning electron microscope

The grain sizes of the sintered samples was measured using the linear intercepts method. The Lince 2.4.2e software (TU Darmstadt, FB Materialwissenschaft, FG NAW) was used with a conversion factor of 1.56.<sup>187</sup>

### **2.6.8. Transmission electron microscopy (TEM)**

A transmission electron microscope (TEM) is a type of electron microscope that produces the image of an ultra-thin specimen by transmitting an electron beam through the specimen. An image is formed from the interaction of the electrons transmitted through the specimen. The image is magnified and focused onto an imaging device, or to be detected by a sensor.

A number of different TEM machines were used throughout this work because of varying equipment and resolution problems. A Topcon 002B TEM was used for the spinel powder, and a Phillips CM300 TEM working under 300 kV was used for the sintered samples.

### **2.6.9. Micro-indentation hardness**

“Hardness is a measure of the resistance to permanent deformation or damage”.<sup>87</sup> There are six types of hardness testing methods: 1) Statistic indentation test, 2) Dynamic indentation test, 3) Scratch test, 4) Rebound test, 5) Pendulum recoil test, and 6) Abrasion test. This work used the statistic indentation testing method with a Vickers diamond indenter and a Knoop diamond indenter.

A Leco M-400-G3 (LECO Corporation, Michigan) hardness tester was used with a PAXcam digital microscope camera and a Confident Hardness Testing Program to measure the hardness of the spinel samples. The calibration was performed using a LECO test block and an Olympus objective micrometer prior to the start of the testing series to verify the accuracy of the measurement. The measurement strictly followed the testing standard developed by the American Society for Testing Materials.<sup>188, 189</sup> Hardness indents were

made at the loads of 0.100 kg, 0.300 kg, 0.500 kg, 1 kg, and 2 kg with a 15 second hold. Ten indents were taken at each load at a well-polished region.

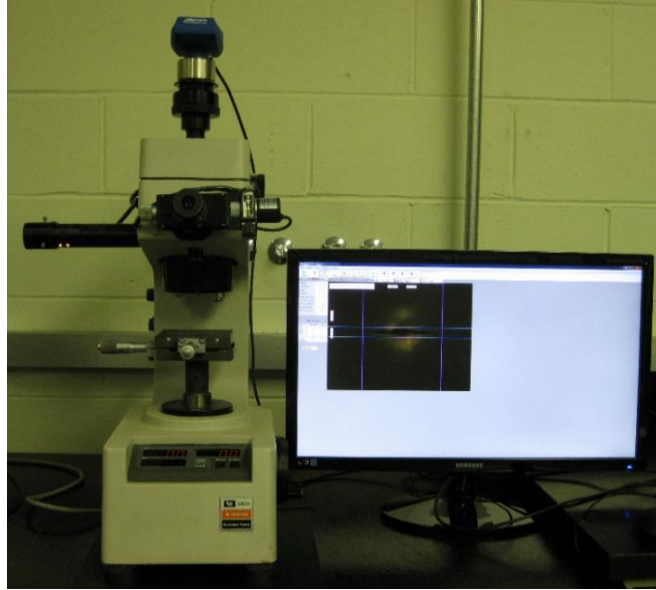


Figure 23. Leco M-400-G3 micro-indentation hardness tester.

The Knoop hardness reported with units of GPa was computed as follows:

$$HK = 1.000 \times 10^{-3} \times P / (C_p d^2) \quad \text{Eq. 28}$$

where P is the force applied on the indenter, measured in Newtons,  $C_p$  is the correction factor related to the indenter shape, which ideally should be 0.07028, d is the length of the long diagonal of the indentation, measured in mm.

The dimensionless Knoop hardness number was computed by:

$$HK = P / (C_p d^2) \quad \text{Eq. 29}$$

where  $P$  is the force applied on the indenter, measured in kgf,  $C_p$  and  $d$  is the same as in Eq. 28

The Vickers hardness reported with units of GPa was computed by:

$$HK = 0.0018544 \times P/d^2 \quad \text{Eq. 30}$$

where  $P$  is the force applied on the indenter, measured in Newtons, and  $d$  is the mean diagonal length of the indentations, measured in mm.

The dimensionless Vickers hardness number was computed as follows:

$$HV = 1854.4 \times P/d^2 \quad \text{Eq. 31}$$

where  $P$  is the force applied on the indenter, measured in gf, and  $d$  is mean diagonal length of the indentation, measured in  $\mu\text{m}$ .

#### **2.6.10. Laser Raman spectroscopy**

Raman spectroscopy is a spectroscopic technique used to observe vibrational, rotational, and other low-frequency modes in a system. This work used a Renishaw InVia Confocal micro-Raman Spectrometer to study the vibrational mode of the doped and undoped spinel samples (Figure 24). Raman spectra of the samples were taken with a 514 nm laser excitation line.



Figure 24. Renishaw InVia Confocal Micro-Raman Spectrometer (image courtesy Renishaw PLC).

### 2.6.11. Acoustic evaluation of the elastic properties

The small size of the samples prepared from the current SPS set-up made mechanical strength tests difficult at this time. Therefore, A-scan (point scan) ultrasound nondestructive testing was chosen as the method for characterizing the elastic properties of the material. The equipment for this test was designed and built at Rutgers University (Figure 25).

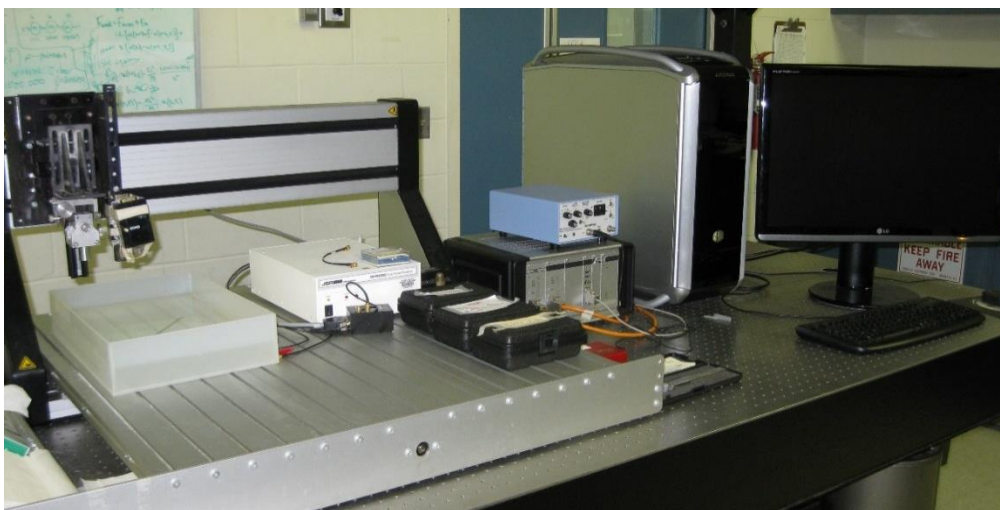


Figure 25. Single transducer ultrasound system for measuring the elastic properties of the dense samples.

Poisson ratio,  $\nu$ , is the ratio of transverse contraction strain to longitudinal extension strain in the direction of stretching force applied on a material, and can be directly calculated after measuring the longitudinal and shear velocities of the ultrasonic wave propagated through the material.<sup>190</sup>

$$\nu = \frac{\left(1 - 2\frac{C_s}{C_l}\right)^2}{\left(2 - 2\frac{C_s}{C_l}\right)^2} \quad \text{Eq. 32}$$

where  $C_s$  is the shear wave velocity (m/s), and  $C_l$  is the longitudinal wave velocity (m/s).

The measurement of ultrasonic velocities depends upon generating a dynamic pressure wave (pulse) into a material of known thickness and measuring the transit time of the emerging acoustic pressure wave. The longitudinal ( $C_l$ ) and shear ( $C_s$ ) wave velocities are determined by the follow equations:<sup>190</sup>

$$C_l = \frac{2d}{\text{TOF}_l} \quad \text{Eq. 33}$$

$$C_s = \frac{2d}{\text{TOF}_s} \quad \text{Eq. 34}$$

where  $d$  is the sample thickness, TOF is the time it takes for an acoustic wave to travel through the sample, and the subscripts,  $l$  and  $s$ , refer to either longitudinal or shear waves. The factor of 2 in each equation accounts for the ultrasonic wave travelling through the material twice due to using a pulse-echo configuration.

Young's modulus,  $E$ , is the ratio of applied stress to the resulting strain of a material and is calculated by using the equation:<sup>190</sup>

$$E = \frac{C_1^2 \rho (1 - 2\nu)(1 + \nu)}{(1 - \nu)} \quad \text{Eq. 35}$$

where  $\rho$  is the density ( $\text{g/cm}^3$ ) of the material to be measured.

Shear modulus,  $G$ , is the ratio of applied shear stress to the resulting shear strain and is calculated by using the equation:<sup>190</sup>

$$G = \frac{E}{2(1 + \nu)} \quad \text{Eq. 36}$$

Bulk modulus,  $K$ , is the resistance of a material to compression and is quantified using the equation:<sup>190</sup>

$$K = \frac{E}{3(1 - 2\nu)} \quad \text{Eq. 37}$$

### **3. Determination and optimization of the SPS condition for transparent spinel**

Although the capability of performing a high heating rate is the major advantage of the SPS over the HP and HIP methods, low SPS heating rates have been proved to be efficient in producing transparent spinel without excessive grain growth. In addition, the SPS temperature for transparent spinel could be kept at temperatures as low as from 1300°C to 1350°C. Morita et.al.<sup>22</sup> demonstrated that by controlling the SPS heating rate at as low as less than 10°C/min with a 20-minute hold at 1300°C, a fine-grain polycrystalline spinel with a transmittance of about 50% at the 550 nm wavelength could be obtained.

The present study was performed to further optimize the SPS condition for transparent spinel. Two factors were considered in this study, one is the heating rate at different stages of the SPS process and the other is the soaking time, so called dwell time.

### 3.1. Characterization of the starting powder

Figure 26 is the FESEM image which shows the agglomerates of the as-received spinel powder. Each agglomerate comprises a number of nano-scale primary particles, and the voids between these particles have different sizes. As can be seen on the top right of the image, several agglomerates bond together to form a larger size inter-agglomerate. The voids in this inter-agglomerate are also larger than the voids in the primary particles. These inter-agglomerate voids might shrink more slowly and be more difficult to fill up during sintering than the voids in a single agglomerate.<sup>191</sup> Therefore, these inter-agglomerates should be broken as much as possible for an easier sintering.

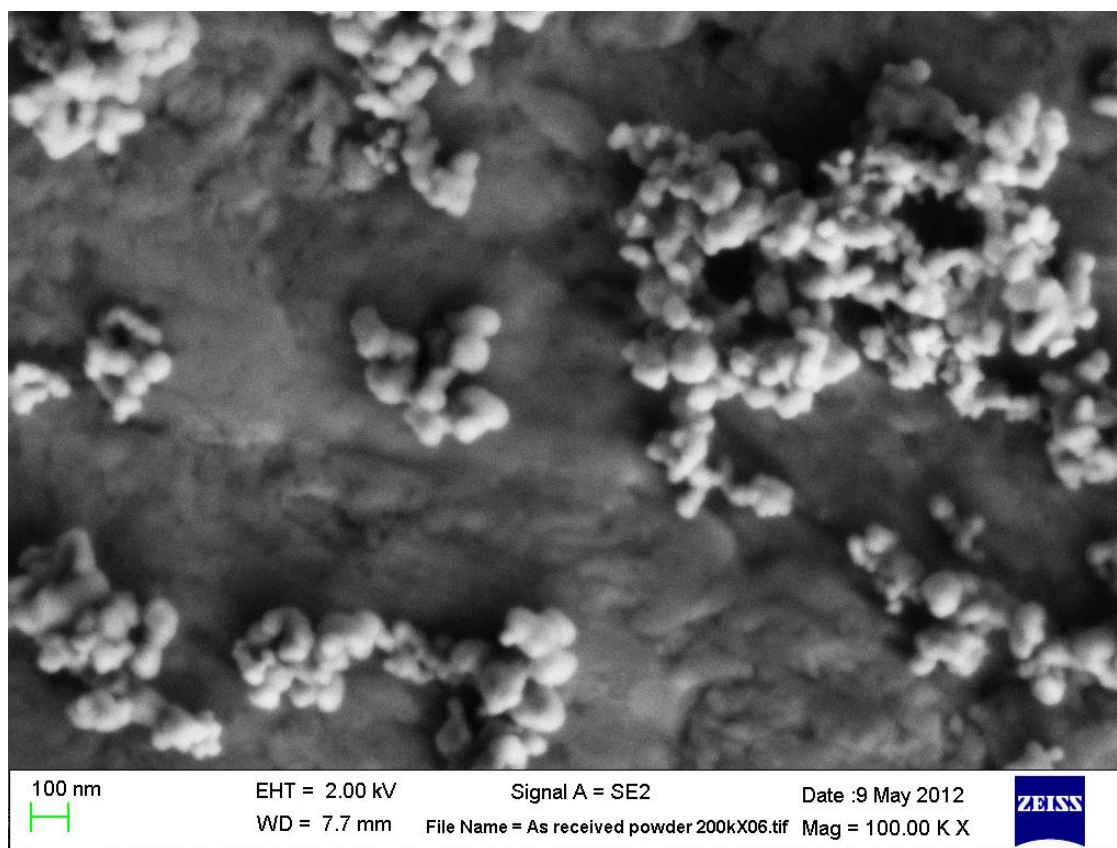


Figure 26. FESEM image showing the agglomerates of the as-received spinel powder.

Figure 27 is the X-ray diffraction pattern of the powder. The powder diffraction file (PDF) card number 97-009-7159 matched with the acquired data and indicated that there was only one phase, which was spinel, presented. The average lattice parameter calculated from peak locations and Miller indices (cubic) basing on the six lowest-angle peaks using the Jade program was 8.0878 Å. It was slightly shorter than that of a natural single crystalline spinel ( $a = 8.0898$  Å) measured by Finger *et.al.*<sup>68</sup>. The average crystalline size of the powder as estimated by the Jade software was 386 Å. The average number of grains in a particle was 57512 as calculated using equation Eq. 27.

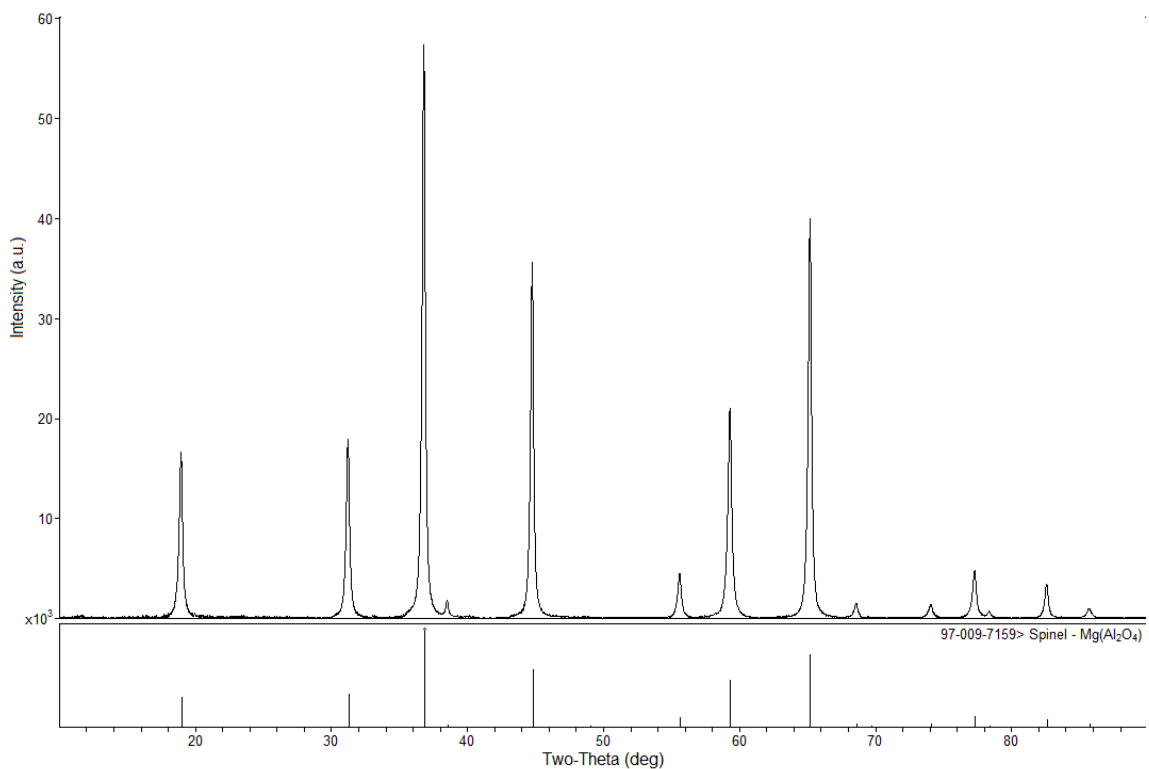
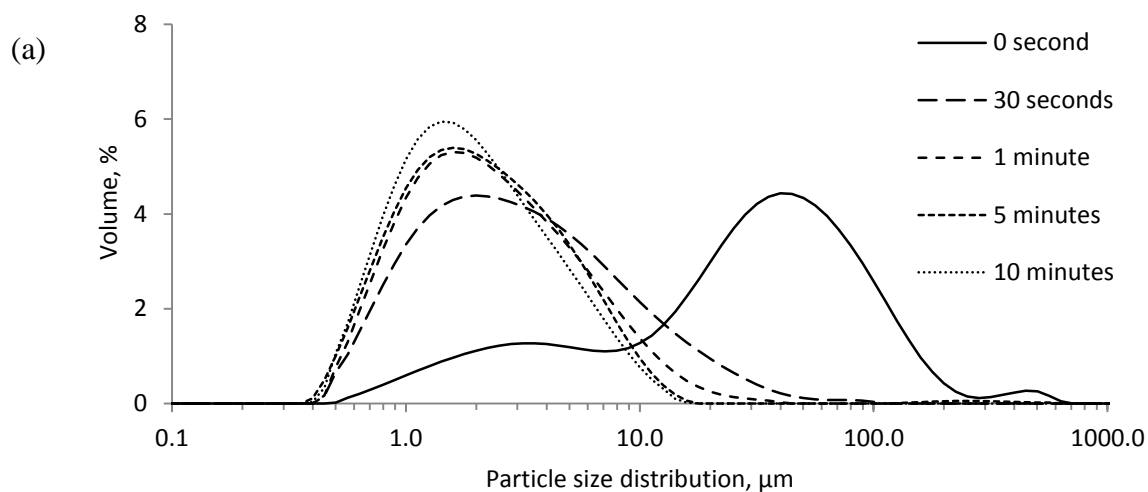


Figure 27. X-ray diffraction pattern of the as-received powder



Ultrasonication time minutes	D(v, 0.1) $\mu\text{m}$	D(v, 0.5) $\mu\text{m}$	D(v, 0.9) $\mu\text{m}$
0	$2.515 \pm 0.164$	$29.555 \pm 1.756$	$96.193 \pm 2.971$
0.5	$0.867 \pm 0.003$	$2.676 \pm 0.033$	$11.345 \pm 0.117$
1	$0.794 \pm 0.003$	$2.045 \pm 0.027$	$6.870 \pm 0.082$
5	$0.752 \pm 0.003$	$1.918 \pm 0.039$	$5.770 \pm 0.313$
10	$0.737 \pm 0.004$	$1.728 \pm 0.018$	$5.133 \pm 0.110$

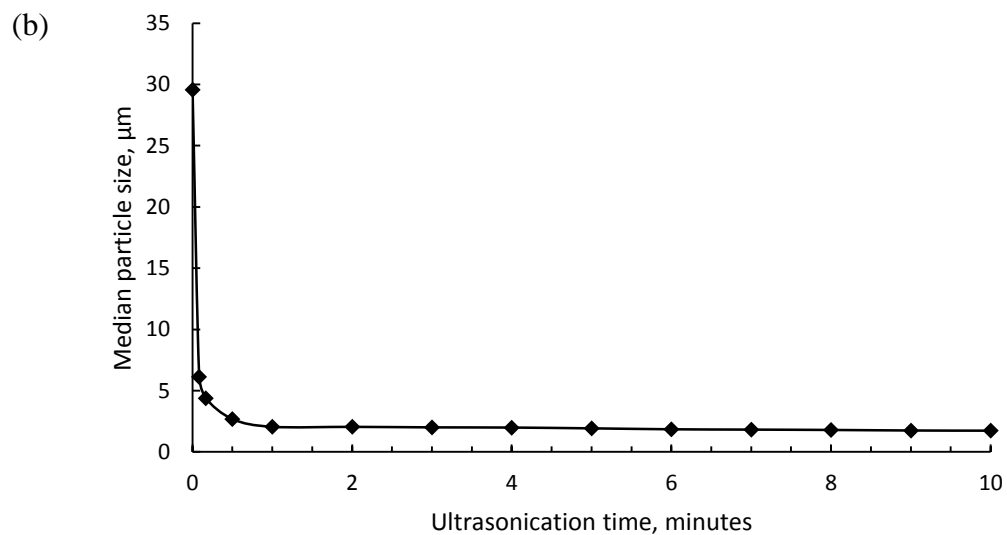


Figure 28. The dependence of the particle size distribution on the ultrasonication time. (a) Particle size distribution curve shifted to the smaller size site as the ultrasonication time increased; (b) Median particle size decreased as the ultrasonication time increased.

Figure 28(a) presents the change in particle size distribution of the as-received powder by ultrasonic agitation. Measurement was taken for a dilute suspension of the powder in deionized water. The median particle size,  $D(v, 0.5)$ , was reduced by four orders of magnitude after only 30 seconds of ultrasonic agitation. As the ultrasonic agitation time was further increased, although more agglomerates were broken and finer particles were formed, the reduction of the median particle size was kept at the same order of magnitude (Figure 28(b)). It means that the majority of the soft agglomerates of the powder were broken by ultrasonic agitation in less than a minute, and increasing of the ultrasonic agitation time was not very effective in terms of the degree of reduction in average particle size of the powder.

Figure 29 presents the DSC and TGA curves of the as-received powder. There was a continuous heat loss on the DSC curve and a continuous weight loss on the TGA curve. The total weight loss was 1.6 wt.%. Both curves were smooth with a change in the slope. The slope of the DSC curve increased at about 700°C, while the slope of the TGA curve decreased at about 500°C. Since this was a high-purity spinel powder and no phase transition was expected until the melting point of spinel at 2122°C,<sup>4</sup> the observed losses can be interpreted as the evolution of the water absorbed in to the powder during storage. The surface of the spinel particles had been partly hydrated, so that more heat was needed to break the chemical bonded water at temperature above 700°C. This phenomenon could be used to explain why heat treating of the spinel powder before SPS helped to enhance light transmission as observed by Kim et.al.<sup>24</sup> This observation suggested that a system of connected capillaries is needed at the early stage of the SPS process so that volatiles in

form of water is able to escape from the powder compact. Therefore, a full pressure should not be applied on to the sample before SPS to avoid early pore closure.

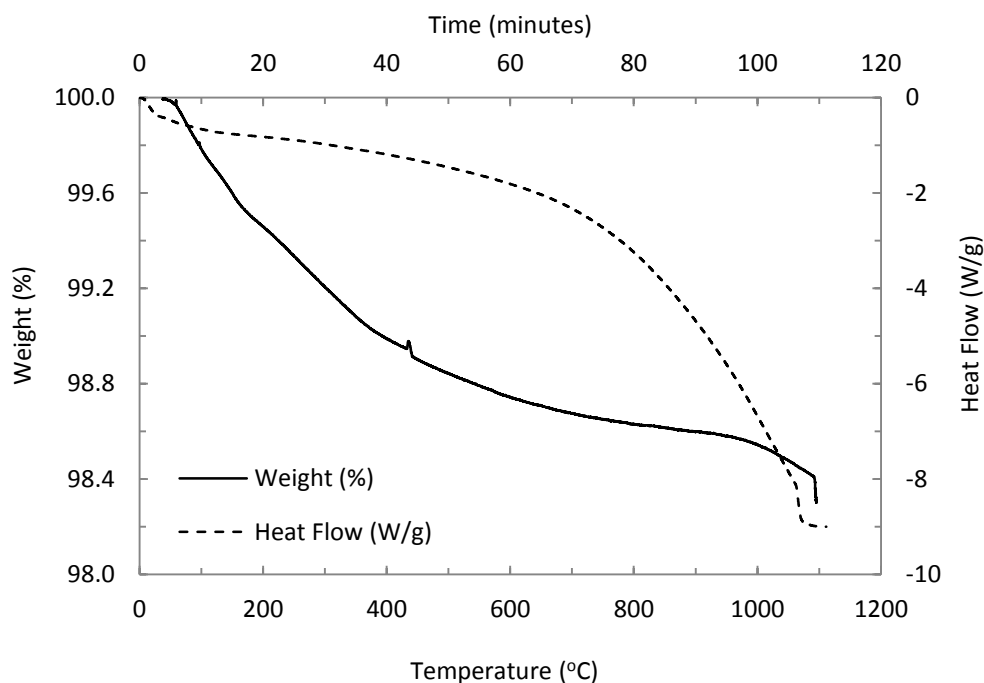


Figure 29. The DSC and TGA curves of the as-received powder. The sample was heated at the heating rate of  $10^{\circ}\text{C}/\text{min}$  in a nitrogen atmosphere.

### 3.2. Effects of high SPS heating rate on the properties of spinel

Initially, four samples were SPS at the following condition: The as-received powder was heated to  $1400^{\circ}\text{C}$ ,  $1300^{\circ}\text{C}$ ,  $1200^{\circ}\text{C}$  and  $1100^{\circ}\text{C}$  at the heating rate of  $100^{\circ}\text{C}/\text{min}$ , and continued to  $1400^{\circ}\text{C}$  at the heating rate of  $2.5^{\circ}\text{C}/\text{min}$ . They were held at  $1400^{\circ}\text{C}$  for 10 seconds before cooling down at the cooling rate of  $200^{\circ}\text{C}/\text{min}$ . These samples were labeled as T1400, T1300, T1200, and T1100, respectively. The numbers, 1400, 1300, 1200 and 1100, indicate the temperature where the heating rate was changed.

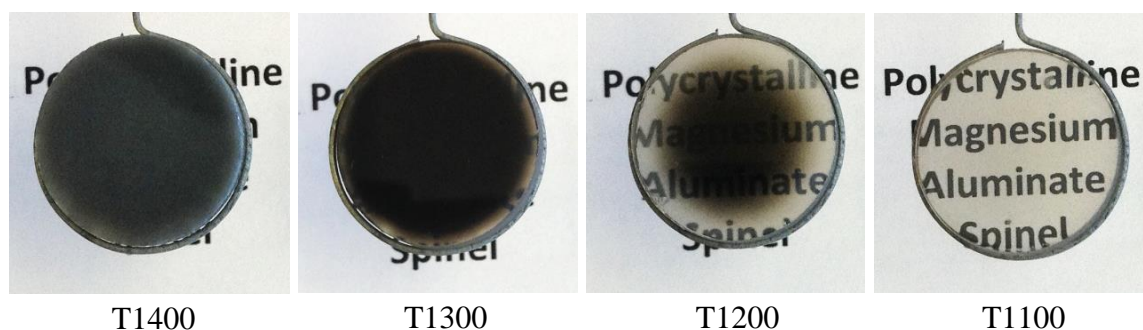


Figure 30. Photographs of samples SPS at the heating rate of 100°C/min to a transition point and then at 2.5°C/min to 1400°C, with a 10 seconds hold at 1400°C. The samples had a thickness of about 3 mm, and were placed at 4 cm above the text.

Figure 30 shows the photographs of these four samples after polishing. T1400 had a dark gray color, while T1300 had a black color with a thin translucent edge. As the transition point of the heating rate was lowered to 1200°C, the discoloration gradient was more visible. The sample became transparent as the transition point of the heating rate was lowered to 1100°C. The Archimedes densities of these samples were 3.554, 3.555, 3.568 and 3.579 g/cm<sup>3</sup>, respectively. Their relative densities obtained by taking the theoretical density of stoichiometric spinel<sup>39</sup> as 3.578 g/cm<sup>3</sup> were 99.32%, 99.37%, 99.73% and 100.03%.

The in-line transmittance through the center of these samples were plotted as a function of wavelength in Figure 31. Data were normalized to the transmittance at the thickness of 1.8 mm. The discontinued section on these spectra was due to the fact that the two spectrometers used for the measurement did not cover this range of wave lengths. Samples T1400 and T1300 did not transmit light in the visible region but became opaque in the mid infrared region. Their transmittance at the 550 nm wavelength was 0%, and at the 4μm wavelength was 34% and 19% respectively. The light transmittance was improved as the transition point of the heating rate was further lowered but the sample

became transparent only when the transition point was lowered to 1100°C. The properties of these samples were summarized in Table 7.

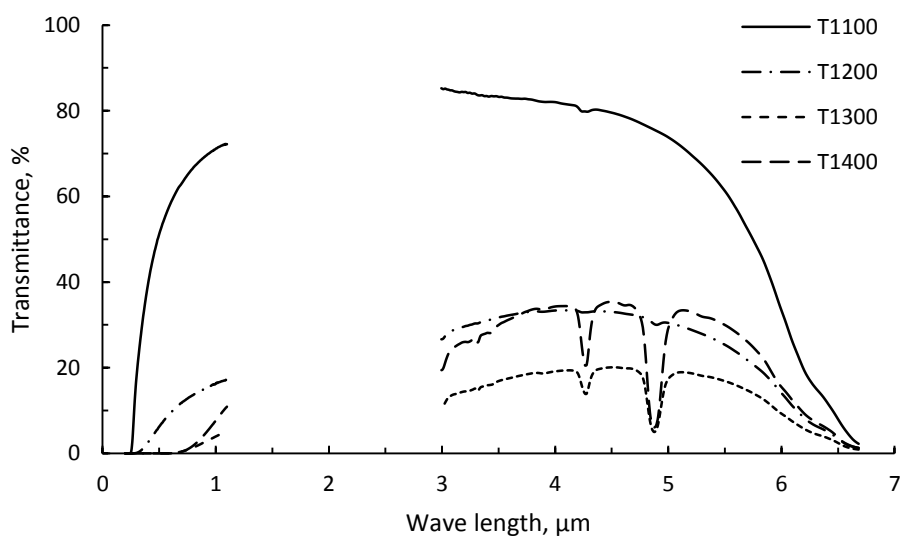


Figure 31. In-line transmittance of samples SPS at the heating rate of 100°C/min to a transition point and then at 2.5°C/min to 1400°C, with a 10 seconds hold at 1400°C. Data was normalized to the transmittance at the thickness of 1.8 mm.

Table 7. Properties of samples SPS at various heating rates.

Sample	SPS condition*	Density, g/cm <sup>3</sup>	Transmittance, %	
			at 550nm	at 4μm
T1400	100°C/min to 1400°C	3.554	0.0	34.3
T1300	100°C/min to 1300°C and then 2.5°C/min to 1400°C	3.555	0.0	19.2
T1200	100°C/min to 1200°C and then 2.5°C/min to 1400°C	3.568	8.1	33.4
T1100	100°C/min to 1100°C and then 2.5°C/min to	3.579	55.4	82.0

\* with a 10 second hold at 1400°C.

Figure 32 shows the difference in color of the outermost layer and the center of the sample SPS at the heating rate of 100°C/min to 1400°C with a 10 minutes hold at this temperature. While the outer had a black color, the center had a white color. A gradient of white-to-black color from the center to the edge of the sample was also observed. The apparent density calculated from the Archimedes' principle<sup>192</sup> was 3.55 g/cm<sup>3</sup>.

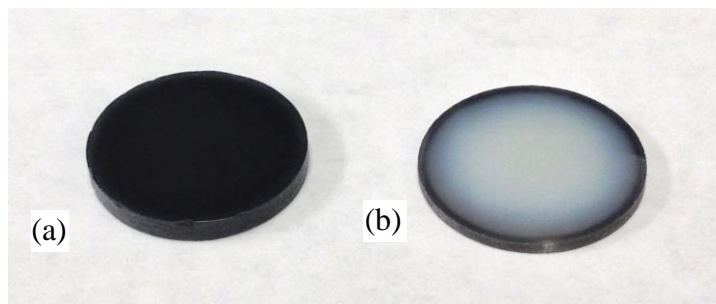


Figure 32. Photograph showing the difference in color of the surface and the center of the sample SPS at the heating rate of 100°C/min with a 10 minutes hold at 1400°C. (a) As-received SPS sample after polishing; (b) The cross-section through the center of the sample.

The microstructure of these surfaces was studied using FESEM imaging (Figure 33). The specimens were not coated, and the FESEM was run at an accelerating voltage of 2kV to avoid charging. The porosity of the sample was calculated from the size of the pores present on the surface of sample using the linear intercept method<sup>193</sup> with the Lince software. The center of the sample had a porosity of 1.96 vol.% while the top of the sample was almost dense with a few pores present. At the center of the sample, most of the pores were at the grain boundary triple point junctions. However, several in-grain pores were also observed. The number of pores decreased significantly at the top of the sample. Besides the difference in the porosity, the color contrast between grains at the top of the sample was more obvious than that at the center. It could be because of the difference in the Mg/Al cation ratio between the grains at these surfaces.

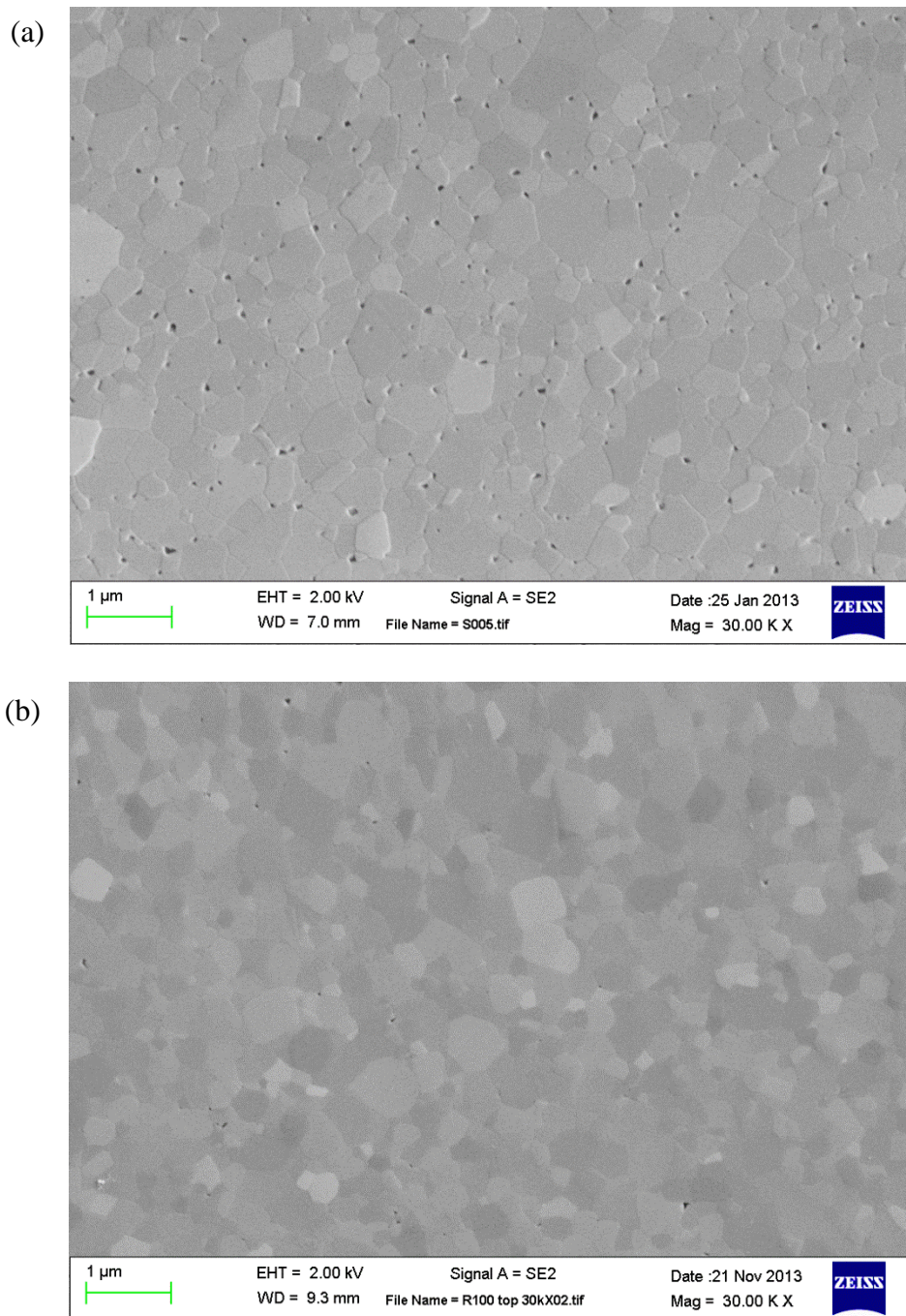


Figure 33. FESEM images of the sample heated at the rate of  $100^{\circ}\text{C}/\text{min}$ : (a) taken at the center of the sample; (b) taken at the top of the sample.

It was undoubtedly that densification started from the surface in contact with the graphite die. It was because graphite was thermally and electrically conductive. It was heated up by the Joule's heating effect as a current passing through, and released heat to the surrounding. Since heating was resistive, the difference between the temperature inside the sample and that on the surface in contact with the heated graphite die depended on the thermal conductivity of the material. The thermal conductivity of spinel is relatively low, 14.6 W/m.K at room temperature,<sup>1, 194</sup> while that of polycrystalline graphite is around 100 W/m.K,<sup>195-197</sup>. Therefore, the outermost layer of the sample was heated up faster than the center, and densification started from the outermost layer inward. That was why the edge of T1300 and T1200 was more transparent than the center, and the porosity at the center of the sample was higher than at the top.

The XRD patterns presented in Figure 34 were taken on the top and the center of the sample SPS at the heating rate of 100°C/min. The XRD pattern of the as-received powder was also included for comparison. Neither phase change nor new phase formation was observed, but a close look at each diffracted peak showed that there was a peak shift. The diffracted peaks of the top surface shifted more to the high-angle side than that of the cross section through the center of the sample. Regardless of the strain, the shifting of XRD peaks to the high-angles in spinel is normally due to the change in stoichiometry to the alumina rich composition.<sup>198</sup> Since peak shifting was consistent and FESEM imaging showed a change in the contrast between grains, this peak shift could be attributed to the change in the Mg and/or Al cations distribution on these surfaces.

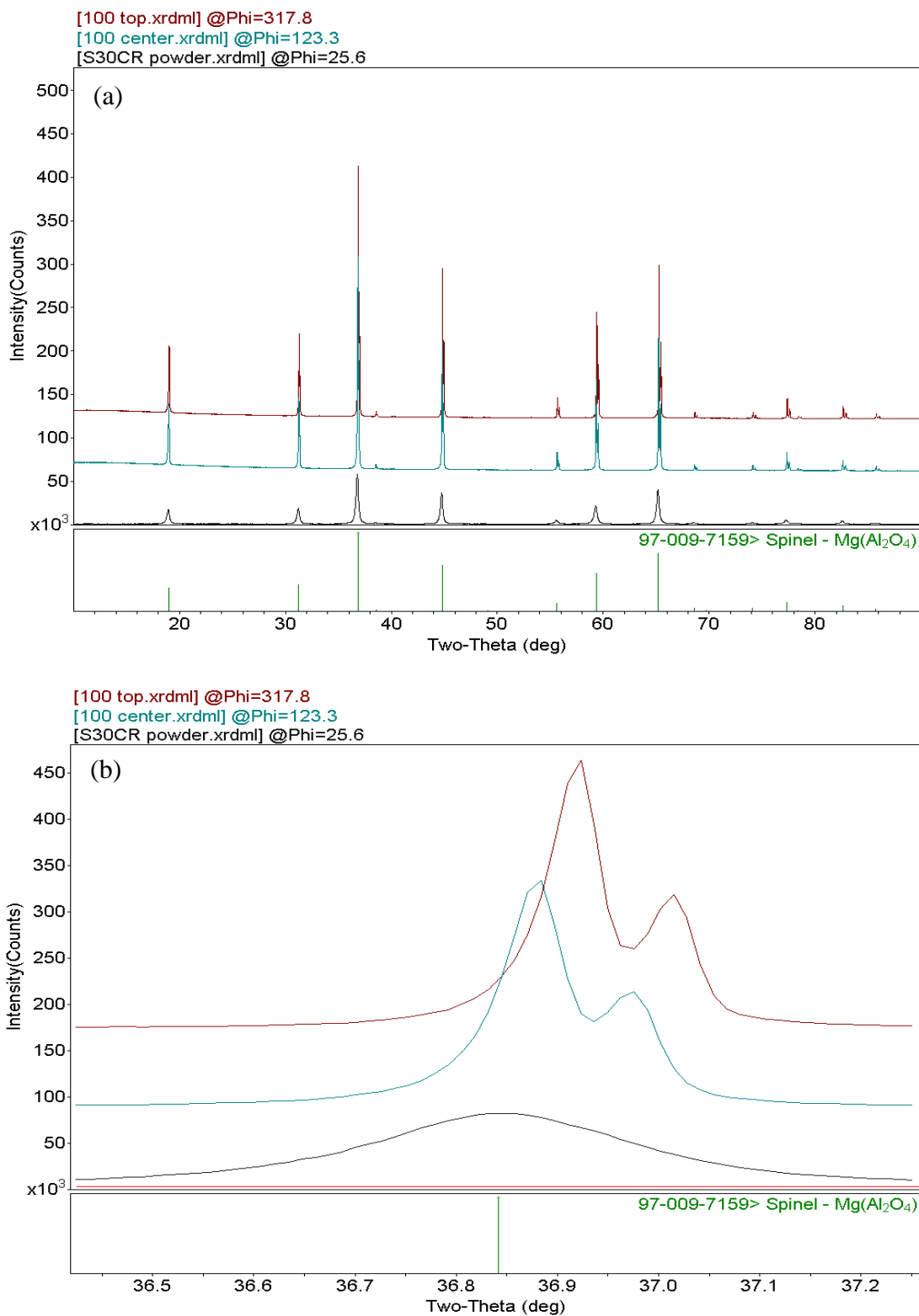


Figure 34. XRD patterns taken at the top and the center of the sample SPS at the heating rate of 100°C/min with a 10 minute hold at 1400°C in comparison with the XRD pattern of the as-received powder: (a) full pattern; (b) zoomed-in pattern at the k-alpha peak.

Figure 35 presents the typical elemental maps processed by energy filtered TEM (EFTEM) of the specimens taken from the top of the sample SPS at the heating rate of 100°C/min. Twinning and stacking faults were not seen, but there was a non-homogeneous distribution Mg and Al the cations over the field of view. Besides the depletion in the concentration of these cations at the pores, there was a depletion of either Mg or Al at particular grains. The depletion of Mg was seen at the grain in the rectangular frame, and the depletion of Al was seen at the grain in the circular frame. Looking back to Figure 33(b), the contrast between grains could be attributed to the non-homogeneous distribution of the Mg and Al cations. Although quantitative chemical mapping of Mg and Al was not available in this work, these observations indicated that the sample had become locally nonstoichiometric while processed at a high SPS heating rate, and it could be the cause of discoloration in the samples.

As discussed in 1.6.3.3, black, gray, brownish and yellowish discoloration was typical in SPS processed ceramics. The problem that should be interpreted was what caused discoloration in spinel. Apparently, carbon diffusion from the graphite die was not the major cause. Referring to samples T1400, T1300, T1200, and T1100, the processing time of T1100 was 40 times longer than that of T1400 in the range of temperature from 1100°C to 1400°C but the discoloration of T1100 was not as severe as that of T1400. According to Fick's second law of diffusion,<sup>199</sup> the concentration of the diffused matter would increase with time. Hence, if carbon diffusion was the case, carbon concentration in T1100 would be expected to be higher than in T1400, and discoloration of T1100 would be expected to be more severe. Since the degree of discoloration of these two sample was in the opposite trend, carbon diffusion could be eliminated as the cause of discoloration in this case.

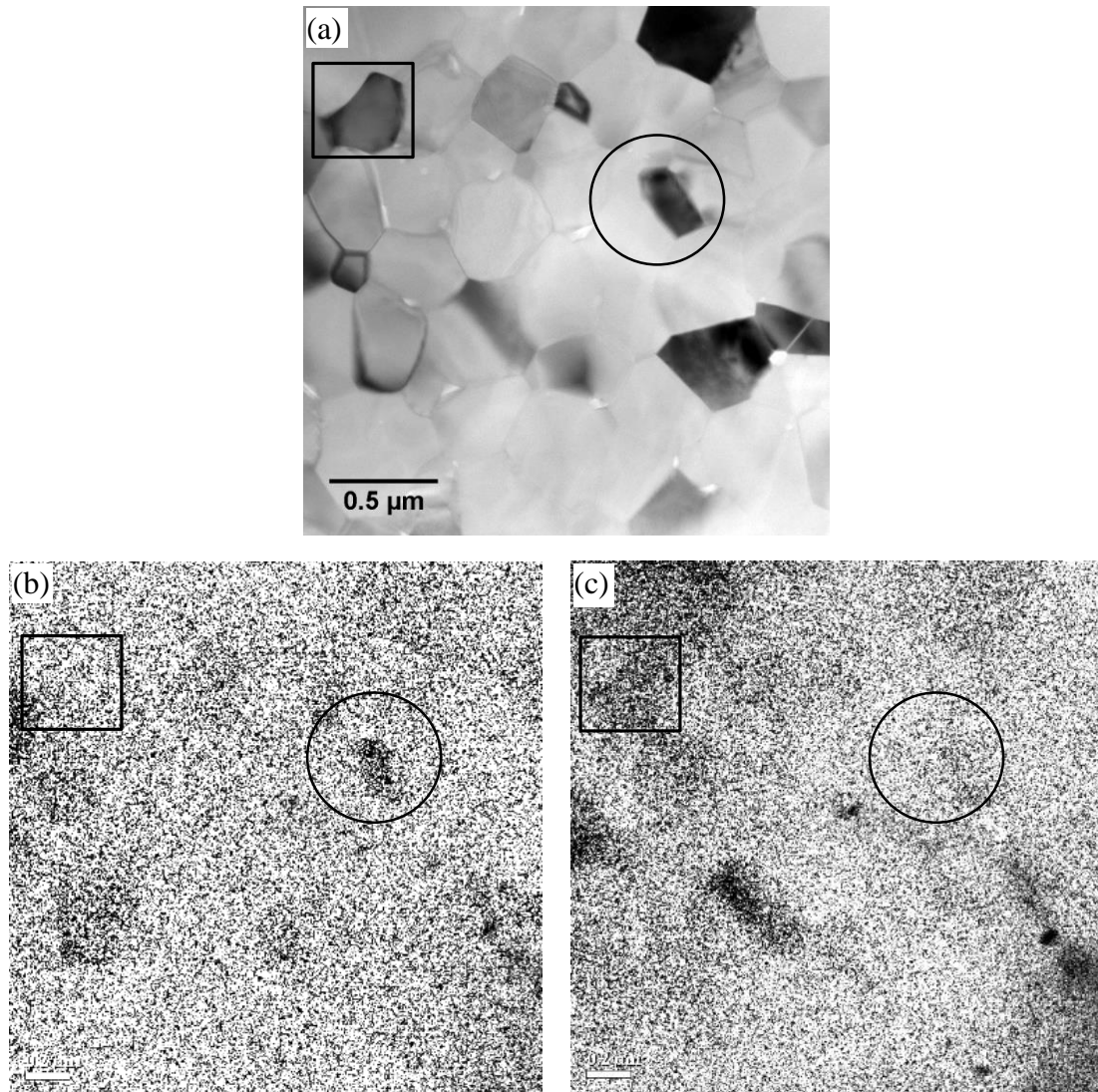


Figure 35. TEM images of the sample SPS at the heating rate of 100°C/min. (a) TEM image showing the grains and pores distribution; (b) EFTEM map of aluminum; and (c) EFTEM map of magnesium.

Another interpretation to be considered was the formation of color centers in the form of oxygen vacancies after exposing to a reducing environment at high temperatures.<sup>180</sup> Again, this is the problem of diffusion, and may not be applicable to explain the black discoloration observed on samples T1400, T1300 and T1200. In case of T1400, black

discoloration occurred at the outermost layer while the center remain of the sample remained white. If the diffusion of oxygen to the immediate surroundings formed oxygen vacancies that caused black discoloration, more severe discoloration would have been observed on the surface of the samples processed for a longer period of time in the SPS. However, as could be seen on T1300 and T1200, the outermost layer of these samples were not black discolored. Instead, this kind of discoloration occurred at the center of the samples. Therefore, the formation of oxygen vacancy could be eliminated as the cause of black discoloration in these cases.

Although the present of the spark plasma in SPS processing is controversial in the literature, observations on the electrical conductivity of spinel and the mobility of the  $Mg^{2+}$  cation at elevated temperatures<sup>102-104, 106, 107</sup> and Inoue's hypothesis on the development of the spark discharge at the early stage of SPS processing<sup>160, 161</sup> could be used to interpret the non-homogeneous distribution of the Mg and Al ions as well as the discoloration of spinel. According to Martinelli et.al.,<sup>106</sup> the mobility of the magnesium cation ( $Mg^{2+}$ ) in spinel was induced near 1000°C by a moderate electric fields, and  $Mg^{2+}$  became the predominant ionic carrier that resulted in a reduction in the Mg/Al ratio. When SPS processing, the powder underwent both thermal treatment and electrical treatment, therefore a similar phenomenon would be expected to occur. The non-homogeneous distribution of Mg and Al in Figure 35 indicated that some of the  $Mg^{2+}$  cations had left the grains causing a variation in the Mg/Al ratio between grains. Magnesium vacancies would play the role of color centers that absorb light at certain wavelengths and induce color for the sample. However, what really worsened the discoloration of spinel could be the development of the spark discharge between grains.

According to Inoue,<sup>159, 160</sup> a light contact was necessary for the development of the spark discharge in SPS processing, and the spark discharge may be terminated upon the particles being welded together. The development of the spark discharge forced the particles into bonding contact with a pressure even greater than that attainable by mechanical means. As will be presented in section 3.3, at the SPS heating rate of 100°C/min, a sample reaches 60% of its theoretical density at 1100°C. It would be the density at which the spark discharge started to develop because different degree of discoloration was observed by altering the heating rate beyond this point. Since discoloration depended on the heating rate, the amount of power introduced into the SPS system would be nontrivial to the generation of the spark discharge, thereby affected the discoloration phenomenon.

Figure 36 presents the power introduced to the SPS system during sintering of 4 grams of the spinel powder. At a stable heating rate, the output current and voltage increased linearly with temperature. As the heating rate was reduced from 100°C/min to 2.5°C/min, the current dropped by approximately 170 apms while the voltage drop by approximately 0.4 volts at the same temperature. At 1180°C for example, the power required by T1100, which was heated at 2.5°C/min, was about 20% less than required by T1200, T1300 and T1400, which were heated at 100°C/min. Since more power was needed at a higher heating rate, the generation of the spark discharge would be more significant at a higher heating rate.

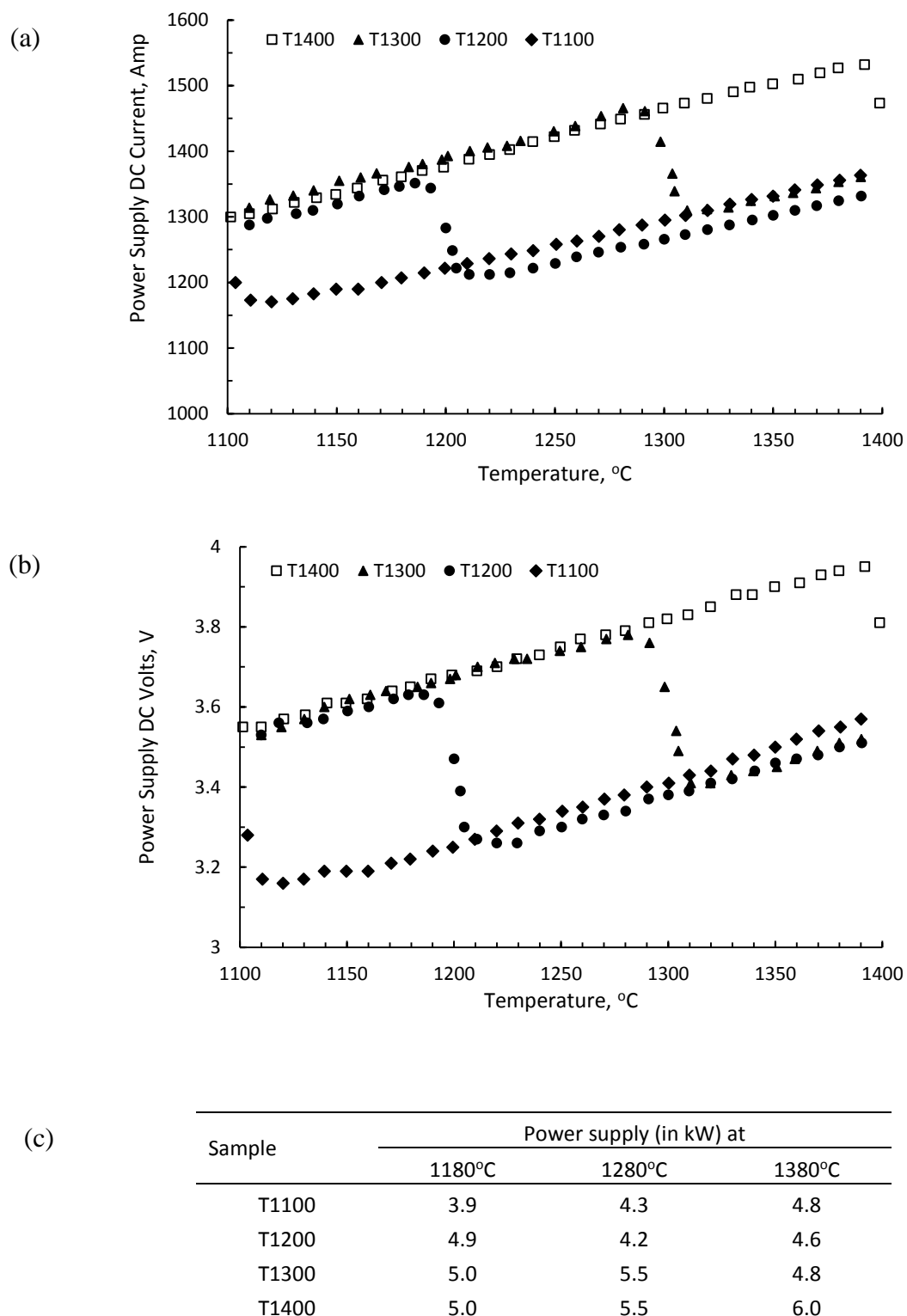


Figure 36. DC power supply during SPS processing: (a) current, (b) voltage, and (c) power supply calculated from (a) and (b).

This work interpreted the black discoloration of SPS processed spinel as that the  $Mg^{2+}$  cations became more mobile at elevated temperature ( $>1000^{\circ}C$ ) and was ready to become ionic current carriers under an electric field. When the powder reached 60% of its theoretical density at  $1100^{\circ}C$ , the spark discharge started to develop. Beyond this point, the generation of the spark discharge was more intense with more power introduced into the system. The spark discharge partially ionize the mutually contacting surfaces of the spinel particles and between the spinel particles and the graphite die. The spark discharge between the spinel particles and the graphite die was predominant when a high intensity current was introduction of the SPS system in a short period of time. It cause a severe ionization of the spinel particles near the contacting surface with the die, and more  $Mg^{2+}$  cations left the lattice as ionic current carriers. At the same time, the outermost layers of the sample was densified by the heat of the die and by the spark discharge effects while the center of the sample remained porous. That was why T1400 was discolored and dense at the outer most layers but remained white and porous at the center.

The spark discharge happened at high current density at the porous part of the sample only. The spark discharge at the mutually contacting surface of the powder and the die of T1300 was less intensive than that of T1400 because of a lower intensity of the current. Concurrently, its outermost layers densified by the heat from the die. The spark discharge was terminated at the dense layers but the  $Mg^{2+}$  cations became more mobile because of a higher temperature. Therefore, the spark discharge with an increased current density moved toward the center of the sample where the porosity remained high. When the power supply was terminated, the edge of the sample was dense and clear while the center of the sample was black discolored. The same explanation could be applied for

T1200. In case of sample T1100, the spark discharge was minimized because of a moderate current intensity. Heat transfer from the die to the powder governed the sintering process resulted in a clearer sample. Since the spark discharge still occurred, discoloration of T1100 was not avoidable but was kept at a much lesser extend compare to the other samples.

Figure 37 shows the HRTEM micrographs taken at a pore and a grain boundary of the top of the sample SPS at the heating rate of 100°C/min to 1400°C, with a 10 minute hold at 1400°C. Screw dislocation presents at the bottom right corner of Figure 37(a). This structure is reflected on the corresponding FFT image. Figure 37(b) shows the HRTEM micrograph taken at the grain boundary of the sample. This is a clean grain boundary without an inter-granular film of an amorphous phase.

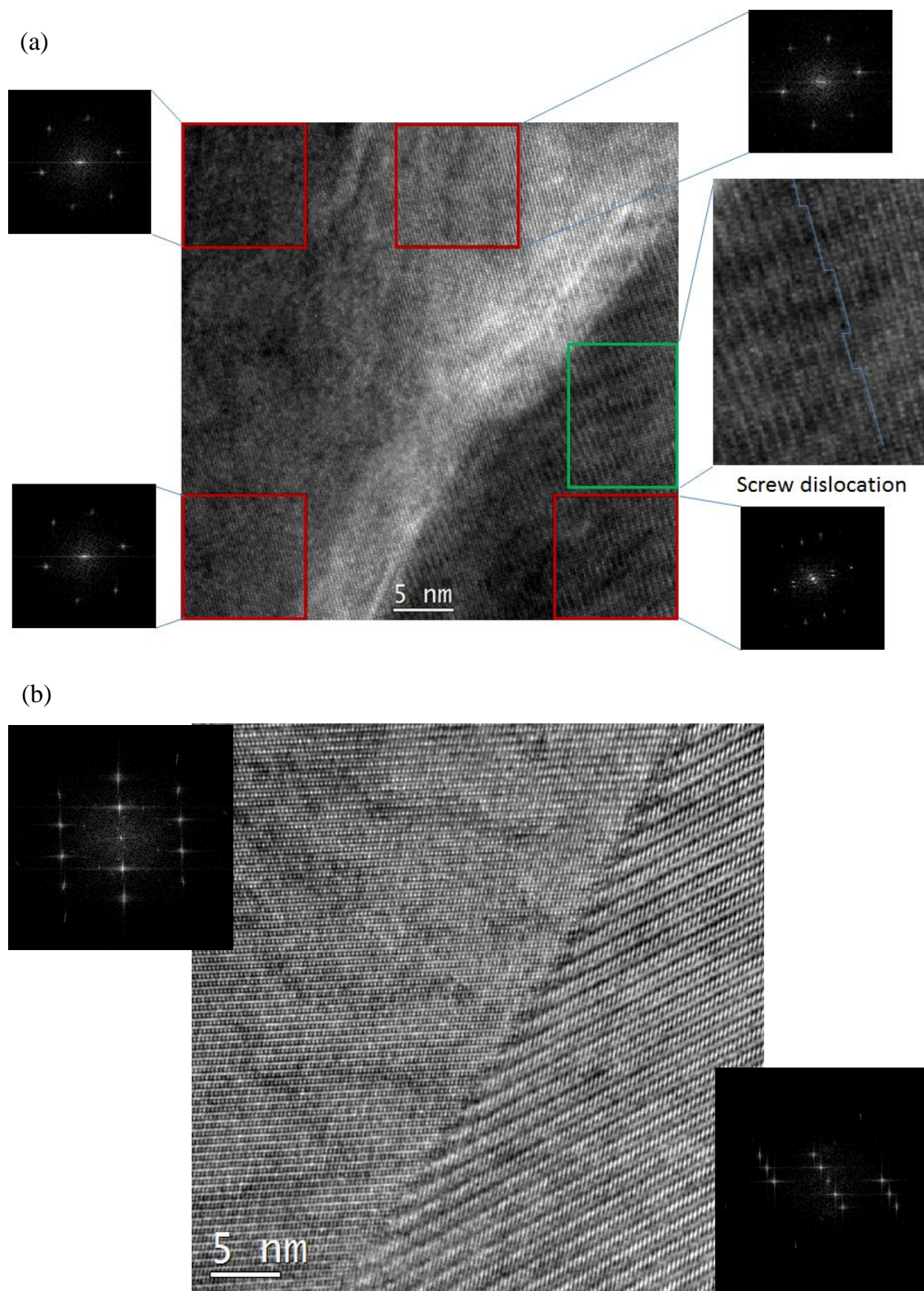


Figure 37. High resolution TEM micrographs taken at (a) a pore and (b) a grain boundary of the top of the sample SPS at the heating rate of  $100^{\circ}\text{C}/\text{min}$  to  $1400^{\circ}\text{C}$  with a 10 minute hold at  $1400^{\circ}\text{C}$ .

### 3.3. Determination of the critical sintering temperatures

Two samples were heated in the SPS to 1400°C, one at the heating rate of 10°C/min and the other at the heating rate of 100°C/min. Figure 38(a) and (b) presents the change in thickness of these samples during the SPS process. The thermal expansion of the graphite die, punches and spacers was eliminated by subtracting the displacement of the electrode when the die was run with spinel powder to that when run without the powder. In case of the sample heated at the rate of 100°C/min, its change in thickness could be divided into three stages, starting with a quick contraction from the beginning of the process until 200°C, followed by a slow contraction over the range of temperatures from 200°C to 800°C, and another quick contraction from 800°C to 1400°C. The rates of contraction of these stages were 1.16 mm/min, 0.17 mm/min and 0.77 mm/min, respectively. In case of the sample heated at the rate of 10°C/min, its change in thickness could be divided into four stages: 0.10 mm/min from room temperature to 200°C, 0.02 mm/min from 200°C to 700°C, 0.08 mm/min from 700°C to 1200°C, and almost unchanged from 1200°C to 1400°C. The contraction of the powder upto 750°C was mainly due to the increasing uniaxial pressure applied on the powder, whereas the contraction beyond this point was primarily due to sintering.

The apparent density of these samples at temperature  $t$  was estimated using the equation:

$$d_t = d \frac{T_t}{T} \quad \text{Eq. 38}$$

where  $d$  was the apparent density of the samples after SPS processing,  $T$  was the thickness of the samples at the end of the heating process, and  $T_t$  was the thickness of the samples at

temperature T. The relative densities of the samples were then calculated using the equation:

$$\rho = 100 \frac{d_t}{D} \quad \text{Eq. 39}$$

where D was the theoretical density of spinel and  $D = 3.578 \text{ g/cm}^3$ .<sup>39</sup> These calculations were approximate because the thermal expansion of the samples was disregarded.

Changes in the relative density of these two samples was plotted as the function of temperature in Figure 38(c), and their relative densities at different temperatures were presented in Table 8. In case of sample SPS at the heating rate of  $10^\circ\text{C}/\text{min}$ , sintering started at about  $800^\circ\text{C}$  and stop at about  $1350^\circ\text{C}$  because the density of the sample increased quickly in this range of temperatures. In case of sample SPS at the heating rate of  $100^\circ\text{C}/\text{min}$ , sintering started at about  $900^\circ\text{C}$  and continued until  $1400^\circ\text{C}$ . These differences demonstrate that the sintering process was postponed to a higher temperature if the SPS heating rate was higher. It also suggested that a high SPS heating rate could only be employed in the lower range of temperatures.

At  $1100^\circ\text{C}$ , the sample SPS at the heating rate of  $100^\circ\text{C}/\text{min}$  reached a relative density of 60%. These were important temperature and density because, as presented in section 3.2, discoloration was minimized if the SPS was run at a low heating rate from  $1100^\circ\text{C}$ .

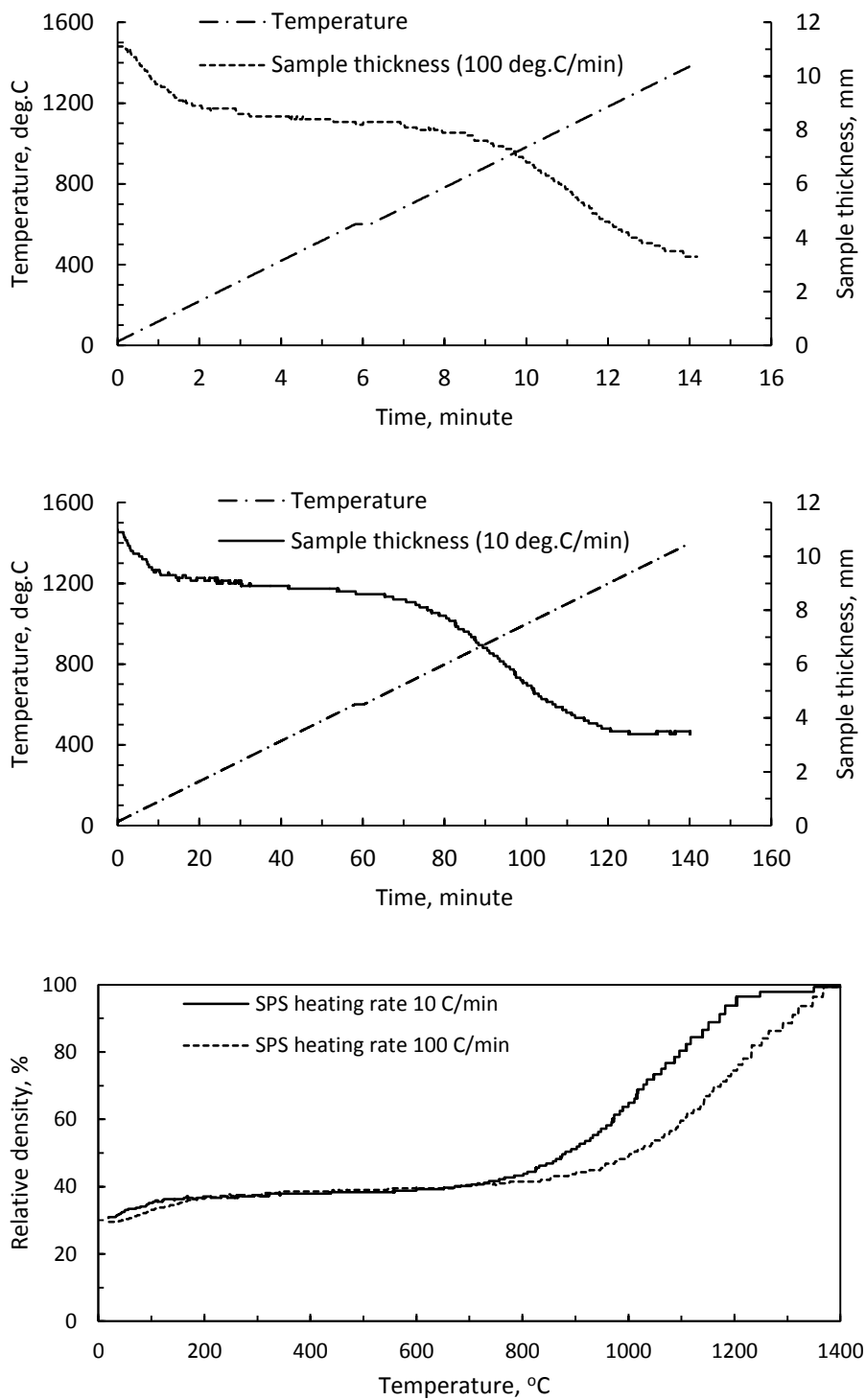


Figure 38. The contraction of the spinel samples during SPS processing.

(a) Change in thickness of sample heated at the rate of 100°C/min as a function of time,  
 (b) Change in thickness of sample heated at the rate of 10°C/min as a function of time,  
 (c) Change in density of samples heated at the rates of 100°C/min and 10°C/min as a function of temperature.

Table 8. Average relative density of the spinel samples during SPS processing.

Temperature, °C	Relative density, %	
	SPS at 100°C/min	SPS at 10°C/min
800	41.5	43.4
900	43.7	51.3
1000	48.9	63.9
1100	59.6	80.7
1200	74.5	94.1
1300	88.6	98.2
1350	96.4	99.7
1400	99.4	99.7

The photographs of these two samples after polishing is presented in Figure 39 and their in-line transmittance is presented in Figure 40. The samples were 3mm-thick and were placed at 40 mm above the text. The sample heated at the rate of 100°C/min had a black color, and it did not transmit light in the visible region. The sample heated at the rate of 10°C/min was translucent with a transmittance of 29% at the 550 nm wavelength. A gradient of brown color from the center to the edge of this sample was observed.



Figure 39. Photographs showing the appearance of samples heated at the rate of (a) 100°C/min, and (b) 10°C/min. The samples had a thickness of about 3 mm and were placed at 40 mm above the text.

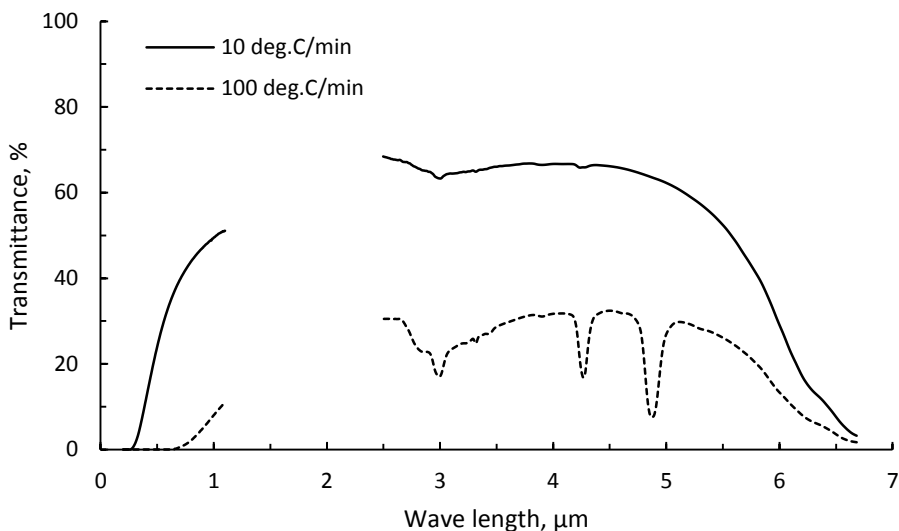


Figure 40. In-line transmittance of the samples SPS at the heating rate of 100°C/min and 10°C/min. The data was normalized to the transmittance at the thickness of 1.8 mm.

From the change in thickness during SPS of these samples, the range of temperatures where the heating rate is controlled was determined. The SPS heating rate was kept at 100°C/min until 1100°C and then at  $\leq 10^\circ\text{C}/\text{min}$  from 1100°C – 1350°C. A 10 minute hold at 1350°C was applied before cooling down. The uniaxial pressure applied on the samples was increased at the rate of 10 MPa/min until it reached 80 MPa and was kept at 80 MPa until the end of the heating cycle.

### 3.4. Effects of the SPS heating rate on the properties of the sintered spinel

Four samples were run at the SPS conditions described above. The heating rates of these samples in the range of temperature from 1100°C to 1300°C were 10°C/min, 5°C/min, 2.5°C/min and 1.25°C/min.

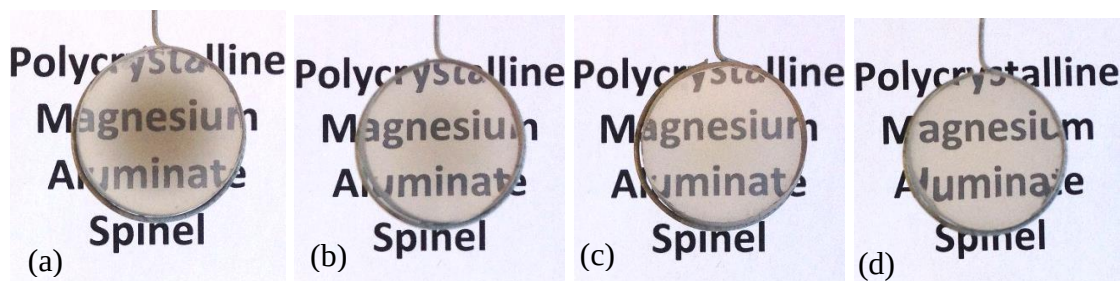


Figure 41. Photographs of the spinel samples SPS at the heating rate of  $100^{\circ}\text{C}/\text{min}$  until  $1100^{\circ}\text{C}$  and then at (a)  $10^{\circ}\text{C}/\text{min}$ , (b)  $5^{\circ}\text{C}/\text{min}$ , (c)  $2.5^{\circ}\text{C}/\text{min}$ , and (d)  $1.25^{\circ}\text{C}/\text{min}$  until  $1350^{\circ}\text{C}$  with a 10 minute hold at  $1350^{\circ}\text{C}$ . The samples were placed at 40 mm above the text.

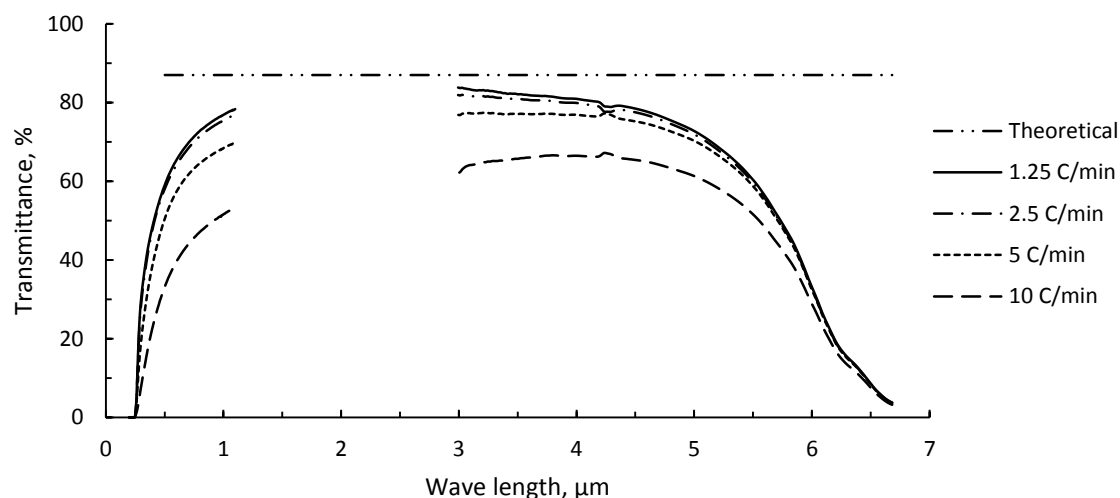


Figure 42. Effects of the SPS heating rate on the transmittance spinel. The samples were SPS at the heating rate of  $100^{\circ}\text{C}$  until  $1100^{\circ}\text{C}$ , and then at lower heating rates, as indicated in the legend, until  $1350^{\circ}\text{C}$  with a 10 minute hold at  $1350^{\circ}\text{C}$ . The data was normalized to the transmittance at the thickness of 1.8 mm.

Figure 41 shows the photographs of the resulted samples and Figure 42 presents their in-line transmittance as a function of the wavelength. As the heating rate was decreased, the discoloration was decreased and the in-line transmittance was increased. In case of samples heated at the rate of  $10^{\circ}\text{C}/\text{min}$  and  $5^{\circ}\text{C}/\text{min}$ , the area close to the edge transmitted more light than the area close to the center of samples. The dark shade appeared at the center of these samples was not seen on samples heated at the rate of  $2.5^{\circ}\text{C}/\text{min}$  and

1.25°C/min. Although the discoloration gradient was diminished, these samples were not completely clear. The in-line transmittance at the 550 nm wavelength of the samples SPS at the heating rates of 10°C/min, 5°C/min, 2.5°C/min and 1.25°C/min was 36.6%, 54.2%, 61.4% and 62.5%, respectively.

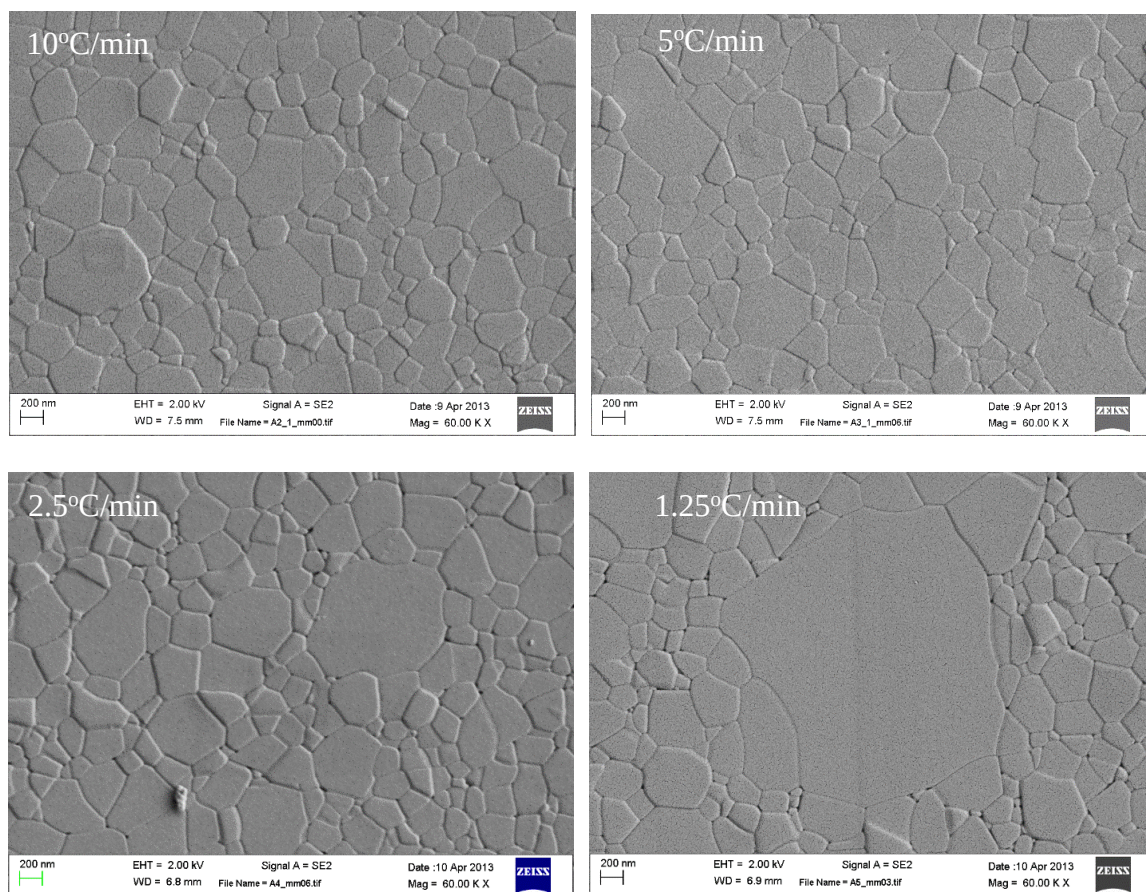


Figure 43. FESEM images of spinel SPSed at the heating rate of 100°C/min until 1100°C, and then at lower rates until 1350°C, with a 10 minute hold at 1350°C.

Figure 43 is the FESEM image of these samples. Their average grain size remained in the submicron range at all SPS heating rates. Some degree of grain growth was observable on the sample SPS at the heating rate of 2.5°C/min, and it became more clearly on the sample heated at 1.25°C/min. The grain size measurement was taken on the plane

that was perpendicular to the SPS pressure direction and was less than 0.5 mm far from the top surface of the samples. The grain size and porosity distributions from the edge to the center of these samples are presented in Figure 44. Images were taken from the edge to the center of the sample with an interval of 1.0 mm. The grain size was measured using the linear interception method with at least 100 interceptions per image. The average porosity of samples SPS at the heating rates from 5 – 1.25°C/min was less than 0.5 vol.%.

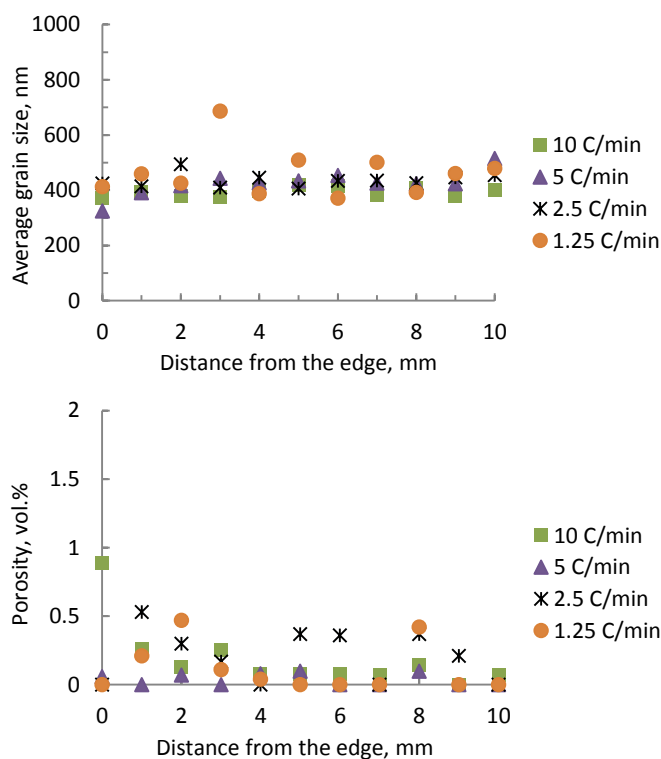


Figure 44. The grain size and porosity distribution samples SPS at different heating rates.

Figure 45 presents the fracture surface of sample SPS at the heating rate of 1.25°C/min. The intergranular fractures was not only propagated through the grain boundaries but also cut through the grains creating a stair-like pattern on the fractured grains.

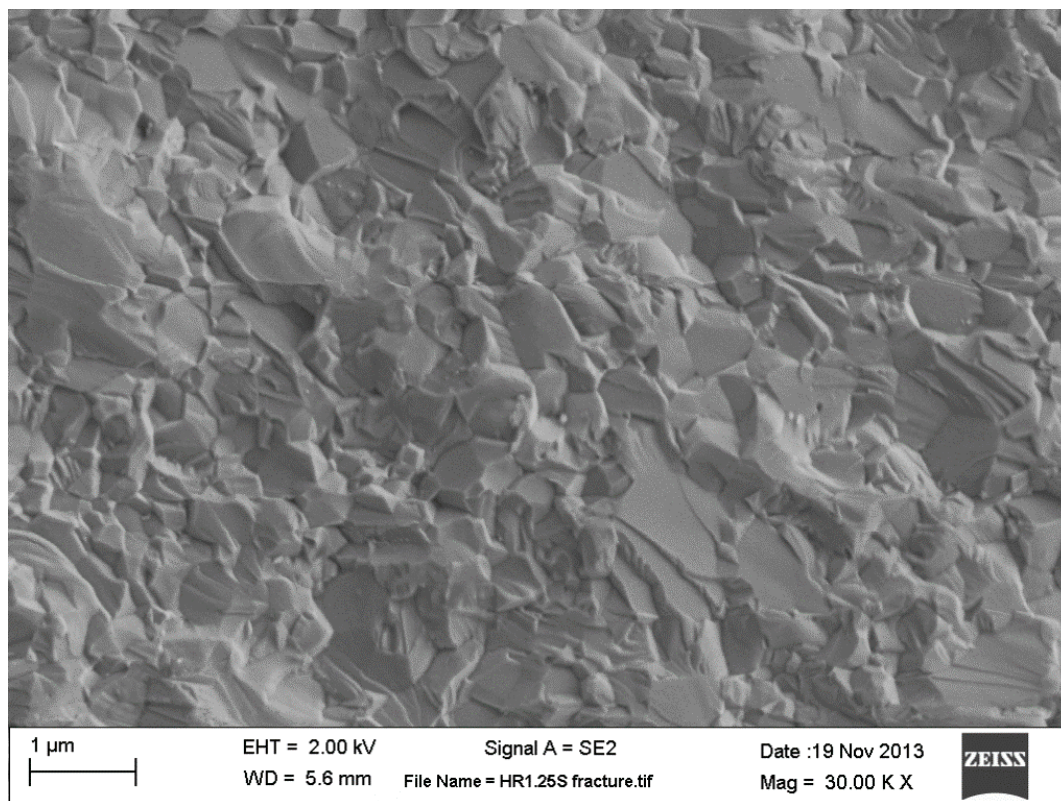


Figure 45. FESEM images of the fractured surface of the sample SPS at the heating rate of  $100^{\circ}\text{C}/\text{min}$  until  $1100^{\circ}\text{C}$ , and then at  $1.25^{\circ}\text{C}/\text{min}$  until  $1350^{\circ}\text{C}$  with a 10 minute hold at  $1350^{\circ}\text{C}$ .

Figure 46 presents the shifting of the XRD peaks of samples SPS at the heating rate of  $10-1.25^{\circ}\text{C}/\text{min}$  in the temperature range of  $1100-1350^{\circ}\text{C}$  compared to the as-received powder. While the as-received powder had a wide single K-alpha peak, all of the SPS samples had two K-alpha peaks, K-alpha 1 and K-alpha 2, and they appeared on the higher angle side. As a result, spinel in the powder form had a lattice parameter of  $8.0878 \text{ \AA}$  while the SPS processed samples had a lattice parameter in the range of  $8.0556 - 8.0610 \text{ \AA}$ . This change in the lattice parameter could be interpreted as due to the formation of the magnesium vacancies during SPS processing. It implied that the stoichiometry of the SPS spinel shifted to the alumina-rich side.

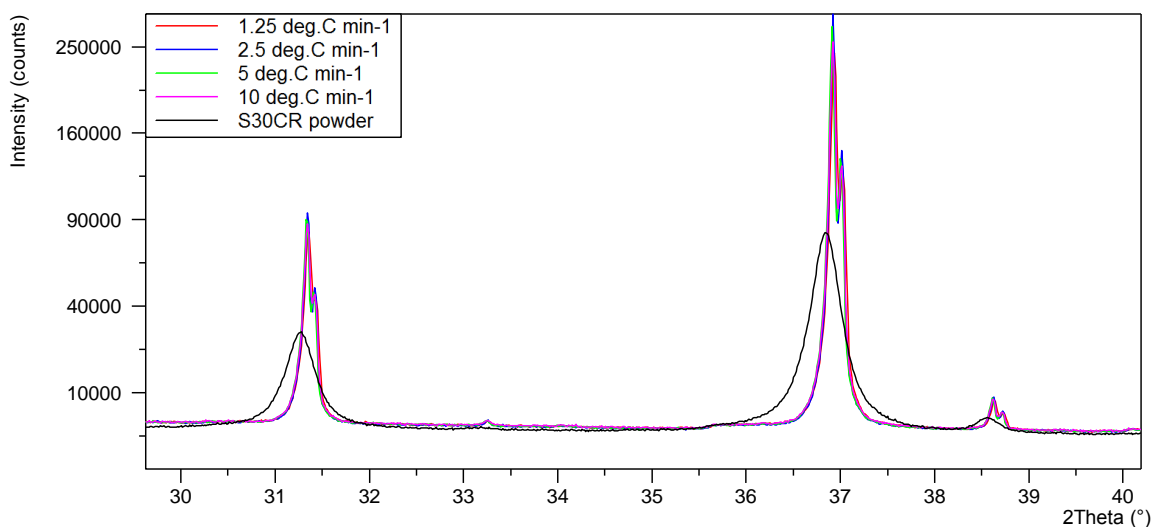


Figure 46. X-ray diffraction of the SPSed samples showing peaks shifting compared to the as-received powder

In general practice, prolonging the heating process after the sample is fully dense is avoided because of the increased processing cost and undesired excessive grain growth. The present work provided another reason for not prolonging the SPS process for transparent spinel: A long processing time at high temperatures would diminish the transmittance of the samples. As the range of temperatures where the heating rate was controlled was enlarged from 1100 – 1350°C to 800 – 1350°C, the transmittance of the samples in the visible region was decreased slightly at all experimental heating rates (Figure 47). However, their transmittance in the infrared region remained the same except the sample SPS at the heating rate of 10°C/min. It suggested that a longer SPS processing time at high temperatures was not favorable.

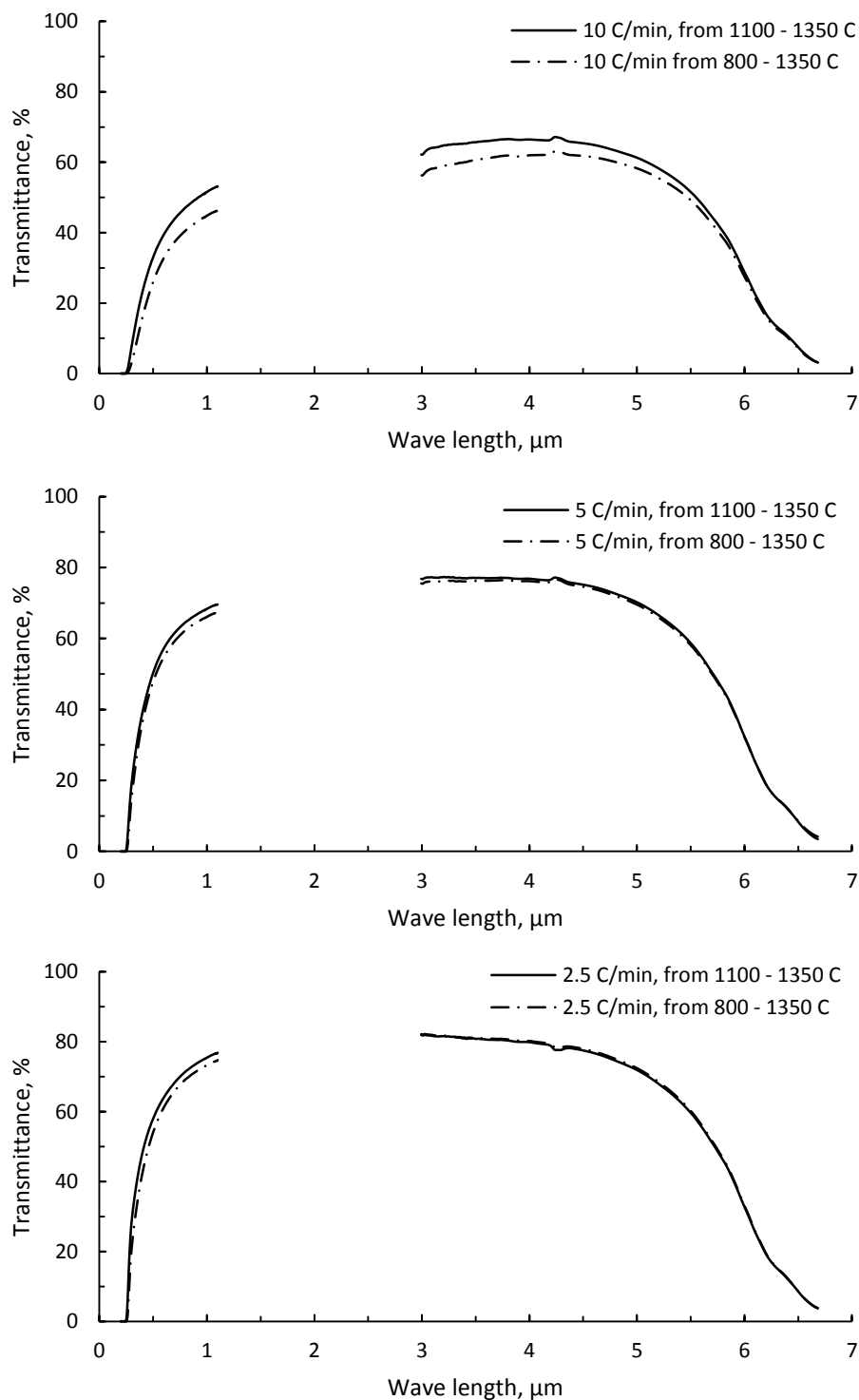


Figure 47. Effects of the controlled heating rates on the transmittance of the spinel. The samples were SPSed at the heating rate of 100°C/min until 800°C or 1100°C, and then at lower heating rates until 1350°C with a 10 minute hold at 1350°C. The data was normalized to the transmittance at the thickness of 1.8 mm.

Figure 48 presents the real-time change in thickness of sample heated at the rate of  $2.5^{\circ}\text{C}/\text{min}$  in the temperature range from  $1100^{\circ}\text{C}$  to  $1350^{\circ}\text{C}$ . Its contraction finished at approximately  $1215^{\circ}\text{C}$ . Beyond that point the thickness of the sample hardly changed.

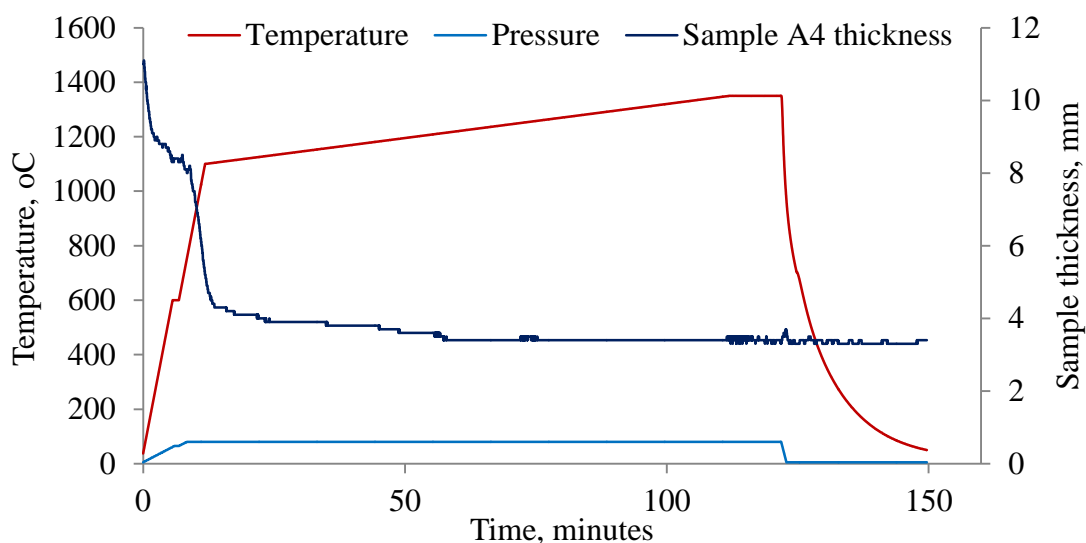


Figure 48. The real-time change in thickness of the sample SPS at  $2.5^{\circ}\text{C}/\text{min}$  in the range of temperatures from  $1100^{\circ}\text{C}$  –  $1350^{\circ}\text{C}$ .

The properties of the sample run with the SPS cycle developed by Bonnefont et.al.<sup>28</sup> was also included in Table 9. It was heated at the rate of  $10^{\circ}\text{C}/\text{min}$  from  $800^{\circ}\text{C}$  to  $1100^{\circ}\text{C}$  and then  $1^{\circ}\text{C}/\text{min}$  from  $1100^{\circ}\text{C}$  to  $1300^{\circ}\text{C}$ . It had a lower density and a larger average grain than the other samples. The transmittance of this sample was about 3% lower than that of the sample SPS at the heating rate of  $2.5^{\circ}\text{C}/\text{min}$ .

Table 9 presents some of the physical properties of samples SPS at the heating rates from  $100^{\circ}\text{C}/\text{min}$  to  $1.25^{\circ}\text{C}/\text{min}$  in the range of temperature from  $1100^{\circ}\text{C}$  to  $1350^{\circ}\text{C}$  with a 10 minute hold at  $1350^{\circ}\text{C}$ . The heating rate played a critical role in the properties of these samples. As the heating rate decreased from  $100^{\circ}\text{C}/\text{min}$  to  $1.25^{\circ}\text{C}/\text{min}$ , the density of the

samples increased from 3.555g/cm<sup>3</sup> to 3.576 g/cm<sup>3</sup>, and the transmittance of the samples increased from 0.0% to 62.5% at the 550nm wavelength. The average grain size was, however, not changed much as they remained less than 500 nm.

Table 9. Effects of the heating rate on the sample properties

Heating rate from 1100°C-1350°C, (°C/min)	Density* (g/cm <sup>3</sup> )	Transmittance (%)		Grain size (nm)	Lattice const. (Å)
		at 550nm	at 4000nm		
Powder	-	-	-	-	8.0878
100	3.555	0	30.7	414	8.0592 (top)
10	3.563	36.6	66.5	392	8.0610
5	3.564	54.2	76.9	425	8.0622
2.5	3.573	61.4	79.9	435	8.0615
1.25	3.576	62.5	80.9	462	8.0556
Bonnefont**	3.567	58.3	-	645	8.0571

\* Archimedes method.

\*\* Rerun the SPS cycle developed by Bonnefont et.al using the selected powder.<sup>28</sup>

### 3.5. Effects of the dwell time on the properties of the SPS-processed spinel

To investigate the effects of the SPS dwell time on the properties of spinel, two more batches of samples were run, one with a one-hour hold and the other with a two-hour hold at 1350°C. Figure 49 presents the photographs of these samples after polishing. A brownish discoloration was seen on all of these samples. In addition, discoloration was further worsen with an increase in the dwell time. This degradation can be attributed to the mobility of the magnesium ions under an electric field at elevated temperatures. The formation of the Frenkel defect with magnesiums ion leaving their place in the lattice,

creating vacancies, and moving toward the cathode of the SPS system can be described using the Kroger-Vink notation:<sup>70</sup>



where  $\text{Mg}_{\text{Mg}}^{\times}$  is a magnesium ion sitting on a magnesium lattice site with neutral charge,  $\text{V}_{\text{Mg}}''$  is a magnesium vacancy with a double negative charge, and  $\text{Mg}_i^{\cdot\cdot}$  a magnesium interstitial ion with a double positive charge. This reaction could lead to a thermal-electrical runaway as was observed on spinel and MgO.<sup>107, 200</sup>

The microstructures of these samples are presented in Figure 50. The samples were slightly over etched, hence nano-size pores were observed at the trigranular junctions. As expected, an increase in the dwell time resulted in an increase in the grain size (Table 10), and widen the grain size distribution range as some grains grew to the micron scale. However, the average grain size of these samples remained in the submicron range.

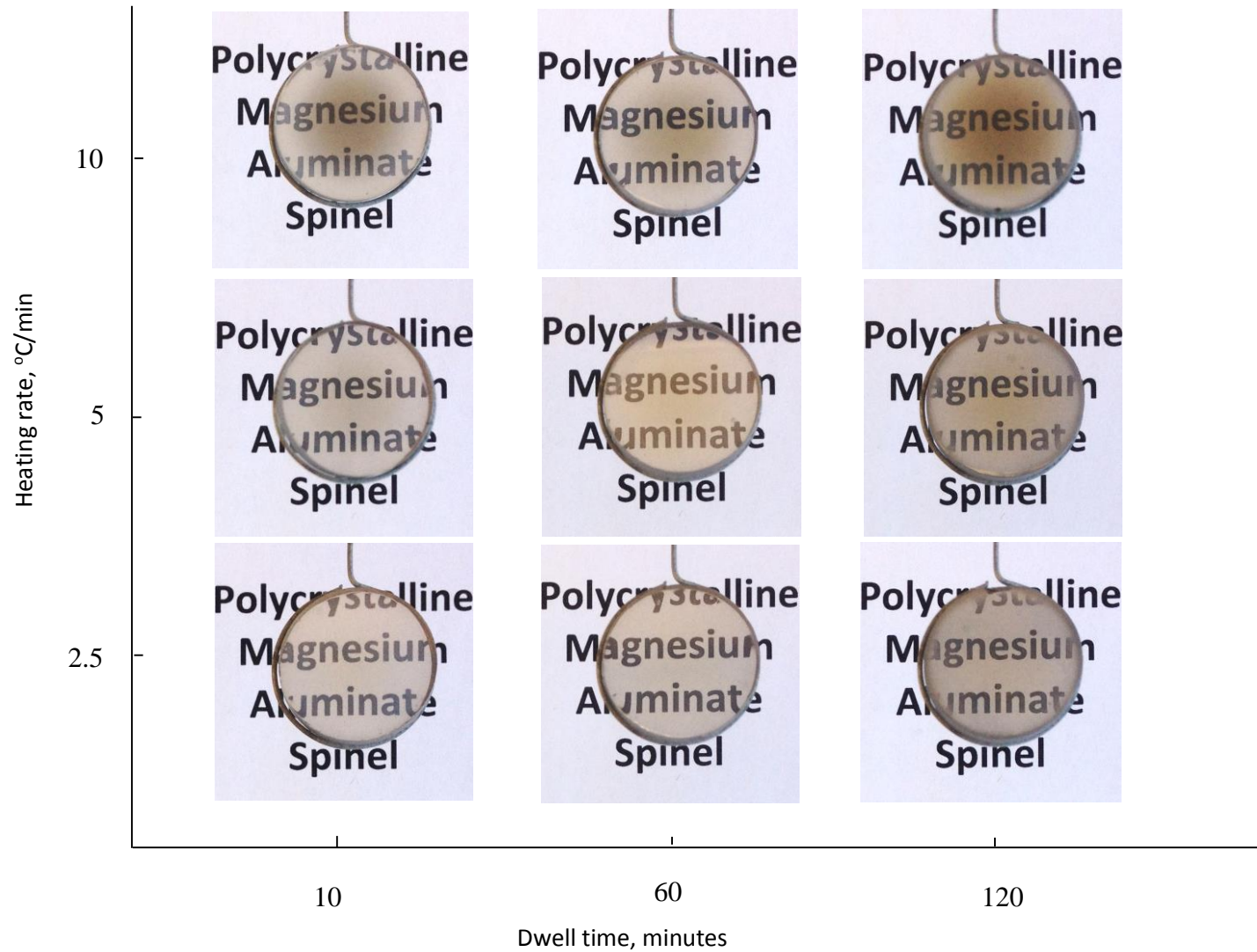


Figure 49. Photographs showing the effects of the dwell time on the transparency of SPS spinel.

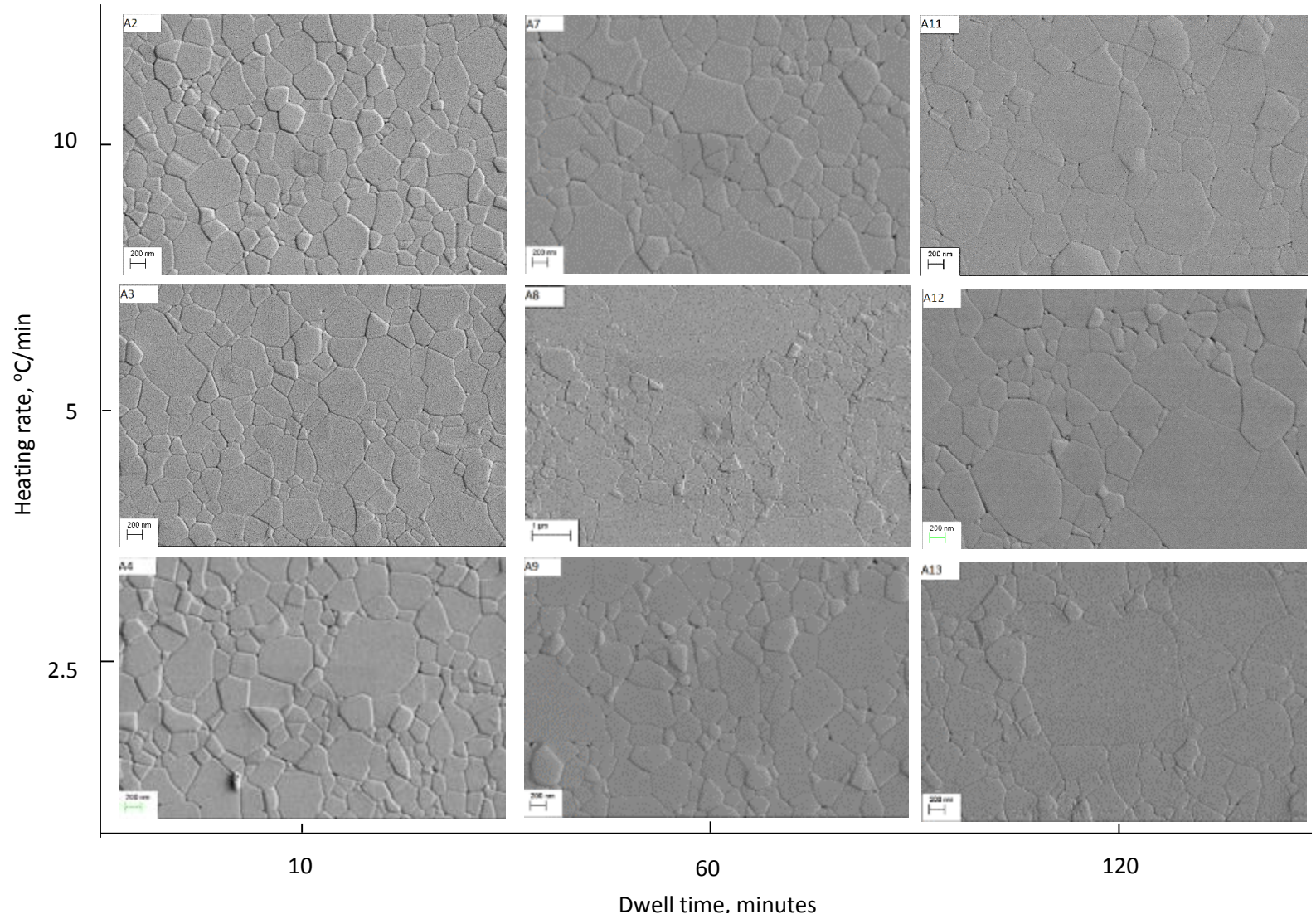


Figure 50. SEM images showing the effects of the dwell time on the microstructure of SPS spinel.

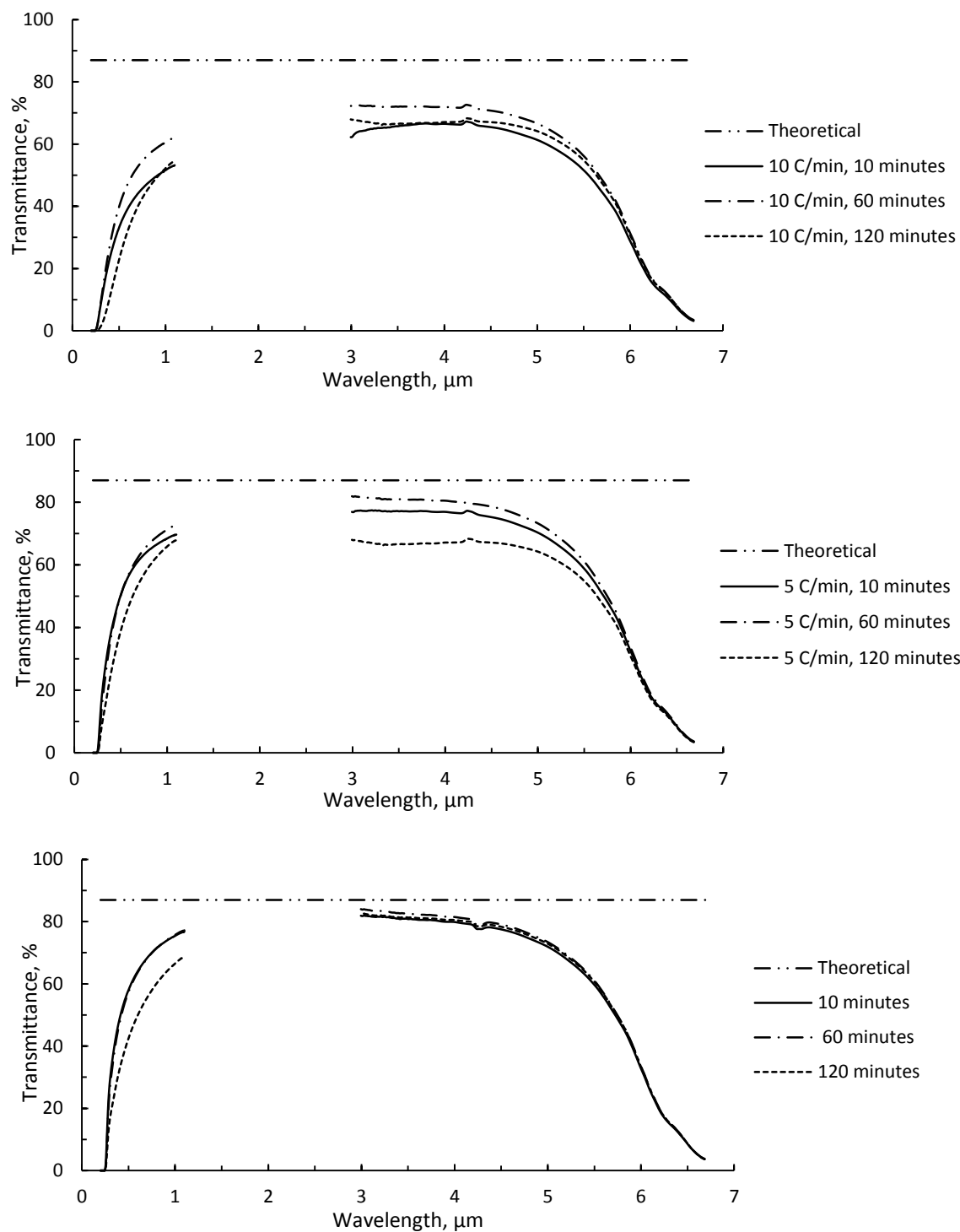


Figure 51. Illustration of the effects of the SPS dwell time on the transmittance of spinel.

Figure 51 presents the in-line transmittance of these samples in the visible and mid IR wavelength range. As the dwell time was increased from 10 minutes to 60 minutes, the in-line transmittance in the vision region was increased for the sample SPS at the heating rate of 10°C/min but almost remained the same for the samples SPS at the heating rates of 5°C/min and 2.5°C/min. However, as the dwell time was increased to 120 minutes, the transmittance of the samples was significantly decreased at all experimental heating rates. In case of the samples SPS at the heating rate of 2.5°C/min, a change in the dwell time did not affect the transmittance in the mid-IR region. The effects of the heating rate and dwell time on the density, transmittance, grain size and lattice parameter of SPS- processed spinel are presented in Table 10.

Table 10. Effects of the heating rate and the dwell time on the sample properties

SPS conditions	Density* g/cm <sup>3</sup>	Transmittance, %		Grain size nm	Lattice const. Å
		at 550nm	at 4000nm		
10°C/min, 10 min.	3.563	36.6	66.5	392	0.80610
5°C/min, 10 min.	3.564	54.2	76.9	425	0.80622
2.5°C/min, 10 min.	3.573	61.4	79.9	435	0.80615
10°C/min, 60 min.	3.567	44.0	71.9	469	0.80628
5°C/min, 60 min.	3.568	54.4	80.4	944	0.80597
2.5°C/min, 60 min.	3.573	60.9	81.5	540	0.80621
10°C/min, 120 min.	3.567	28.0	67.0	534	0.80593
5°C/min, 120 min.	3.570	43.8	67.1	658	0.80599
2.5°C/min, 120 min.	3.572	46.4	80.5	523	0.80590

\* Archimedes method.

### 3.6. Effects HIP post SPS on the properties of SPS-processed spinel

Two samples were sent to Armorline (Armorline Corporation, Indian Land, South Carolina) for HIP post SPS, one was the samples SPS solely at the heating rate of 100°C/min with a 10 minute hold at 1350°C, the other was the samples SPS at the heating rate of 100°C/min to 1100°C and then at 2.5°C/min to 1350°C with a 10 minute hold at 1350°C. The samples was HIP 1750°C for 12 hours in argon under a pressure of 30 ksi.

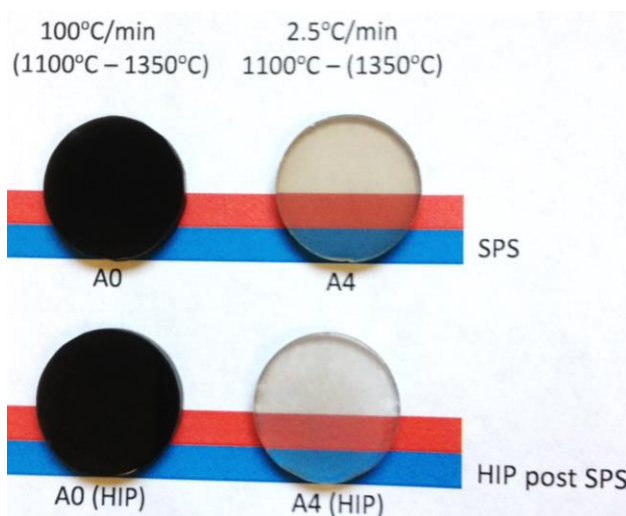


Figure 52. Photograph of the SPS-processed samples before and after HIP.

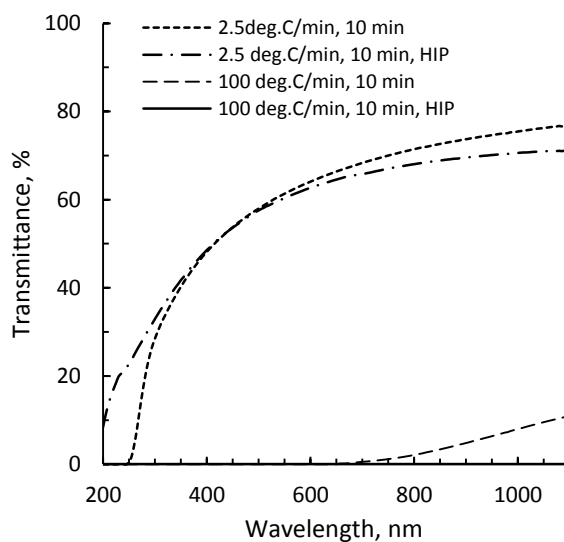


Figure 53. HIP post SPS did not improve the transmittance of SPS processed spinel. Data was normalized to the transmittance at the thickness of 1.8 mm.

A photograph of the samples before and after HIP is presented in Figure 52. The black discoloration was not cured by HIP, but the brownish discoloration was cured at some degree. It is reflected by the transmittance as shown in Figure 53. Initially, the sample SPS at the heating rate of 100°C/min had a transmittance of 11% at the 1100 nm wavelength. After HIP, it completely lost this transmittance. In case of the sample SPS at the heating rate of 2.5°C/min, it became more transparent in the UV region and less transparent in the near IR region. In addition, its clarity was not homogeneous (Figure 54). A cloudy shade presented within the samples and discoloration occurred at the grain boundaries. The grains of the sample were about 0.5 – 1 mm in size, and were viewable by naked eyes. Exaggerated grain growth, so-called secondary recrystallization was expected in this case because of a long heat treatment time (12 hours) at 1750°C. Along with the growth of the grains, intrinsic impurities and defects were excluded from the bulk of a grain during recrystallization and gathered at the grain boundaries.<sup>143, 201, 202</sup> Therefore, discoloration was observed at the grain boundaries.

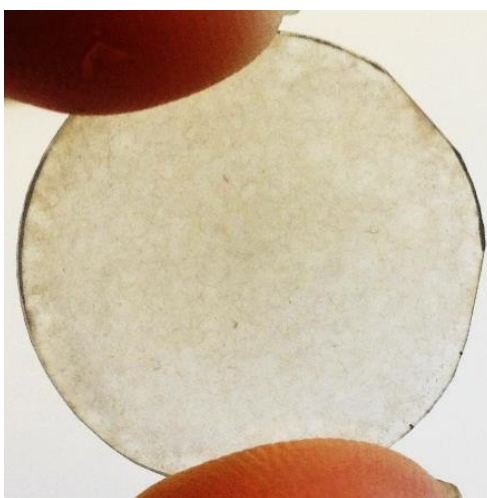


Figure 54. Photograph showing the inhomogeneity in the transparency of SPS-processed spinel after HIP.

### 3.7. Summary

Transparent polycrystalline spinel samples was produced by SPS processing. The transmittance of the samples was heating rate and dwell time dependent. A high heating rate at elevated temperature resulted in a severe discoloration, and a long dwell time diminished the transmittance of the samples.

Discoloration was unavoidable in SPS-processed spinel. It was interpreted as being due to the mobility of the magnesium ions undergoing an electric field at elevated temperature. The magnesium ions left their places in the spinel lattice as the current carriers, creating magnesium vacancies which later played the role of a color center.

HIP post SPS did not cure the discoloration. In addition, it exacerbated unwanted qualities including exaggerated grain growth and inhomogeneity.

#### 4. Effects of doping on the properties of SPS-processed spinel

##### 4.1. Characterization of the alumina doped spinel powder

The powder doped with 10 wt.% of alumina, S10A, was selected to perform FTIR analysis. The powder was heated to 400°C, 600°C, 800°C and 1000°C with a ten minute hold at these temperatures. After heating each sample was mixed with KBr and pressed to form a 1 mm thick pellet. The weight percentage of the powder in the mixture was 1%.

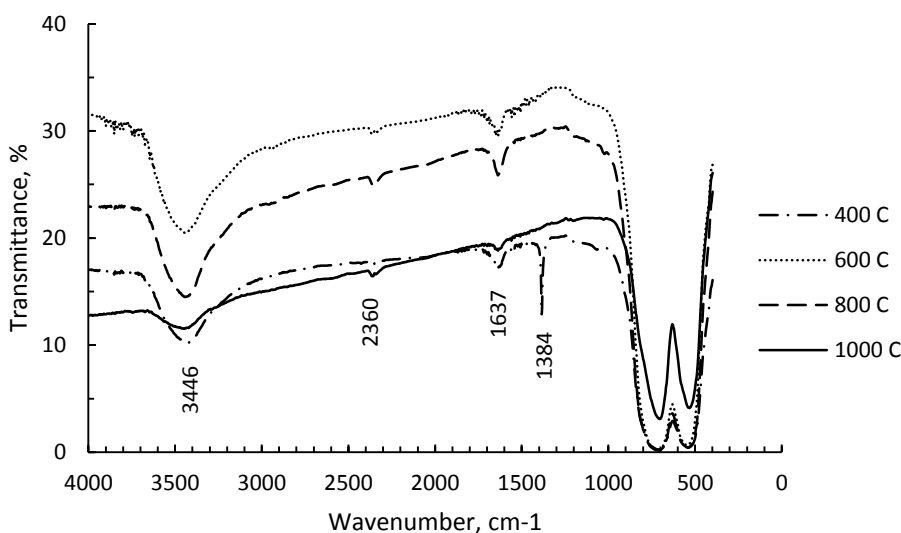


Figure 55. FTIR spectra of the alumina coated powder.

Figure 55 presents the transmittance of the infrared lights through the pellets. The IR absorption band of the N-O stretching appeared at the 1384 cm<sup>-1</sup> wavenumber on the spectrum of the sample heated at 400°C. The IR absorption band of the C=O stretching appeared at the 2360 cm<sup>-1</sup> wave number, and that of the O-H stretching appeared at the 1637 cm<sup>-1</sup>. The wide absorption band near the 3500 cm<sup>-1</sup> could belong to the O-H stretching (at the 3446 cm<sup>-1</sup> wavenumber). However, as the absorption band of the O-H bonding at

1637  $\text{cm}^{-1}$  disappeared after the powder was heated at 1000°C, the one near 3500  $\text{cm}^{-1}$  remained anonymous.

The N-O bonding was not expected to present after the powder was a heat treated at 400°C because the decomposition of aluminum nitrate and ammonium nitrate are at 275°C and 210°C, respectively. The present of the N-O bonding could be interpreted as that aluminum hydroxide formed during the coating process had entrapped the nitrates and slowed down the decomposition of these substances. The decomposition of the nitrates was completed at temperatures before 600°C because no IR absorption band of the N-O bonding appeared on the spectra of the powder heated at 600°C and higher.

Ambient water might contribute to the present of the O-H bonding. However, since aluminum hydrate was one of the constituents of the sample, it should be the predominant factor that contributed to the present of the absorption peak of the O-H bonding rather than the ambient water. It should be noted that the width and the depth of the absorption band near the 3500  $\text{cm}^{-1}$  wavenumber attenuated as the heat treating temperature increased.

The present of the C=O bonding was due to ambient carbon dioxide taken by the instrument because no carbonate or organic substances were introduced to the doping process.

After the doped powder was heat treated at a higher temperature, the newly formed  $\text{Al}_2\text{O}_3$  could stay in the powder in several possibilities: It was coated on the spinel particles as a continuous or discontinuous layer (Figure 56 (a-b)); It participated in the structure of spinel to form an alumina rich solid solution (Figure 56(c)); It stayed as a separate phase and was detached from the spinel particles (Figure 56(d)); Or it diffused into the outermost layers of the spinel particles and formed a solid solution in there (Figure 56(e-g)).

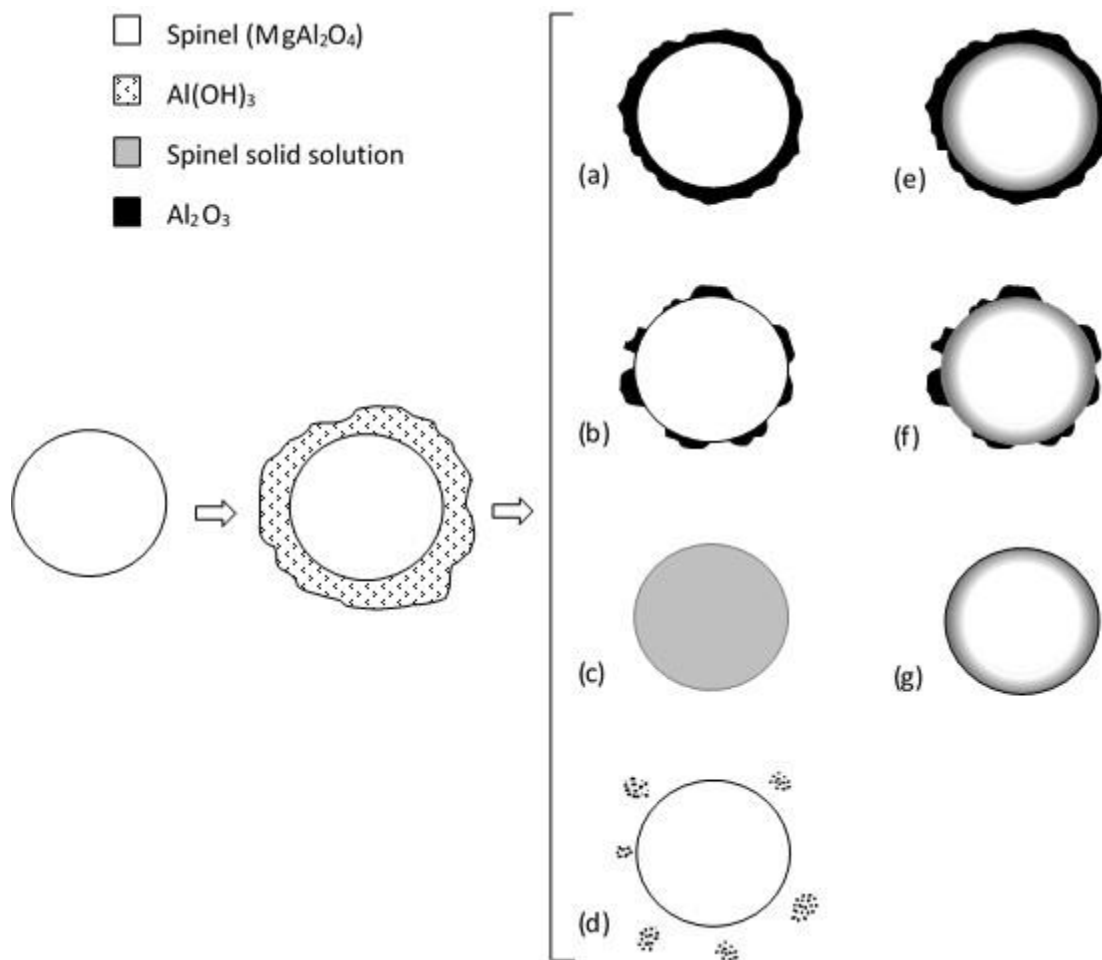


Figure 56. Illustration of the possibilities of how the newly formed  $\text{Al}_2\text{O}_3$  took part in the spinel powder.

Even when alumina was homogeneously coated on the spinel particle without forming a solid solution, calculating the thickness of the coating layer was impossible because of the various particle shapes and complicated surface structures of the as received powder. Therefore, this work took two extremes to estimate the possible thickness of the coating layer. One was to disregard the complicated curved surface of the spinel particles, and the other was to assume that the spinel particles were spherical.

Assuming that coating was homogeneous and continuous and the coated surface was flat, the thickness,  $H$ , of the coating layer can be estimated using a simple equation:

$$H = V_d/S \quad \text{Eq. 41}$$

where  $V_d$  is the total volume of the coating layer,  $S$  is the total surface of the powder.

$$V_d = m_d/\rho_d \quad \text{Eq. 42}$$

$$S = S_{\text{BET}} \cdot m \quad \text{Eq. 43}$$

where  $m_d$  is the mass of the dopant,  $\rho_d$  is the density of the dopant, the calculated density of corundum is  $3.997 \text{ g/cm}^3$ ,<sup>39</sup>  $S_{\text{BET}}$  is the surface area of the host powder,  $m$  is the mass of the doped powder. Therefore,

$$H = \frac{m}{M} \frac{1}{\rho S_{\text{BET}}} \quad \text{Eq. 44}$$

The thickness of the coating layer of the spinel powder doped with 10wt% of  $\text{Al}_2\text{O}_3$ , S10A, would be 14.64 nm. This thickness should be viewable by a regular TEM.

At another extreme, assuming that the spinel particles were spherical and of the same size, and alumina was coated homogeneously and continuously on these particles, the thickness of the coating layer,  $H$ , would be the length difference between the radius of the coated sphere,  $r_2$ , and the uncoated sphere,  $r_1$ :

$$H = r_2 - r_1 \quad \text{Eq. 45}$$

The specific surface,  $S_{\text{spec}}$ , can then be calculated from the mass and surface area of the sphere:

$$S_{\text{spec}} = \frac{A_1}{m_1} = \frac{A_1}{V_1 \rho} \quad \text{Eq. 46}$$

where  $A_1$ ,  $V_1$ , and  $m_1$  is respectively the surface area, volume and mass of the sphere, and  $\rho$  is the density of the sphere. For spinel  $\rho = 3.578 \text{ g/cm}^3$ .<sup>39</sup>

Taking BET surface area as the specific area, it can be expressed as:

$$S_{\text{BET}} = \frac{S}{m} = \frac{nA_1}{nV_1\rho} = \frac{A_1}{V_1\rho} \quad \text{Eq. 47}$$

where  $m$  is the mass of the powder,  $S$  is the total surface of the powder, and  $n$  is number of the sphere particles in the powder.

The surface area,  $A$ , and volume,  $V$ , of a sphere with a radius  $r$  are calculated by:

$$A = 4\pi r^2 \quad \text{Eq. 48}$$

$$V = \frac{4}{3}\pi r^3 \quad \text{Eq. 49}$$

Therefore, the radius of a sphere particle of the powder is:

$$r_1 = \frac{3V_1}{A_1} = \frac{3}{S_{\text{BET}}\rho} \quad \text{Eq. 50}$$

$$r_2 = \sqrt[3]{\frac{3V_2}{4\pi}} = \sqrt[3]{\frac{3(V_1 + V_c)}{4\pi}} \quad \text{Eq. 51}$$

where  $V_2$  is the volume of the coated sphere, and  $V_c$  is the volume of the coating layer.

$$V_c = \frac{V_d}{n} = \frac{m_d}{n\rho_d} \quad \text{Eq. 52}$$

where  $n$  is the number of spheres in the powder,  $V_d$ ,  $m_d$  and  $\rho_d$  is respectively the volume, mass, and density of the coating material. For corundum,  $\rho_d = 3.997 \text{ g/cm}^3$ .

$$n = \frac{S}{A_1} = \frac{mS_{\text{BET}}}{4\pi r_1^2} = \frac{mS_{\text{BET}}}{4\pi \left(\frac{3}{S_{\text{BET}}\rho}\right)^2} = \frac{mS_{\text{BET}}^3\rho^2}{36\pi} \quad \text{Eq. 53}$$

$$V_c = \frac{m_d}{\frac{mS_{\text{BET}}^3\rho^2}{36\pi} \rho_d} = \frac{36\pi m_d}{mS_{\text{BET}}^3\rho^2\rho_d} \quad \text{Eq. 54}$$

Therefore,

$$H = \sqrt[3]{\frac{3 \left[ \frac{4}{3} \pi \left( \frac{3}{S_{\text{BET}} \rho} \right)^3 + \frac{36 \pi m_d}{m S_{\text{BET}}^3 \rho^2 \rho_d} \right]}{4 \pi}} - \frac{3}{S_{\text{BET}} \rho} = 3 \sqrt[3]{\frac{1}{S_{\text{BET}}^3 \rho^3} + \frac{m_d}{m S_{\text{BET}}^3 \rho^2 \rho_d}} - \frac{3}{S_{\text{BET}} \rho}$$

Eq. 55

With 10wt% of alumina added to spinel,  $H = 0.89$  nm. The thickness of the coating layer is about the length of the lattice parameter of spinel and might not be viewable by a regular TEM.

Figure 57 compares the morphology of the undoped powder, S30CR and the 10%  $\text{Al}_2\text{O}_3$  doped powder, S10A. The surfaces of the undoped and doped particles were clean, and the edges of the grains on both case were well-defined. No amorphous phase or crystalline phase of  $\text{Al}_2\text{O}_3$  was observable.

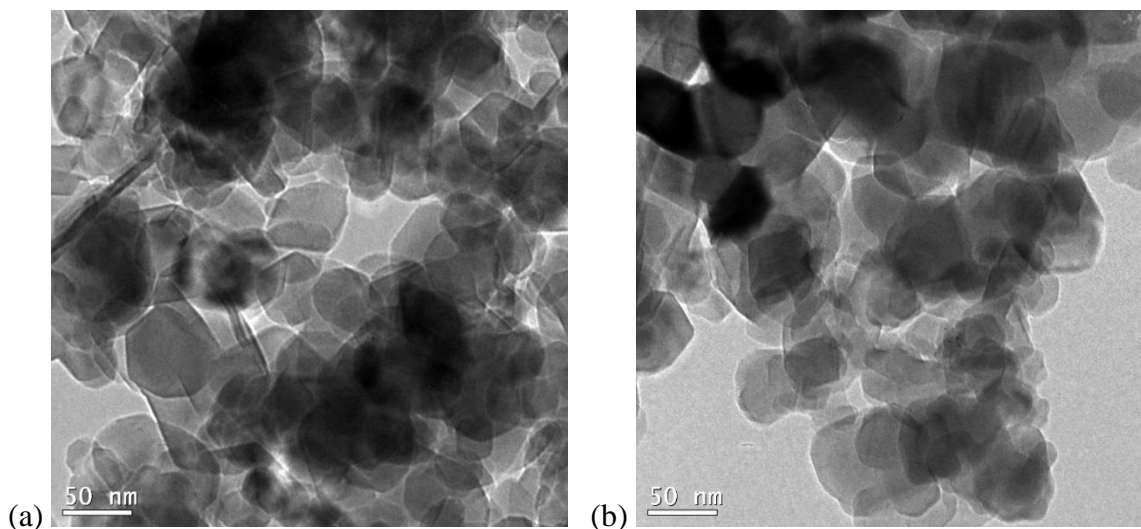


Figure 57. TEM images of (a) the undoped powder, S30CR, and (b) the 10 wt%  $\text{Al}_2\text{O}_3$  doped powder, S10A.

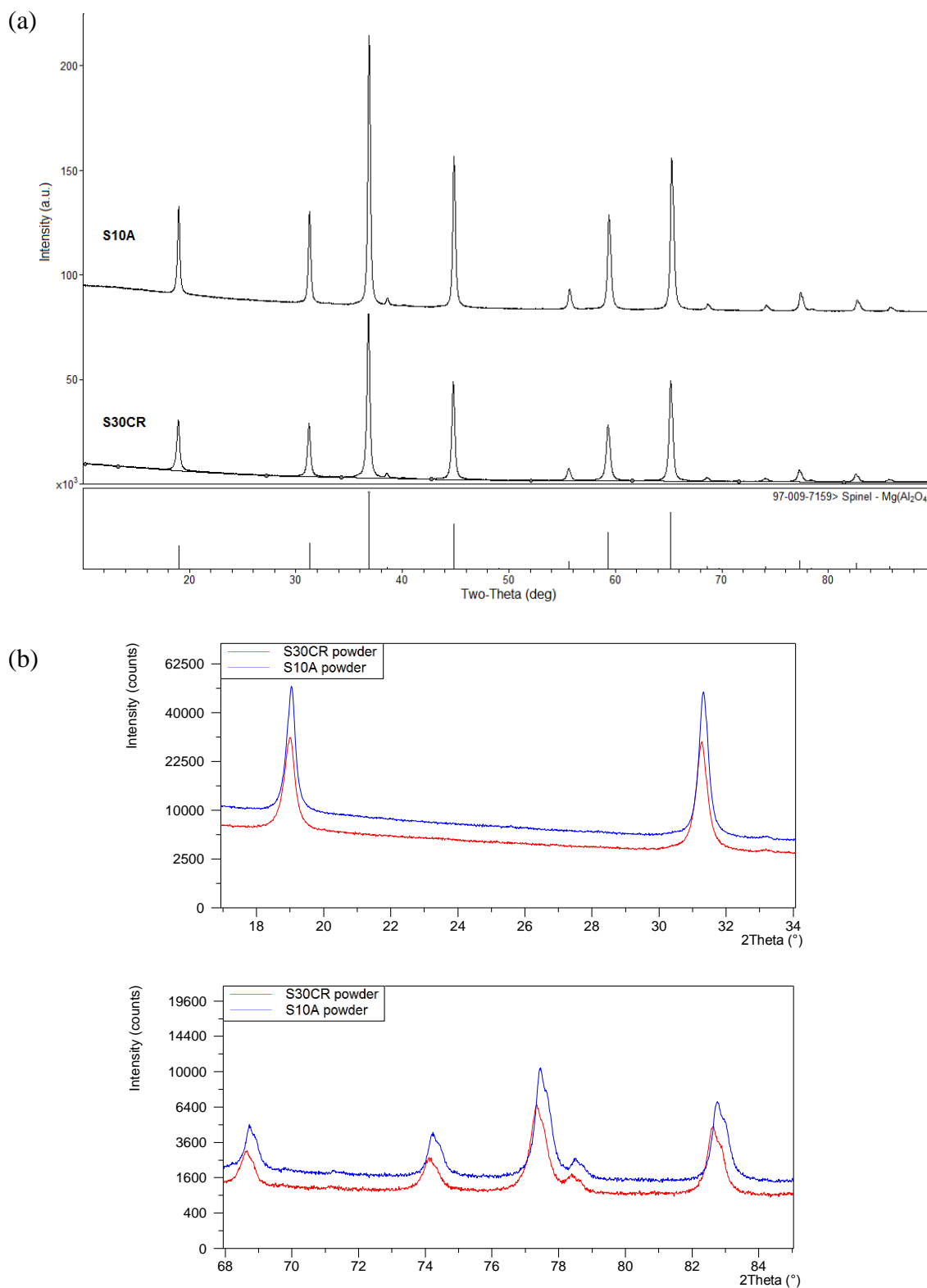


Figure 58. X-ray diffraction of an 10 wt.% alumina-doped spinel powder, S10A, compare to the as-received powder, S30CR. (a) No new phase was formed; (b) Peak shift at the low angles was less than peak shift at the high angles

Figure 58 presents the XRD pattern of powder S10A compare to that of the undoped powder. There was no new phase present in the doped powder. However, the diffraction peaks of S10A were slightly shifted to the high-angle side, causing a reduction in the lattice parameter from 8.0878 Å to 8.0756 Å. Peak shift was increased at the high angles.

With 10 wt.% of alumina added to the spinel powder, if alumina stayed as a separate crystalline phase, it should be detectable as corundum by X-ray diffraction. The absence of the corundum phase together with the contraction of the lattice parameter indicated that Al<sub>2</sub>O<sub>3</sub> either presented as an amorphous phase, or had been diffused into the crystal structure of the spinel powder and formed an alumina rich solid solution, or both.

## **4.2. Characterization of the doped samples after SPS processing**

The doped powders were sintered using the optimized SPS condition. That is, the powder was heated at the heating rate of 100°C/min until 1100°C, and at 2.5°C/min until 1350°C. A 10 minute hold was applied at 1350°C before the samples was cooled at the rate of 200°C/min. The samples were run under vacuum with an external uniaxial pressure of 80 MPa. The pressure was increased from 5 MPa to 80 MPa at the rate of 10 MPa/min.

In another series of experiment, an alumina layer was inserted between the spinel powder and the graphite die to prevent the spark discharge between the die and the spinel particles.

### **4.2.1. Discoloration and transmittance**

Figure 59 presents the photographs of the doped samples compare to the non-doped sample. The first row was the samples SPS without an alumina protective layer, and the

second row was the samples SPS with the alumina protective layer. In the first row, there was a tendency that discoloration increased with the doping amount. However, this problem was solved with the present of the alumina protective layer. Although the morphology of the dopant was unclear when analyzing the TEM image and XRD pattern of the doped powder, the observed discoloration indicated that the dopant stayed at the outermost layer of the spinel particles and was more susceptible to spark discharge than the spinel itself.



Figure 59. Illustration of the transparency of alumina doped samples. From the left: S0A, S1A, S3A, and S5A. The samples on the first row were SPS without the alumina protective layer. The samples on the second row were SPS with the alumina protective layer.

The transmittance of these samples was presented in Figure 60. As could be predicted from their appearance, samples SPS without the alumina protective layer had a lower transmittance over the visible region than the ones SPS with the protective layer. An increase in the dopant amount resulted in a decrease in the transmittance. For samples SPS without the alumina protective layer, their transmittance in the infrared region was hardly

affected by doping. However, in case of samples SPS with the protective layer, except for S1A, there was an absorption band near the  $3\mu\text{m}$  wavelength. This absorption band was also seen on the S10A powder undergone low temperature heat treatments (Figure 55), and was remained unidentified. Since it appeared again with the use of the alumina protective layer, it could be attributed to the Al-O stretching in this particular instance.

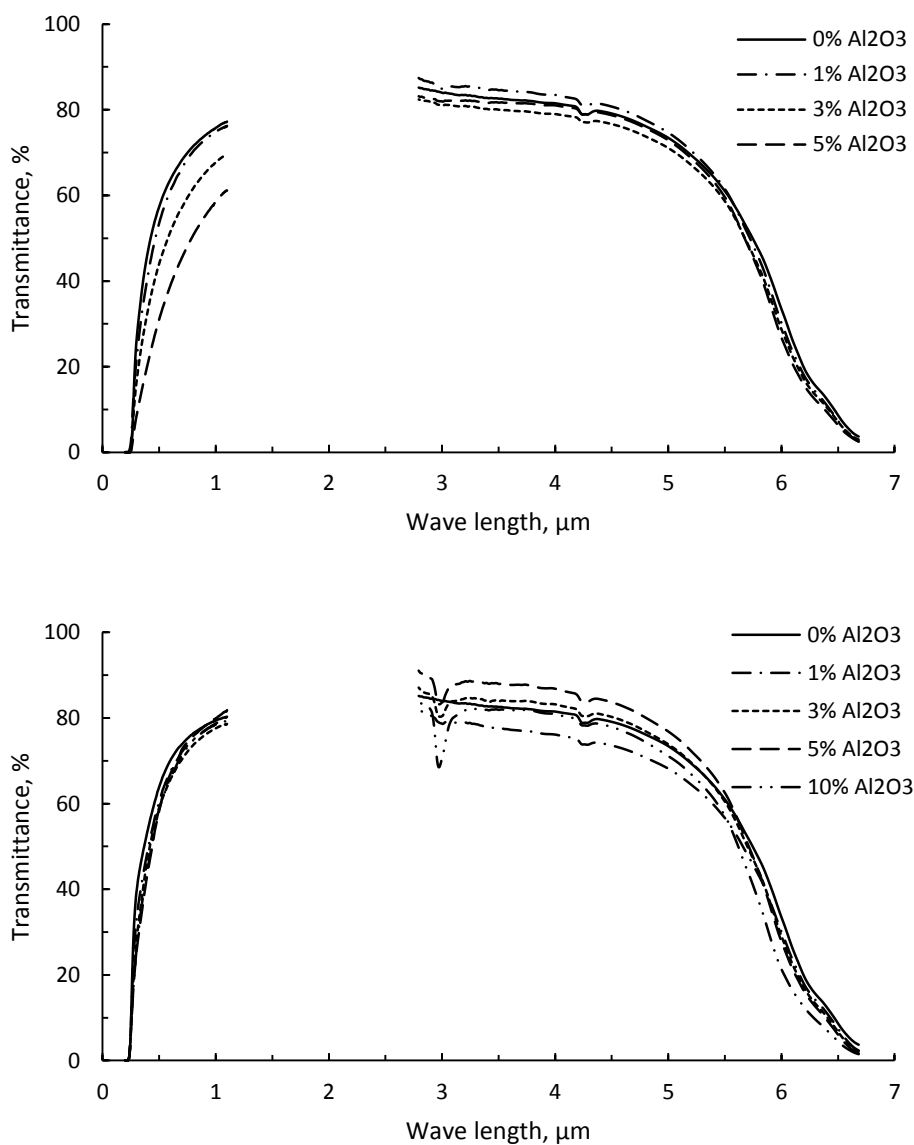


Figure 60. The in-line transmittance of the doped samples. (a) SPS without the alumina layer inserted between spinel powder and the graphite die; (b) SPS with the alumina layer inserted between spinel powder and the graphite die

Because of their discoloration and low transmittance in the visible region, characterization of the samples SPS without the alumina protective layer is terminated at this stage of study. Characterization of the samples SPS with the alumina protective layer continues hereunder.

#### 4.2.2. XRD analysis

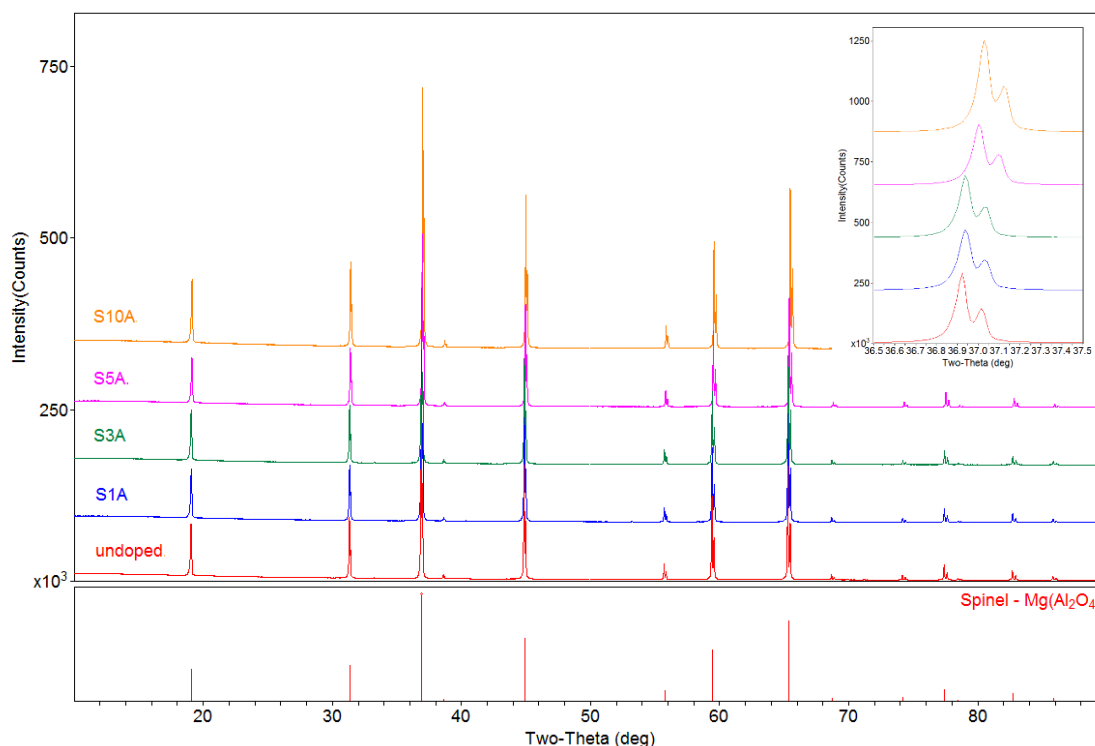


Figure 61. XRD patterns of the doped samples compare to the undoped sample.

As discussed in section 3.4, page 107, the diffraction peaks of the SPS processed sample shifted to the high angle side, i.e. alumina rich side, causing a reduction in the lattice parameter. With the introduction of alumina into the spinel powder, the diffraction peaks would be expected to shift further to the high angle side. Figure 61 compares the XRD pattern of the undoped sample with those of the doped samples. Peak shift of S5A and

S10A was clear, while peak shift of S1A and S3A was negligible. The lattice parameter of S5A was reduced to 8.0488 Å whilst that of S10A was reduced to 8.0440 Å. The changes in the lattice parameter indicated that aluminum ions from the dopant had diffused into the spinel lattice and created an alumina rich solid solution.

#### 4.2.3. Microstructural properties

Figure 62 shows the FESEM images of the doped samples together with an undoped sample, S0A. These samples were dense. No pores present on the polished, uncoated on the cut surface of these samples except for S10A. The average grain sizes of these samples were presented in Table 11. Because S0A was heat treated at 1200°C for an hour before SPS processing, its average grain was about 60% larger than the one SPS without pre-sintering heat treatment.

Table 11. Properties of doped samples.

Sample	T (%) at 550 nm	Grain size (nm)	Density * (g/cm <sup>3</sup> )	Lattice const. (Å)	Hardness ** (HV1)
S0A	62.4	687	3.573	8.0615	1535 ± 11
S1A	64.4	685	3.578	8.0635	1570 ± 7
S3A	62.6	764	3.578	8.0634	1558 ± 11
S5A	63.4	713	3.580	8.0488	1555 ± 12
S10A	62.6	646	3.585	8.0440	1497 ± 35

\* Archimedes density.

\*\* Vickers hardness number with a 1kgf load.

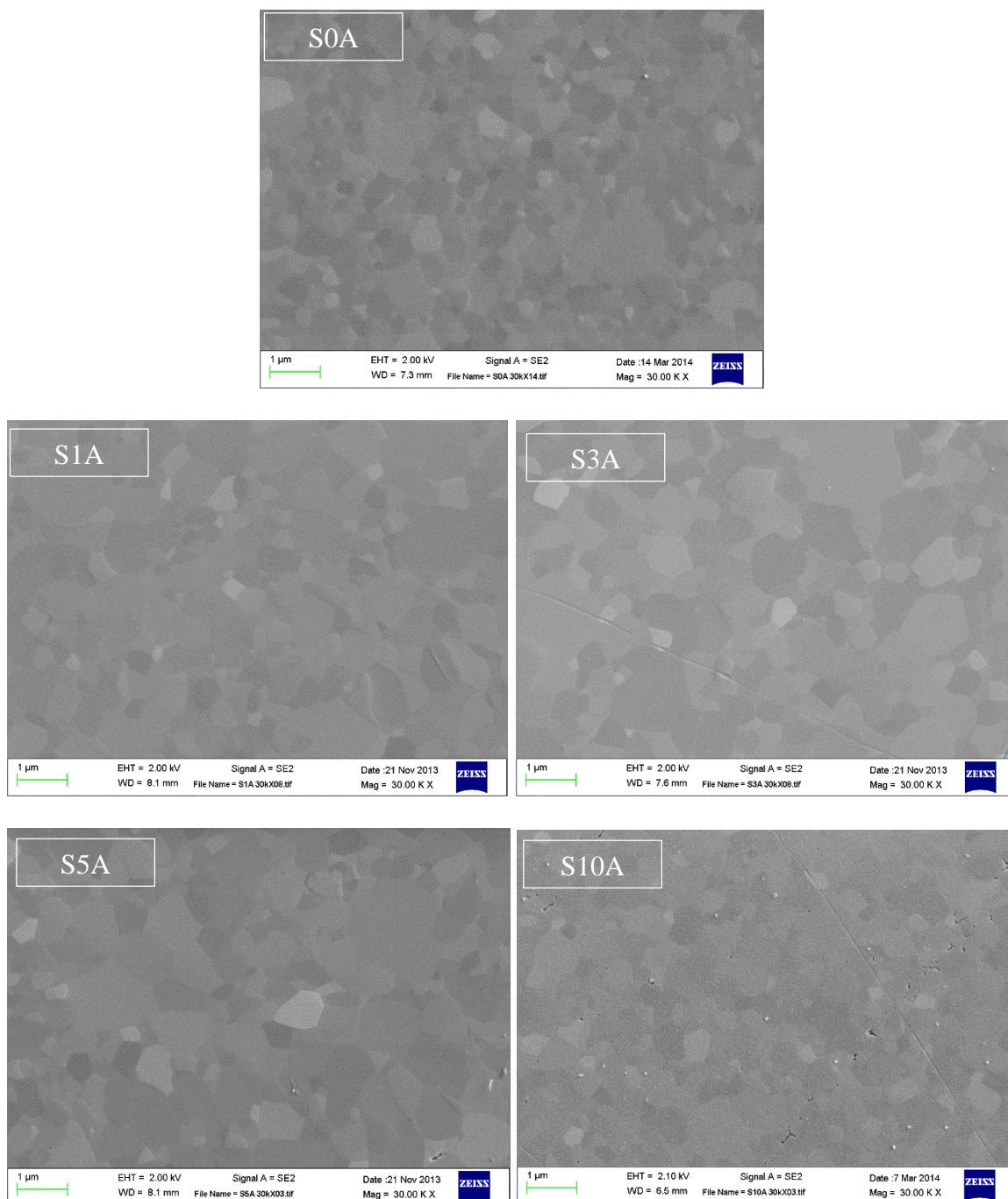


Figure 62. FESEM images of the doped samples.

Figure 63 is the TEM-EDX elemental mapping of samples S10A. No apparent Mg depletion or Al enrichment were observed. This indicated that even there were Al segregation at the grain boundary, the amount is nominal and beyond the detection limit of

the EDX. Therefore, STEM was performed to study the segregation of Al at the grain boundaries.

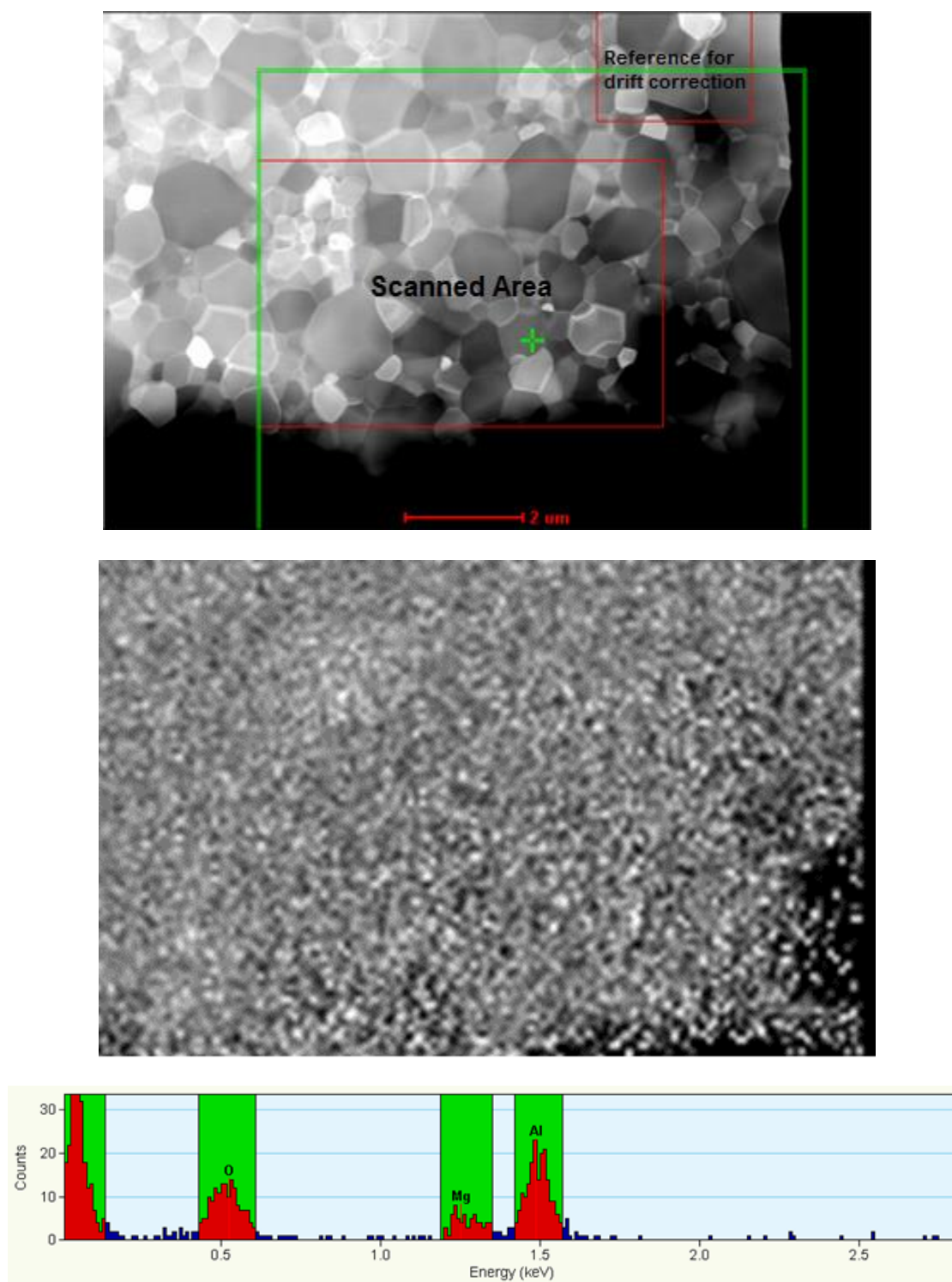


Figure 63. TEM-EDX mapping of S10A.

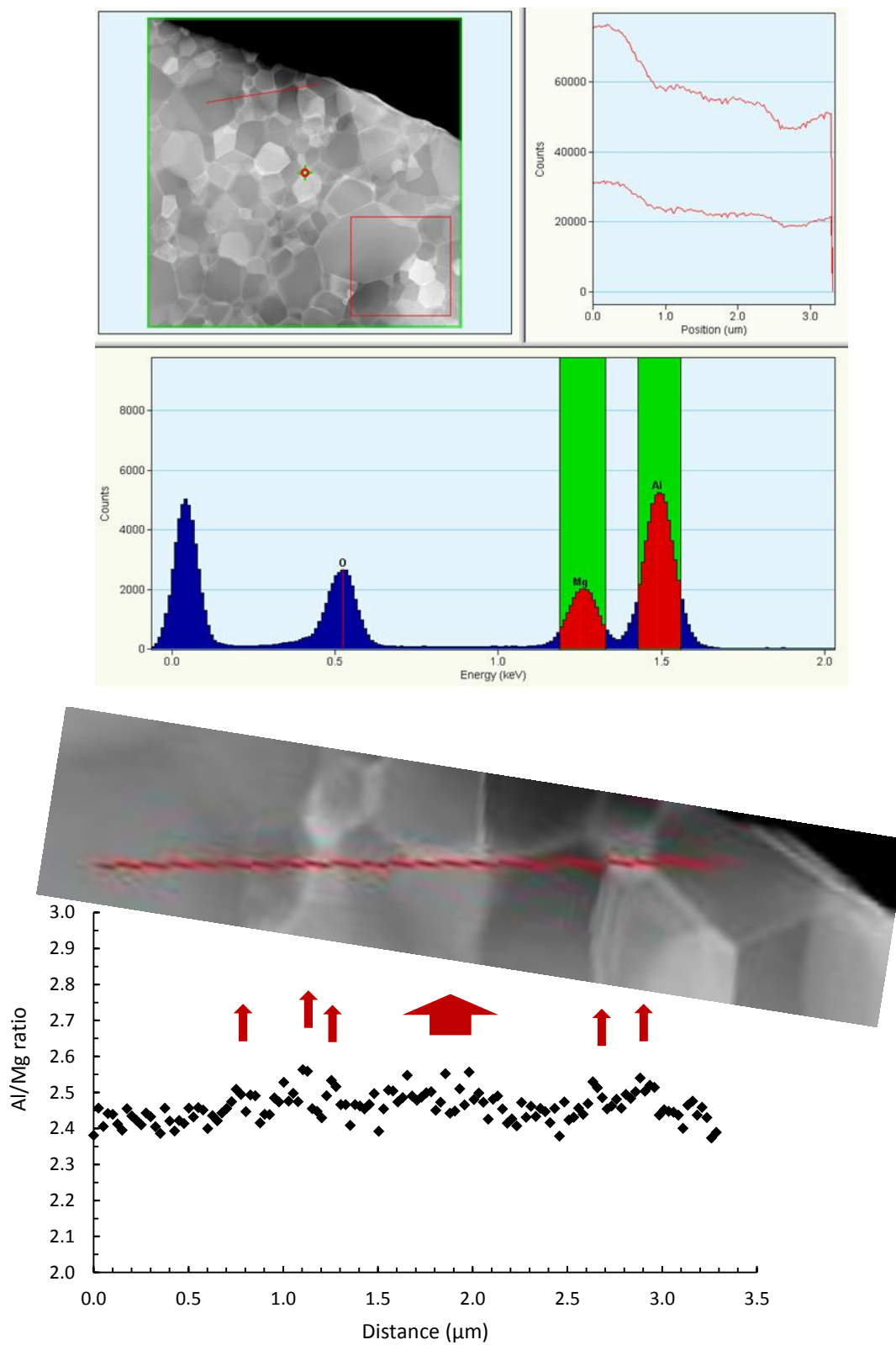


Figure 64. Line-scan STEM analysis of S10A.

Line-scan STEM was performed across a few grain boundaries with a 25 nm step size over a distance of 3.5  $\mu\text{m}$ . The scanned line not only crossed the grain boundaries but also went along a grain boundary. The variation in the counts at the top right corner was caused by the specimen thickness. A method of elemental quantitative analysis of ionic materials from STEM data were developed by Van Capellen and Doukhan<sup>203</sup>. It was derived from the ratio method performed by Cliff and Lorimer<sup>204</sup> such that the relative concentrations of two elements was calculated by the relationship:

$$\frac{I_1}{I_2} = k \frac{C_1}{C_2} \quad \text{Eq. 56}$$

where  $I_1$  and  $I_2$  were the measured characteristic intensities,  $C_1$  and  $C_2$  were the weight fractions of the two elements in question, and  $k$  was a factor which could be determined from the specimen itself or from a thin standard known composition.

In this work, measurement of the foil thickness was not available, thus X-ray intensity ratios is discussed rather than the concentrations. The Al/Mg intensity ratio was plotted as a function of distance in Figure 64. Minor increases in the Al/Mg ratio at the grain boundaries was observed. It indicated that aluminum did segregate at the grain boundary.

#### **4.2.4. Microindentation hardness**

Both Vickers hardness and Knoop hardness indentations were performed on the doped and undoped samples. Vickers hardness was measured with a 1 kgf load while Knoop hardness was measured with different loads, 0.1 kgf, 0.3 kgf, 0.5kgf, and 1 kgf. The Vickers hardness numbers (HV1) were plotted as the function of the dopant amount, and

the Knoop hardness numbers were plotted as a function of the load applied on the indenter in Figure 65.

The Vickers hardness was improved with a small amount of the dopant. HV1 was increased by 2.3% with 1 wt% of alumina doped to the spinel powder but gradually decreased with an increase in the dopant amount. The HV1 of S3A and S5A was about 1.3 – 1.5% higher than S0A, but that S10A was 2.5% lower than S0A. In addition, the margin of error of S10A was twice of that of the other samples. It indicated that S10A was not favorable.

Table 12 shows the hardness of the doped and undoped spinel. For comparison, data collected from the literature were also included. Overall, this work was able to produce spinel with higher hardness values than published in the literature. The hardness HV1 of the material was improved by 2.7 – 6.2% compare to other SPS-processed spinels, and by about 8.5% compare to HIP-processed spinel of the same grain size.

Table 12. Comparison of the obtained hardness with the data available in the literature.

Sources	HV1 (GPa)	HK1 (GPa)	Grain size (nm)	Sintering method
This work:				
S0A	15.1	12.7	687	SPS, 1350°C
S1A	15.4	12.9	685	SPS, 1350°C
S3A	15.3	13.0	764	SPS, 1350°C
S5A	15.3	12.8	713	SPS, 1350°C
S10A	14.7	12.8	646	SPS, 1350°C
References:				
K. Maca <sup>205</sup>	13	-	1000	HIP, 1550°C
A.Krell <sup>17</sup>	14.2	12.6	700	HIP
K.Morita <sup>176</sup>	14.5 - 15	-	400	SPS, 1300°C

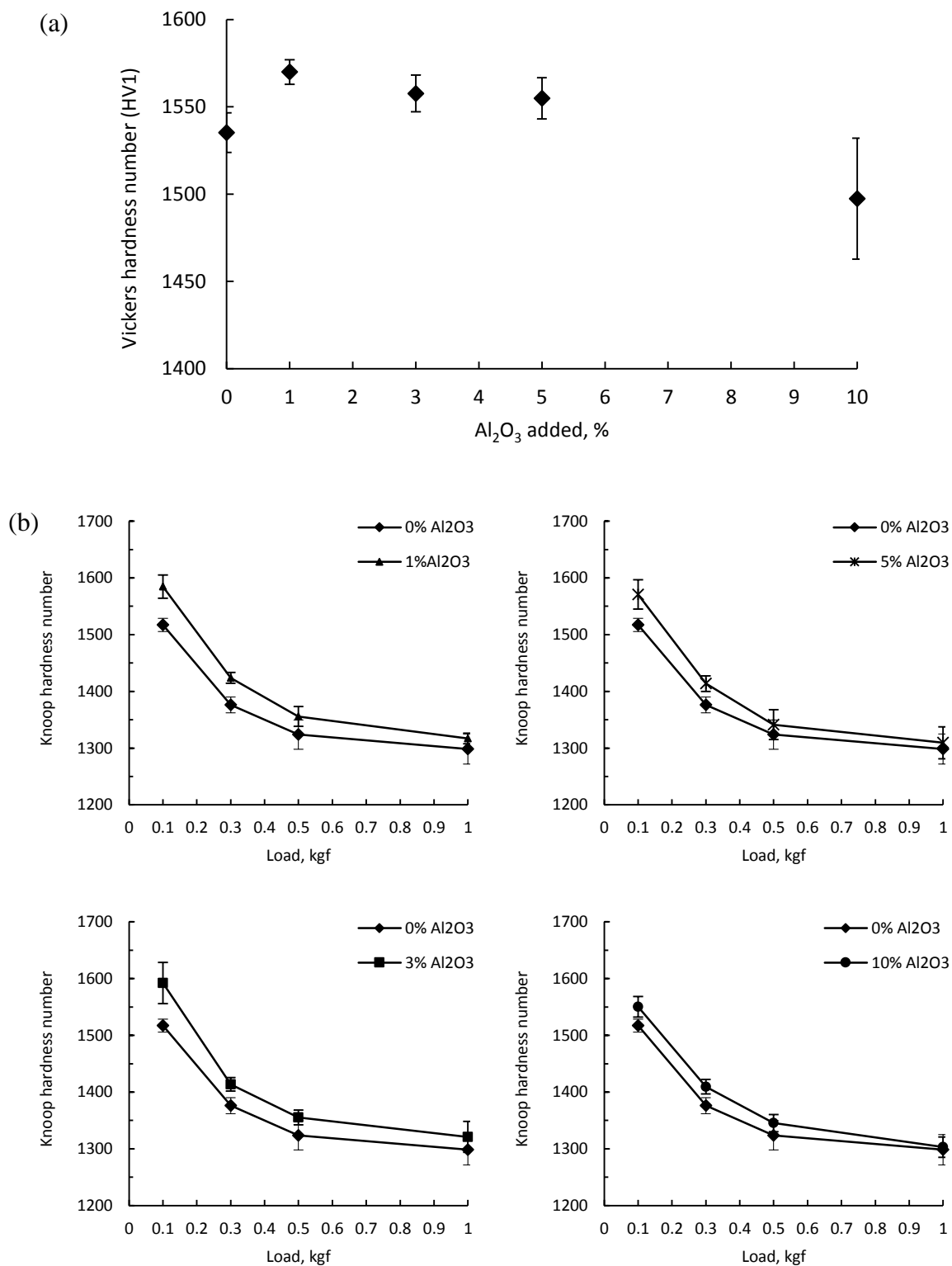


Figure 65. Effects of Al<sub>2</sub>O<sub>3</sub> doping on the hardness of the samples. (a) Vickers hardness and (b) Knoop hardness.

Low load Knoop hardness was improved at all dopant amount. However, HK1 was not increased with 10% of alumina doped to the as received spinel powder. This observation was consistent with HV1. Since the size of a Knoop indent under a 1kgf load was about three time of the size of a Vickers indent under the same load, the margin of error of Knoop hardness measurement was narrower than that of Vickers hardness measurement.

#### 4.2.5. Laser Raman analysis

Study of the Raman scattering and measurement of the elastic properties of doped and undoped samples was carried out before the SPS condition was optimized. The then SPS condition was set up such that the die was heated up to 800°C at the heating rate of 100°C/min, and then to 1300°C or 1550°C at the rate of 5°C/min. After holding at the 1300°C temperature for 50 minutes, or at 1350°C for 40 minutes, the die was cooled down to an annealing temperature in a minute and held for ten minutes before cooled at the rate of 1000°C/min. The annealing temperature was change with the dopant amount as presented in Table 13.

Table 13. The Al<sub>2</sub>O<sub>3</sub> doping amounts, SPS temperatures and annealing temperatures for spinel.

Sample	Al <sub>2</sub> O <sub>3</sub> doping amount (wt%)	SPS temperature (°C)	Annealing temperature (°C)
S0A	0	1300 or 1350	1100
S1A	1	1300 or 1350	1100
S3A	3	1300 or 1350	1150
S5A	5	1300 or 1350	1200

Raman spectroscopic characterization of spinel was performed with the 514.5 nm laser excitation line. Figure 66 and Figure 67 present the Raman spectra of the samples SPS at 1300°C and 1350°C, respectively, and Table 14 presents the Raman symmetric modes of these samples. The spectra of the fabricated samples were generally in a good agreement with that of the natural single crystal except that a minor  $A_{1g}$  peak was observed at 720 – 722  $\text{cm}^{-1}$ . The difference in the vibrations frequencies of the fabricated samples and natural spinel<sup>206</sup> was not significant. However, the symmetry of the fabricated spinel was different from that of the natural spinel because the  $E_{2g}$  peaks at 408 – 409  $\text{cm}^{-1}$  and the  $T_{2g}$  peaks at 666 – 670  $\text{cm}^{-1}$  were not identically symmetric. The normal distribution of these peaks showed that there was probably a peak at 380 – 384  $\text{cm}^{-1}$  and another at 683 – 689  $\text{cm}^{-1}$ . This effect happened regardless of the SPS temperatures.

Table 14. Comparison of the vibrational frequencies of the SPS spinel samples

Samples	Raman symmetric modes*				
	$T_{2g}$	$E_g$	$T_{2g}$	$A_{1g}$	$A_{1g}$
S0A 1300	306	408	666	720	766
S3A 1300	307	409	669	721	768
S5A 1300	308	409	670	722	768
S0A 1350	307	407	666	721	767
S3A 1350	307	409	668	722	768
S5A 1350	307	409	669	721	768
Natural spinel**	312	407	666	-	767

\*Frequency in  $\text{cm}^{-1}$

\*\* From Ref.<sup>206</sup>

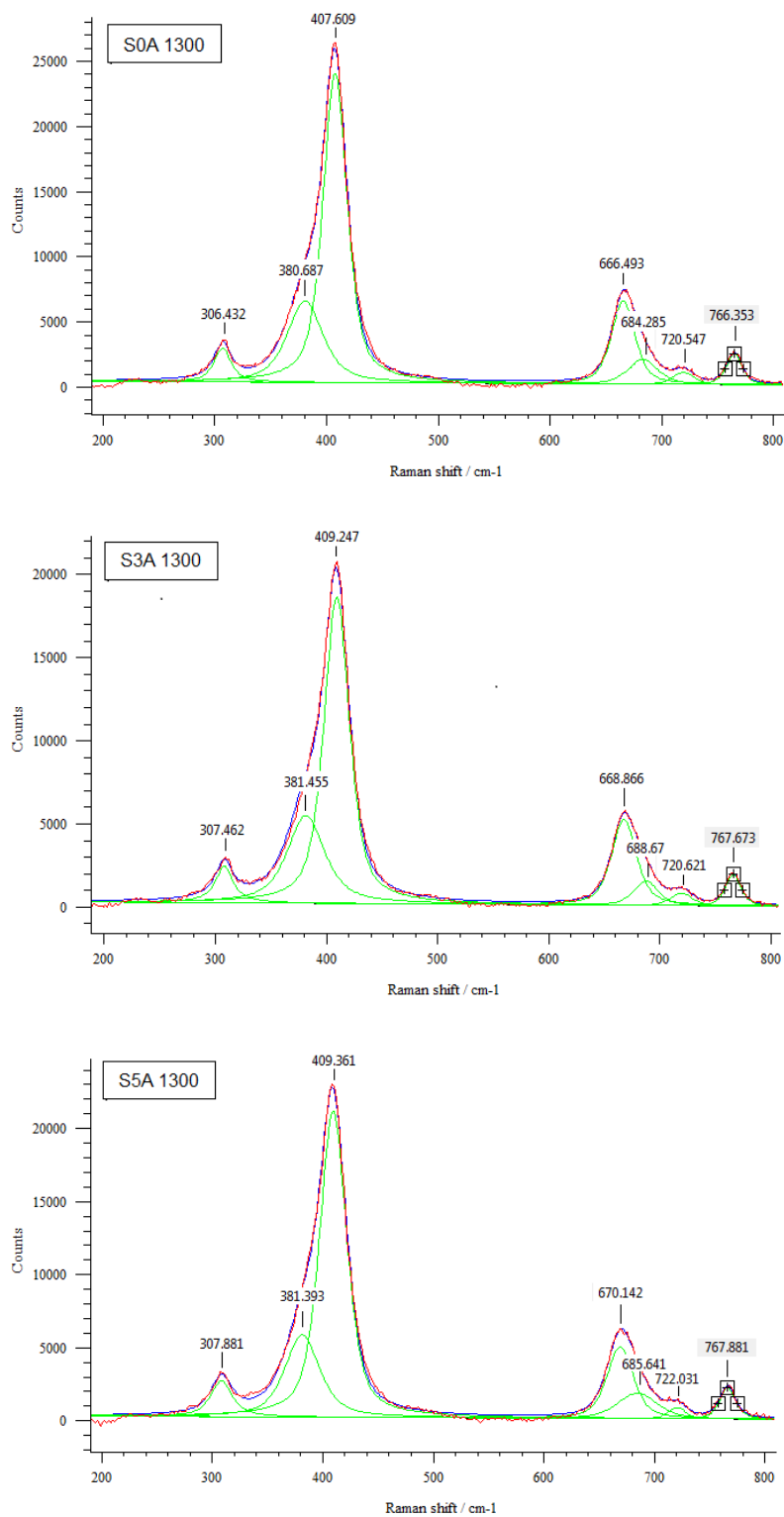


Figure 66. Raman spectra of the samples SPS at 1300°C, taken with a 514 nm laser excitation line.

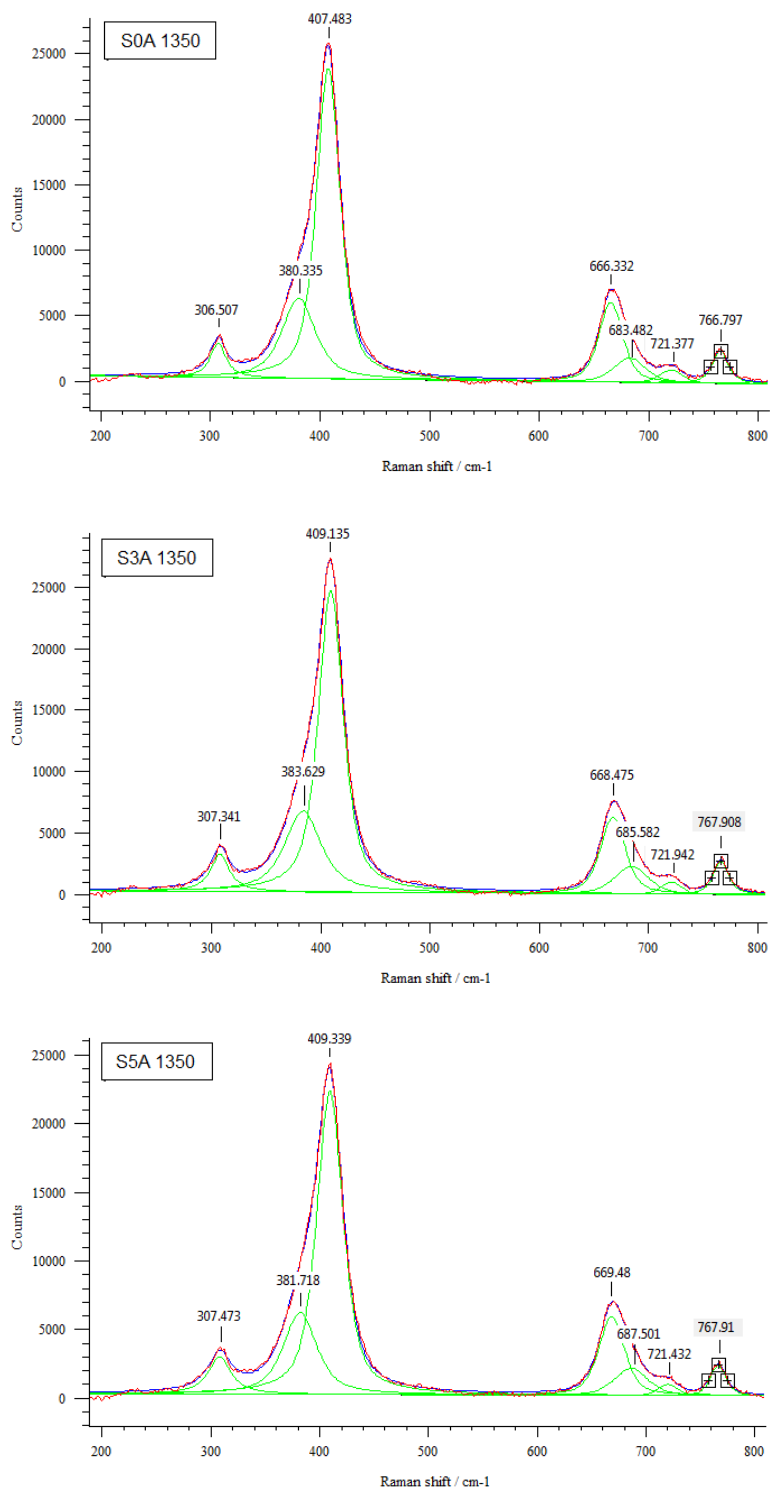


Figure 67. Raman spectra of the samples SPS at 1350°C, taken with a 514 nm laser excitation line.

These observations indicated that the symmetry of SPS processed spinel, dope and undoped, was changed locally and the space group symmetry  $Fd3m$  might not be preserved throughout the bulk of the samples. Together with the shifting of the XRD peaks observed and discussed in the previous section, it was clear that SPS processing created more defects in the spinel lattice structure.

#### 4.2.6. Ultrasound non-destructive evaluation (NDE)

The elastic properties of the fabricated spinel samples were measured on an NED device developed at Rutgers University.

Table 15 presents the A-scan measurement of the Poisson's ratio,  $\nu$ , elastic modulus, Young's modulus and the bulk modulus of the fabricated samples. The samples reached a Young's modulus of 259 – 269 GPa but the difference between samples were not significant.

Table 15. The A-scan measurement of the elastic properties for SPS spinel samples

Samples	cL (m/s) *	cS (m/s)**	$\nu$	E (GPa)	G (GPa)	K (GPa)
S0A 1300	9781	5289	0.293	259	100	209
S0A 1350	9744	5429	0.275	269	106	199
S3A 1300	9800	5370	0.285	265	103	206
S3A 1350	9799	5387	0.283	267	104	205
S5A 1300	9703	5358	0.281	263	103	200
S5A 1350	9802	5401	0.282	268	104	205

\* Longitudinal acoustic wave velocities

\*\* Shear acoustic wave velocities

### 4.3. Summary

The alumina layer inserted between the spinel powder and the graphite die played the role of a barrier that protected the doped spinel from discoloration but generate an anonymous absorption band near the  $3000\text{ cm}^{-1}$  wavenumber.

Coating by surface precipitation was homogeneous and the segregation of alumina at the grain boundary of spinel was nominal even with 10 wt % of alumina added to the spinel. The  $\text{Al}_2\text{O}_3$  dopant diffused into the crystal structure of spinel and form a solid solution that caused a decrease in the lattice parameter and an increase in the density.

Raman symmetric modes were not sensitive to doping. The elastic properties of the dense samples measured by NDE were also not sensitive to doping. However, the hardness of the samples was improved with a small amount of dopant. When the dopant amount was increased to 10 wt%, the hardness was reduced.

## 5. Conclusions

Transparent polycrystalline spinel samples were produced by SPS processing. The transmittance of the samples was heating rate and dwell time dependent. A high heating rate at elevated temperatures resulted in a serious discoloration and pores while a long dwell time diminished the transmittance of the samples.

Discoloration was unavoidable in SPS-processed spinel. It was interpreted as being due to the mobility of the magnesium ions undergoing an electric field at elevated temperature. The magnesium ions left their places in the spinel lattice as the current carriers, creating magnesium vacancies which later played the role of color centers. Discoloration of SPS processed spinel was not associated with new phase formation but a change in the stoichiometry.

The SPS condition for transparent spinel was determined and optimized. The samples were SPS under vacuum with an external uniaxial load of 80MPa. The sintering temperature of spinel in the SPS was 1350°C. The powder could be SPS at the heating rate of 100°C/min until 1100°C, after that the heating rate was reduced to 2.5°C/min. A 10 minute hold at 1350°C was sufficient.

Maintaining a low heating rate above 1100°C was required to keep the electrical power introduced to the SPS system at a low level, otherwise it would promote the mobility of the magnesium ions that lead to a quick formation of the magnesium vacancies. However, the total processing time from 1100°C until cooling should not be longer than 210 minutes because the magnesium ions kept leaving their places in the spinel lattice during thermal-electrical treatment. A long SPS processing time would severely reduce the transmittance of spinel, and would possibly lead to thermal- electrical runaway.

The SPS condition that was described in the literature as the one that obtained a highest transmittance for SPS-processed spinel was rerun. The resulted samples were less transparent than the ones run by the optimized conditions.

HIP post SPS did not cure the discoloration. In addition, it exacerbated unwanted qualities including exaggerated grain growth and inhomogeneity.

A surface precipitation method was developed to coat alumina onto the spinel particles. This method was not only simple but every effective in terms of the uniformity. The segregation of alumina at the grain boundaries of spinel after SPS processing was nominal, even with 10 wt % of alumina added to the spinel. The dopant diffused into the lattice of spinel and form an alumina-rich solid solution that caused a decrease in the lattice parameter and an increase in the density.

The alumina layer inserted between the spinel powder and the graphite die played the role of a barrier that protected the doped spinel from discoloration but generated an anonymous absorption band near the  $3000\text{ cm}^{-1}$  wavenumber.

The elastic properties measured by NDE and Raman symmetric modes were not sensitive to doping. However, the hardness of the samples was improved with a small amount of dopant. The hardness HV1 of the material was improved by 2.7 – 6.2% compare to other SPS-processed spinels, and by about 8.5% compare to HIP-processed spinel of the same grain size. When the dopant amount was increased to 10 wt%, the hardness was reduced.

## 6. Future work

1. Measuring the concentration of magnesium and aluminum near the cathode and anode of the SPS: This dissertation served to develop an improved understanding of the dynamics and interactions of polycrystalline spinel during SPS processing. Discoloration of spinel was interpreted based on the assumption that magnesium ions became mobile when undergoing an electric field at elevated temperatures, and left their places in the spinel lattice, moving toward the SPS cathode as current carriers and creating magnesium vacancies. A large number of samples, doped and undoped, produced by a various SPS conditions were characterized. Although various characterization techniques, including XRD, FESEM, TEM, TEM-EDX, HRTEM, STEM, FTIR, UV-VIS spectroscopy, Laser Raman, NDE, and micro-hardness indentation, were applied, direct evidences of the formation of the magnesium vacancies have not been obtained. Proper qualitative and quantitative measurements of the concentration of magnesium and aluminum near the cathode and anode of the SPS need to be addressed.

2. Detailed modeling and description of the sintering kinetics of spinel in spark plasma sintering: Besides the mobility of the magnesium ion, factors that potentially contribute to the discoloration of spinel include the mobility of the aluminum ion undergoing an electric field, the removal of the oxygen under high vacuum, and the diffusion of carbon from the graphite die into spinel at elevated temperatures. Discussion on the interactions of these element during SPS remains so far at suggestions and assumptions. Because of the present of a DC current and the rise in mobility of cations in spinel, the sintering kinetics of spinel in SPS processing is expected to be different from that in conventional pressure-assisted sintering. In fact, the sintering temperature in the

SPS was lower than in HP and HIP. The processing time in SPS was also shorter. The design of an experimental modeling method to study the interactions of Mg, Al, O and C during SPS processing would be an excellent next step to fully address the discoloration of the samples.

4. Detailed HRTEM analysis of the morphology of the  $\text{Al}_2\text{O}_3$ -coated on the spinel particles: Although the addition of a small amount of alumina helped to improve the hardness of spinel, the morphology of the dopant after heat treatment and before SPS remains unidentified because regular TEM and XRD analysis was not able to determine the morphology of the alumina. Therefore, the kinetics of the solid state sintering of spinel with the present of the alumina was unclear. An HRTEM study looking at the morphology of a material at the atomic scale although time consuming. The final result would be valuable to explain the discoloration of doped samples SPS without the alumina protective layer.

5. Producing large-size samples: Rate controlled SPS developed by this work was capable of producing small grain size high hardness samples. High hardness is advantageous for high-impact resistant applications such as transparent armors because both scratch resistance and ballistic strength can be improved with the hardness. The information and knowledge gained about rate control and properties of the sintered samples are valuable to study at this point, but it would be advantageous to expand this work into a larger system. Larger samples are required for mechanical strength tests, but most importantly they are the transition step for industrial scale production.

## References

- <sup>1</sup>D. C. Harris, "Materials for Infrared Windows and Domes: Properties and Performance," *SPIE Optical Engineering Press* (1999).
- <sup>2</sup>M. Grujicic, W. C. Bell, and B. Pandurangan, "Design and Material Selection Guidelines and Strategies for Transparent Armor Systems," *Materials and Design*, 34, 808-819 (2012).
- <sup>3</sup>J. E. Shelby, "Introduction to Glass Science and Technology, 2nd Edition," 2nd ed. Royal Society of Chemistry, (2005).
- <sup>4</sup>I.-H. Jung, S. Decterov, and A. Pelton, "Critical Thermodynamic Evaluation and Optimization of the MgO-Al<sub>2</sub>O<sub>3</sub>, CaO-MgO-Al<sub>2</sub>O<sub>3</sub>, and MgO-Al<sub>2</sub>O<sub>3</sub>-SiO<sub>2</sub> Systems," *Journal of Phase Equilibria and Diffusion*, 25[4] 329-345 (2004).
- <sup>5</sup>J. K. Burdett, G. D. Price, and S. L. Price, "Role of the Crystal-Field Theory in Determining the Structures of Spinel," *Journal of the American Chemical Society*, 104[1] 92-95 (1982).
- <sup>6</sup>R. J. Hill, J. R. Craig, and G. V. Gibbs, "Systematics of the Spinel Structure Type," *Physics and Chemistry of Minerals*, 4[4] 317-339 (1979).
- <sup>7</sup>A. C. Sutorik, G. Gilde, J. J. Swab, C. Cooper, R. Gamble, and E. Shanholtz, "Transparent Solid Solution Magnesium Aluminate Spinel Polycrystalline Ceramic with the Alumina-Rich Composition MgO.1.2 Al<sub>2</sub>O<sub>3</sub>," *Journal of the American Ceramic Society*, 95[2] 636-643 (2012).
- <sup>8</sup>T. E. Mitchell, "Dislocations and Mechanical Properties of MgO-Al<sub>2</sub>O<sub>3</sub> Spinel Single Crystals," *Journal of the American Ceramic Society*, 82[12] 3305-3316 (1999).
- <sup>9</sup>A. Gatti, "Development of a Process for Producing Transparent Spinel Bodies." in. General Electric Company, Space Division, Space Science Laboratory, Philadelphia, PA, Contract N00019-69-C-0133, Code Air-5203A, 1969.
- <sup>10</sup>H. Palmour, "Development of Polycrystalline Spinel for Transparent Armor Applications," *Final Technical Report, Army Materials and Mechanics Research Center, Massachusetts* (1972).
- <sup>11</sup>M. C. L. Patterson, J. Caiazzaa, and D. Roy, "Transparent Spinel Development," *Proceedings of SPIE*, 4102, 59-68 (2000).
- <sup>12</sup>M. Shimada, T. S. T. Endo, and T. Sato, "Fabrication of Transparent Spinel Polycrystalline Materials," *Materials Letters*, 28[4-6] 413-415 (1996).

- <sup>13</sup>A. Krell, T. Hutzler, J. Klimke, and A. Potthoff, "Fine-Grained Transparent Spinel Windows by the Processing of Different Nanopowders," *Journal of the American Ceramic Society*, 93[9] 2656-2666 (2010).
- <sup>14</sup>I. E. Reimanis, K. Rozenburg, H. J. Kleebe, and R. L. Cook, "Fabrication of transparent spinel- The role of impurities," pp. 48-55. in Proceedings of SPIE, Vol. 5786. 2005.
- <sup>15</sup>G. Gilde, P. Patel, P. Patterson, D. Blodgett, D. Duncan, and D. Hahn, "Evaluation of Hot Pressing and Hot Isostatic Pressing Parameters on the Optical Properties of Spinel," *Journal of the American Ceramic Society*, 88[10] 2747-2751 (2005).
- <sup>16</sup>N. Petch, "The cleavage strength of polycrystals," *Journal of the Iron and Steel Institute*, 174, 25-28 (1953).
- <sup>17</sup>A. Krell and A. Bales, "Grain Size-Dependent Hardness of Transparent Magnesium Aluminate Spinel," *International Journal of Applied Ceramic Technology*, 8[5] 1108-1114 (2011).
- <sup>18</sup>R. W. Rice, C. C. Wu, and F. Boichelt, "Hardness–Grain Size Relations in Ceramics," *Journal of the American Ceramic Society*, 77[10] 2539-2553 (1994).
- <sup>19</sup>C. Wang and Z. Zhao, "Transparent MgAl<sub>2</sub>O<sub>4</sub> Ceramic Produced by Spark Plasma Sintering," *Scripta Materialia*, 61[2] 193-196 (2009).
- <sup>20</sup>I. Reimanis and H.-J. Kleebe, "A Review on the Sintering and Microstructure Development of Transparent Spinel (MgAl<sub>2</sub>O<sub>4</sub>)," *Journal of the American Ceramic Society*, 92[7] 1472-1480 (2009).
- <sup>21</sup>K. Morita, B.-N. Kim, H. Yoshida, and K. Hiraga, "Densification behavior of a fine-grained MgAl<sub>2</sub>O<sub>4</sub> spinel during spark plasma sintering (SPS)," *Scripta Materialia*, 63[6] 565-568 (2010).
- <sup>22</sup>K. Morita, B.-N. Kim, H. Yoshida, and K. Hiraga, "Spark-Plasma-Sintering Condition Optimization for Producing Transparent MgAl<sub>2</sub>O<sub>4</sub> Spinel Polycrystal," *Journal of the American Ceramic Society*, 92[6] 1208-1216 (2009).
- <sup>23</sup>S. Meir, S. Kalabukhov, N. Froumin, M. P. Dariel, and N. Frage, "Synthesis and Densification of Transparent Magnesium Aluminate Spinel by SPS Processing," *Journal of the American Ceramic Society*, 92[2] 358-364 (2009).
- <sup>24</sup>B.-N. Kim, K. Morita, J.-H. Lim, K. Hiraga, and H. Yoshida, "Effects of Preheating of Powder Before Spark Plasma Sintering of Transparent MgAl<sub>2</sub>O<sub>4</sub> Spinel," *Journal of the American Ceramic Society*, 93[8] 2158-2160 (2010).
- <sup>25</sup>N. Frage, S. Cohen, S. Meir, S. Kalabukhov, and M. Dariel, "Spark Plasma Sintering (SPS) of Transparent Magnesium–Aluminate Spinel," *Journal of Materials Science*, 42[9] 3273-3275 (2007).

- <sup>26</sup>G. Bernard-Granger, N. Benameur, C. Guizard, and M. Nygren, "Influence of Graphite Contamination on the Optical Properties of Transparent Spinel Obtained by Spark Plasma Sintering," *Scripta Materialia*, 60[3] 164-167 (2009).
- <sup>27</sup>K. Morita, B.-N. Kim, K. Hiraga, and H. Yoshida, "Fabrication of high-strength transparent  $\text{MgAl}_2\text{O}_4$  spinel polycrystals by optimizing spark-plasma-sintering conditions," *Journal of Materials Research*, 24[9] 2863-2872 (2009).
- <sup>28</sup>G. Bonnefont, S. T. G. Fantozzi, and L. Bonneau, "Fine-Grained Transparent  $\text{MgAl}_2\text{O}_4$  Spinel Obtained by Spark Plasma Sintering of Commercially Available Nanopowders," *Ceramics International*, 38[1] 131-140 (2012).
- <sup>29</sup>K. Rozenburg, I. E. Reimanis, H. J. Kleebe, and R. L. Cook, "Sintering kinetics of a  $\text{MgAl}_2\text{O}_4$  spinel doped with LiF," *Journal of the American Ceramic Society*, 91[2] 444-450 (2008).
- <sup>30</sup>G. R. Villalobos, J. S. Sanghera, and I. D. Aggarwal, "Degradation of Magnesium Aluminum Spinel by Lithium Fluoride Sintering Aid," *Journal of the American Ceramic Society*, 88[5] 1321-1322 (2005).
- <sup>31</sup>D. Lepkova, A. Baatarjav, and L. Pavlova, "Effect of Additives on the Firing and the Properties of Magnesium Spinel Ceramics," *Interceram*, 42[2] 89-92 (1993).
- <sup>32</sup>R. Bratton, "Translucent Sintered  $\text{MgAl}_2\text{O}_4$ ," *Journal of the American Ceramic Society*, 57[7] 283-286 (1974).
- <sup>33</sup>O. Borrero-López, A. L. Ortiz, A. D. Gledhill, F. Guiberteau, T. Mroz, L. M. Goldman, and N. P. Padture, "Microstructural Effects on the Sliding Wear of Transparent Magnesium-Aluminate Spinel," *Journal of the European Ceramic Society*, 32[12] 3143-3149 (2012).
- <sup>34</sup>H. Tripathi, S. Singla, and A. Ghosh, "Synthesis and densification behaviour of magnesium aluminate spinel: Effect of  $\text{Dy}_2\text{O}_3$ ," *Ceramics International*, 35[6] 2541-2544 (2009).
- <sup>35</sup>T. F. Baranova, I. N. Kurskaya, N. A. Dabizha, Y. B. Petrov, and E. S. Lukin, "Sintering High-Purity Fusions of MgO and  $\text{MgO} \cdot \text{Al}_2\text{O}_3$ ," *Refractories and Industrial Ceramics*, 22[3-4] 180-182 (1981).
- <sup>36</sup>M. Stuer, Z. Zhao, U. Aschauer, and P. Bowen, "Transparent Polycrystalline Alumina Using Spark Plasma Sintering: Effect of Mg, Y and La Doping," *Journal of the European Ceramic Society*, 30[6] 1335-1343 (2010).
- <sup>37</sup>T. Mroz, L. M. Goldman, A. D. Gledhill, D. Li, and N. P. Padture, "Nanostructured, Infrared-Transparent Magnesium-Aluminate Spinel with Superior Mechanical Properties," *International Journal of Applied Ceramic Technology*, 9[1] 83-90 (2012).

- <sup>38</sup>M. F. Zawrah, H. Hamaad, and S. Meky, "Synthesis and characterization of nano MgAl<sub>2</sub>O<sub>4</sub> spinel by the co-precipitated method," *Ceramics International*, 33[6] 969-978 (2007).
- <sup>39</sup>J. W. Anthony, R. A. Bideaux, K. W. Bladh, and M. C. Nichols, "Handbook of Mineralogy, Volume III: Halides, Hydroxides, Oxides," *Arizona: Mineral Data Publishing* (1997).
- <sup>40</sup>R. Gerber, "Apokalyptische Steine nach Plinius und heute." Books on Demand GmbH, (2002).
- <sup>41</sup>A. Malsy and L. Klemm, "Distinction of gem spinels from the Himalayan mountain belt," *CHIMIA International Journal for Chemistry*, 64[10] 741-746 (2010).
- <sup>42</sup>L. Grande and A. Augustyn, "Gems and Gemstones: Timeless Natural Beauty of the Mineral World ". University Of Chicago Press, (2009).
- <sup>43</sup>H. L. Chhibber, "The Mineral Resources of Burma." Macmillan and Co., Limited: London, (1934).
- <sup>44</sup>K. Nassau, "Gems Made by Man." Chilton Book Co., (1980).
- <sup>45</sup>N. W. Grimes, "The Spinel: Versatile Materials," *Physics in Technology*, 6[1] 22-27 (1975).
- <sup>46</sup>W. H. Bragg, "The Structure of the Spinel Group of Crystals," *Philosophical Magazine*, 30[176] 305 - 315 (1915).
- <sup>47</sup>S. Nishikawa, "Structure of Some Crystals of The Spinel Group," *Proc. Math. Phys. Soc. Tokyo*, 8, 199-209 (1915).
- <sup>48</sup>R. A. Binns, R. J. Davis, and S. J. B. Reed, "Ringwoodite, Natural (Mg,Fe)<sub>2</sub>SiO<sub>4</sub> Spinel in the Tenham Meteorite," *Nature*, 221[5184] 943-944 (1969).
- <sup>49</sup>L. Reznitsky, E. Sklyarov, Z. Ushchapovskaya, L. Suvorova, Y. Polekhovsky, P. Dzerzanovsky, and I. Barash, "Cuprokalininite, CuCr<sub>2</sub>S<sub>4</sub>, a new sulfospinel from metamorphic rocks of the Sludyanka Complex, South Baikal region," *Geology of Ore Deposits*, 53[8] 758-766 (2011).
- <sup>50</sup>F. J. Tone, "Artificial Magnesia Spinel and Process of Manufacture," *US Patent*, No. 1448010 (1923).
- <sup>51</sup>R. Rieke and K. Blicke, "Development, Properties, and Technical Use of Some Spinel," *Ber. deut. keram. Ges.*, 12[4] 163 (1931).
- <sup>52</sup>E. Kothny, "Refractory Materials for the Electric Steel Furnace," *Feuerfest*, 3[10] 157-164 (1927).

- <sup>53</sup>R. Purdy, "Ceramic Abstracts Vol. 7 No. 5," *Journal of the American Ceramic Society*, 11[5] 267-333 (1928).
- <sup>54</sup>J. A. Cunliffe and H. E. Clem, "Refractories for Use in Sulphate-Recovery Furnaces of the Pulp and Paper Industries," *Journal of the American Ceramic Society*, 15[6] 321-321 (1932).
- <sup>55</sup>J. Knoliman, "Refractories for Oil-Gas Manufacture," *Journal of the American Ceramic Society*, 9[12] 860-887 (1926).
- <sup>56</sup>C. Parmelee and K. Lyon, "Investigation of the Use of Magnesium Aluminate (Spinel) as a Material for Glassmelting Containers," *Journal of the American Ceramic Society*, 18[1-12] 338-340 (1935).
- <sup>57</sup>R. Dal Maschio, B. Fabbri, and C. Fiori, "Industrial Applications of Refractories Containing Magnesium Aluminate Spinel," *Industrial Ceramics*, 8[3] 121-126 (1988).
- <sup>58</sup>D. J. Bray, "Toxicity of Chromium Compounds Formed in Refractories," *American Ceramic Society Bulletin*, 64[7] 1012-1016 (1985).
- <sup>59</sup>H. Komatsu, M. Arai, and S. Ukawa, "Current and Future Status of Chrome-Free Bricks for Rotary Cement Kilns," *Taikabutsu Overseas*, 19[4] 3-9 (1999).
- <sup>60</sup>J. Barnhart, "Chromium Chemistry and Implications for Environmental Fate and Toxicity," *Soil and Sediment Contamination*, 6[6] 561-568 (1997).
- <sup>61</sup>D. W. Roy, "Spinel: Where Did It Go?," pp. 307-316 in *Optical Science, Engineering and Instrumentation'97*.
- <sup>62</sup>D. C. Harris, "History of Development of Polycrystalline Optical Spinel in the U.S.," pp. 1-22 in *Defense and Security*.
- <sup>63</sup>K. Morita, B.-N. Kim, H. Yoshida, H. Zhang, K. Hiraga, and Y. Sakka, "Effect of Loading Schedule on Densification of  $MgAl_2O_4$  Spinel during Spark Plasma Sintering (SPS) Processing," *Journal of the European Ceramic Society*, 32[10] 2303-2309 (2012).
- <sup>64</sup>G. Delaizir, M. Dollé, P. Rozier, and X. H. Zhang, "Spark Plasma Sintering: An Easy Way to Make Infrared Transparent Glass-Ceramics," *Journal of the American Ceramic Society*, 93[9] 2495-2498 (2010).
- <sup>65</sup>J. Chesters and C. Parmelee, "Reaction - Expansion Measurements on Chromite and Allied Spinels," *Journal of the American Ceramic Society*, 18[1-12] 94-100 (1935).
- <sup>66</sup>B. Hallstedt, "Thermodynamic Assessment of the System  $MgO-Al_2O_3$ ," *Journal of the American Ceramic Society*, 75[6] 1497-1507 (1992).

- <sup>67</sup>K. D. Rouse, M. W. Thomas, and B. T. M. Willis, "Space group of the spinel structure: A neutron diffraction study of  $\text{MgAl}_2\text{O}_4$ ," *Journal of Physics C: Solid State Physics* 9[9] L231-L233 (1976).
- <sup>68</sup>L. W. Finger, R. M. Hazen, and A. M. Hofmeister, "High-Pressure Crystal Chemistry of Spinel ( $\text{MgAl}_2\text{O}_4$ ) and Magnetite ( $\text{Fe}_3\text{O}_4$ ): Comparisons with Silicate Spinel," *Physics and Chemistry of Minerals*, 13[4] 215-220 (1986).
- <sup>69</sup>T. F. W. Barth and E. Posnjak, "The Spinel Structures: An Example of Variate Atom Equipoints," *Journal of the Washington Academy of Sciences*, 21[12] 255-258 (1931).
- <sup>70</sup>F. A. Kröger and H. J. Vink, "Relations Between the Concentrations of Imperfections in Crystalline Solids," *Solid state physics*, 3 307-435 (1956).
- <sup>71</sup>S. T. Murphy, C. A. Gilbert, R. Smith, T. E. Mitchell, and R. W. Grimes, "Non-stoichiometry in  $\text{MgAl}_2\text{O}_4$  spinel," *Philosophical Magazine*, 90[10] 1297-1305 (2010).
- <sup>72</sup>M. L. Bortz, R. H. French, D. J. Jones, R. V. Kasowski, and F. S. Ohuchi, "Temperature Dependence of the Electronic Structure of Oxides:  $\text{MgO}$ ,  $\text{MgAl}_2\text{O}_4$  and  $\text{Al}_2\text{O}_3$ ," *Phys. Scr.*, 41[4] 537-541 (1990).
- <sup>73</sup>R. Khenata, M. Sahnoun, H. Baltache, M. Rérat, A. H. Reshak, Y. Al-Douri, and B. Bouhafs, "Full-Potential Calculations of Structural, Elastic and Electronic Properties of  $\text{MgAl}_2\text{O}_4$  and  $\text{ZnAl}_2\text{O}_4$  Compounds," *Physics Letters A*, 344[2-4] 271-279 (2005).
- <sup>74</sup>S. K. Sampath, D. G. Kanhere, and R. Pandey, "Electronic structure of spinel oxides: zinc aluminate and zinc gallate," *Journal of Physics: Condensed Matter*, 11[18] 3635 (1999).
- <sup>75</sup>Y.-N. Xu and W. Y. Ching, "Self-consistent band structures, charge distributions, and optical-absorption spectra in  $\text{MgO}$ ,  $\alpha\text{-Al}_2\text{O}_3$ , and  $\text{MgAl}_2\text{O}_4$ ," *Physical Review B*, 43[5] 4461-4472 (1991).
- <sup>76</sup>S. M. Hosseini, "Structural, Electronic and Optical Properties of Spinel  $\text{MgAl}_2\text{O}_4$  Oxide," *Physica Status Solidi (B)*, 245[12] 2800-2807 (2008).
- <sup>77</sup>S. E. Braslavsky, "Glossary of Terms Used in Photochemistry," *Pure and Applied Chemistry*, 79[3] 293-465 (2007).
- <sup>78</sup>D. W. Blodgett, D. V. Hahn, and M. E. Thomas, "Optical Characterization of AION and Spinel," *Proceedings of SPIE* 5786, 83-94 (2005).
- <sup>79</sup>E. D. Palik, "Handbook of Optical Constants of Solids II." Academic Press: San Diego, (1991).
- <sup>80</sup>E. E. Wahlstrom, "Optical Crystallography " 4th ed. John Wiley & Sons Inc.: New York, (1969).

- <sup>81</sup>J. Schroeder and J. H. Rosolowski, "Light Scattering in Polycrystalline Materials," pp. 156-168 in 25th Annual Technical Symposium.
- <sup>82</sup>J. Peelen and R. Metselaar, "Light scattering by pores in polycrystalline materials: Transmission properties of alumina," *Journal of Applied Physics*, 45[1] 216-220 (1974).
- <sup>83</sup>A. Krell, K. Waetzig, and J. Klimke, "Effects and Elimination of Nanoporosity in Transparent Sintered Spinel ( $\text{MgAl}_2\text{O}_4$ )," *Proceeding of SPIE*, 8016, 801602-801601 - 801602-801610 (2011).
- <sup>84</sup>A. Dericoglu and Y. Kagawa, "Effect of Grain Boundary Microcracking on the Light Transmittance of Sintered Transparent  $\text{MgAl}_2\text{O}_4$ ," *Journal of the European Ceramic Society*, 23[6] 951-959 (2003).
- <sup>85</sup>I. Reimanis, H. Kleebe, R. Cook, and A. DiGiovanni, "Transparent spinel fabricated from novel powders: synthesis, microstructure and optical properties." in DTIC Document, 2004.
- <sup>86</sup>M. Patterson, G. A. Gilde, and D. W. Roy, "Fabrication of large thick panels of transparent spinel," *Proceedings of SPIE*, 4452, 126-132 (2001).
- <sup>87</sup>N. A. Ashby, "The Factor of Hardness in Metals," *New Zealand Engineering*, 6[1] 33-34 (1951).
- <sup>88</sup>R. W. Rice, "Microstructure Dependence of Mechanical Behavior of Ceramics" pp. 199-381. in *Treatise on Materials Science and Technology*, Vol. Vol. 11: Properties and Microstructure. Edited by R. K. MacCrone. Academic Press, Inc., New York, 1977.
- <sup>89</sup>Y. Akimune and R. C. Bradt, "Knoop Microhardness Anisotropy of Single-Crystal Stoichiometric  $\text{MgAl}_2\text{O}_4$  Spinel," *Journal of the American Ceramic Society*, 70[4] C-84-C-86 (1987).
- <sup>90</sup>E. R. Petty, "The hardness anisotropy of aluminum single crystals," *Journal Institute of Metals*, 91, 54-62 (1962).
- <sup>91</sup>P. G. Riewald and L. H. Van Vlack, "Slip Behavior and Hardness Indentations in MnSe and MnSe-MnS Solid Solutions," *Journal of the American Ceramic Society*, 52[7] 370-375 (1969).
- <sup>92</sup>C. A. Brookes, "Plastic Deformation and Anisotropy in the Hardness of Diamond," *Nature*, 228[41] 660-661 (1970).
- <sup>93</sup>J. Hornstra, "Dislocations, Stacking Faults and Twins in the Spinel Structure," *Journal of Physics and Chemistry of Solids*, 15[3-4] 311-323 (1960).
- <sup>94</sup>L. Hwang, A. Heuer, and T. Mitchell, "Slip Systems in Stoichiometric  $\text{MgAl}_2\text{O}_4$  Spinel," *Deformation of Ceramics* 257-270 (1975).

- <sup>95</sup>K. C. Radford and C. W. A. Newey, "Plastic deformation in magnesium aluminate spinel," *Proc. Br. Ceram. Soc.*, 9, 131-145 (1967).
- <sup>96</sup>R. Duclos, N. Doukhan, and B. Escaig, "High Temperature Creep Behaviour of Nearly Stoichiometric Alumina Spinel," *Journal of Materials Science*, 13[8] 1740-1748 (1978).
- <sup>97</sup>T. Yano, M. Ikari, T. Iseki, E. H. Farnum, F. W. Clinard, and T. E. Mitchell, "Effect of Neutron Irradiation on Knoop Microhardness Anisotropy in  $\text{MgO}\cdot 3\text{Al}_2\text{O}_3$  Single Crystals," *Journal of the American Ceramic Society*, 78[6] 1469-1474 (1995).
- <sup>98</sup>C. A. Brookes, J. B. O'Neill, and B. A. W. Redfern, "Anisotropy in the Hardness of Single Crystals," *Proceedings of the Royal Society of London. Series A, Mathematical and Physical Sciences*, 322[1548] 73-88 (1971).
- <sup>99</sup>M. Takacs and B. Vero, "Material structural aspects of micro-scale chip removal," *Materials Science Forum*, 414, 337-342 (2003).
- <sup>100</sup>E. O. Hall, "The Deformation and Ageing of Mild Steel: III Discussion of Results," *Proceedings of the Physical Society. Section B*, 64[9] 747-753 (1951).
- <sup>101</sup>P. J. Patel, J. J. Swab, M. Staley, and G. D. Quinn, "Indentation Size Effect (ISE) of Transparent AION and  $\text{MgAl}_2\text{O}_4$ ," (No. ARL-TR-3852). ARMY RESEARCH LAB ABERDEEN PROVING GROUND MD (2006).
- <sup>102</sup>R. A. Weeks and E. Sonder, "Electrical Conductivity of Pure and Fe-Doped Magnesium-Aluminum Spinel," *Journal of the American Ceramic Society*, 63[1-2] 92-95 (1980).
- <sup>103</sup>E. Sonder and L. Darken, "The Influence of Cation Stoichiometry on the Electrical Conductivity and High-Temperature Stability of  $\text{MgO}\cdot n\text{Al}_2\text{O}_3$  Spinel," in MRS Proceedings. Vol. 24.
- <sup>104</sup>E. Sonder, "Ionic Transference Numbers and Electrical Conduction in  $\text{MgAl}_2\text{O}_4$  Spinel," *Journal of the American Ceramic Society*, 66[1] 50-53 (1983).
- <sup>105</sup>J. L. Bates and J. E. Gamier, "Electrical Conductivity of  $\text{MgAl}_2\text{O}_4$  and  $\text{Y}_3\text{Al}_5\text{O}_{12}$ ," *Journal of the American Ceramic Society*, 64[10] C-138-C-141 (1981).
- <sup>106</sup>J. Martinelli, E. Sonder, R. Weeks, and R. Zuhr, "Mobility of Cations in Magnesium Aluminate Spinel," *Physical Review B*, 33[8] 5698 (1986).
- <sup>107</sup>E. Sonder and R. A. Weeks, "Behavior of Electrical Conduction of Spinel and Other Insulating Oxides in Moderate Electric Fields at High Temperature," *Journal of Applied Physics*, 56[8] 2365-2366 (1984).
- <sup>108</sup>M. N. Rahaman, "Ceramic Processing and Sintering," pp. 875 2nd ed. CRC Press: New York, (2003).

- <sup>109</sup>A. Beltrán, J. A. Igualada, R. Llusar, and J. Andrés, "MgAl<sub>2</sub>O<sub>4</sub> Spinel Crystal Structure. An Ab Initio Perturbed Ion Study," *International Journal of Quantum Chemistry*, 56[S29] 685-694 (1995).
- <sup>110</sup>C. Wang, "Growth and characterization of spinel single crystals for substrate use in integrated electronics," *Journal of Applied Physics*, 40[9] 3433-3444 (1969).
- <sup>111</sup>D. Viechnicki, F. Schmid, and J. McCauley, "Growth of nearly stoichiometric MgAl<sub>2</sub>O<sub>4</sub> spinel single crystals by a gradient furnace technique," *Journal of Applied Physics*, 43[11] 4508-4512 (1972).
- <sup>112</sup>C.-T. Wang, L.-S. Lin, and S.-J. Yang, "Preparation of MgAl<sub>2</sub>O<sub>4</sub> Spinel Powders via Freeze-Drying of Alkoxide Precursors," *Journal of the American Ceramic Society*, 75[8] 2240-2243 (1992).
- <sup>113</sup>R. Cook, M. Kochis, I. Reimanis, and H.-J. Kleebe, "A New Powder Production Route for Transparent Spinel Windows: Powder Synthesis and Window Properties," *Defense and Security*, 41-47 (2005).
- <sup>114</sup>J. C. Debsikdar, "Preparation of Transparent Non-Crystalline Stoichiometric Magnesium Aluminate Gel-Monolith by the Sol-Gel Process," *Journal of Materials Science*, 20[12] 4454-4458 (1985).
- <sup>115</sup>I. Ganesh, R. Johnson, G. Rao, Y. Mahajan, S. Madavendra, and B. Reddy, "Microwave-Assisted Combustion Synthesis of Nanocrystalline MgAl<sub>2</sub>O<sub>4</sub> Spinel Powder," *Ceramics International*, 31[1] 67-74 (2005).
- <sup>116</sup>O. Gromov, E. Tikhomirova, E. Lokshin, and V. Kalinnikov, "Synthesis of Magnesium Aluminum Spinel from Carbonate Hydroxyde Precursors," *Russian Journal of Applied Chemistry*, 85[1] 20-24 (2012).
- <sup>117</sup>Z. Nakagawa, "Characterization and sinterability of Mg-Al spinel powders prepared with a thermal decomposition of a freeze-dried sulphate," *J. Ceram. Soc. Jap.*, 90[1042] 313 (1982).
- <sup>118</sup>Y.-M. Chiang and W. D. Kingery, "Grain-Boundary Migration in Nonstoichiometric Solid Solutions of Magnesium Aluminate Spinel: II, Effects of Grain-Boundary Nonstoichiometry," *Journal of the American Ceramic Society*, 73[5] 1153-1158 (1990).
- <sup>119</sup>V. A. Hackley and C. F. Ferraris, "The Use of Nomenclature in Dispersion Science and Technology," Vol. 960. US Department of Commerce, Technology Administration, National Institute of Standards and Technology, (2001).
- <sup>120</sup>F. W. Dynys and J. W. Halloran, "Compaction of Aggregated Alumina Powder," *Journal of the American Ceramic Society*, 66[9] 655-659 (1983).
- <sup>121</sup>F. W. Dynys and J. W. Halloran, "Influence of Aggregates on Sintering," *Journal of the American Ceramic Society*, 67[9] 596-601 (1984).

- <sup>122</sup>H. E. Exner and C. Müller, "Particle Rearrangement and Pore Space Coarsening During Solid-State Sintering," *Journal of the American Ceramic Society*, 92[7] 1384-1390 (2009).
- <sup>123</sup>D. R. Dinger and J. E. Funk, "Particle-Packing Phenomena and Their Application in Materials Processing," *MRS Bulletin*, 22[12] 19-23 (1997).
- <sup>124</sup>Baikowski, "Technical Information Product Code S30CR," [http://www.baikowski.com/upload/produit/fichier\\_66.pdf](http://www.baikowski.com/upload/produit/fichier_66.pdf) (2009).
- <sup>125</sup>Ceralox, "CERALOX® AHPA Magnesium Aluminate Spinel," <http://www.ceralox.com/documents/pdf/TDS-AHPA-Spinel.pdf> (2011).
- <sup>126</sup>R. J. Brook, "Fabrication Principles for the Production of Ceramics With Superior Mechanical Properties," *Proceedings of the British Ceramic Society*, 32[3] 7-24 (1982).
- <sup>127</sup>J. B. Wachtman, W. R. Cannon, and M. J. Matthewson, "Mechanical Properties of Ceramics." John Wiley & Sons, (2009).
- <sup>128</sup>A. A. Griffith, "VI. The Phenomena of Rupture and Flow in Solids," *Philosophical Transactions of the Royal Society of London. Series A*, 221 163-198 (1920).
- <sup>129</sup>R. L. Coble, "Sintering Crystalline Solids. I. Intermediate and Final State Diffusion Models," *Journal of Applied Physics*, 32 787-792 (1961).
- <sup>130</sup>R. L. Coble, "Sintering Crystalline Solids. II. Experimental Test of Diffusion Models in Powder Compacts," *Journal of Applied Physics*, 32[5] 793-799 (1961).
- <sup>131</sup>K. Rozenburg, I. Reimanis, H. J. Kleebe, and R. L. Cook, "Chemical Interaction between LiF and MgAl<sub>2</sub>O<sub>4</sub> Spinel During Sintering," *Journal of the American Ceramic Society*, 90[7] 2038-2042 (2007).
- <sup>132</sup>K. W. White and G. P. Kelkar, "Fracture Mechanisms of a Coarse-Grained, Transparent MgAl<sub>2</sub>O<sub>4</sub> at Elevated Temperatures," *Journal of the American Ceramic Society*, 75[12] 3440-3444 (1992).
- <sup>133</sup>R. E. Carter, "Mechanism of Solid-state Reaction Between Magnesium Oxide and Aluminum Oxide and Between Magnesium Oxide and Ferric Oxide," *Journal of the American Ceramic Society*, 44[3] 116-120 (1961).
- <sup>134</sup>G. A. Gilde, P. J. Patel, and M. Patterson, "Comparison of Hot-Pressing, Rate-Controlled Sintering, and Microwave Sintering of Magnesium Aluminate for Optical Applications," *Society of Photo-Optical Instrumentation Engineers (SPIE) Conference Series*, 3705, 94-104 (1999).
- <sup>135</sup>P. M. C. Lacey, "Developments in the Theory of Particle Mixing," *Journal of Applied Chemistry*, 4[5] 257-268 (1954).

- <sup>136</sup>A. Nienow, M. F. Edwards, and N. Harnby, "Mixing in the Process Industries." Butterworth-Heinemann, (1997).
- <sup>137</sup>B. H. Kaye, "Powder Mixing," Vol. 10. Springer, (1997).
- <sup>138</sup>B. Kaye, "Microencapsulation: The Creation of Synthetic Fine Particles with Specified Properties," *KONA Powder and Particle Journal*, 10[0] 65-82 (1992).
- <sup>139</sup>J. Moon, H. Lee, J. Kim, G. Kim, D. Lee, and H. Lee, "Preparation of ZrO<sub>2</sub>-Coated NiO Powder Using Surface-Induced Coating," *Materials Letters*, 38[3] 214-220 (1999).
- <sup>140</sup>R. Shalliker, L. Rintoul, G. Douglas, and S. Russell, "A Sol-Gel Preparation of Silica Coated Zirconia Microspheres as Chromatographic Support Materials," *Journal of Materials Science*, 32[11] 2949-2955 (1997).
- <sup>141</sup>J. Li, T.-c. Sun, Y. Wang, L.-n. Wang, J.-k. Qu, and T. Qi, "Preparation and Film-Growing Mechanism of Hydrous Zirconia Coated on TiO<sub>2</sub>," *International Journal of Minerals, Metallurgy, and Materials*, 17[5] 660-667 (2010).
- <sup>142</sup>M. Kulig, W. Oroschin, and P. Greil, "Sol-Gel Coating of Silicon Nitride with Mg-Al Oxide Sintering Aid," *Journal of the European Ceramic Society*, 5[4] 209-217 (1989).
- <sup>143</sup>W. Kingery, H. Bowen, and D. Uhlmann, "Introduction to Ceramics," 2nd ed., (1976).
- <sup>144</sup>W. Thomson, "LX. On the equilibrium of vapour at a curved surface of liquid," *The London, Edinburgh, and Dublin Philosophical Magazine and Journal of Science*, 42[282] 448-452 (1871).
- <sup>145</sup>I.-W. Chen and X.-H. Wang, "Sintering Dense Nanocrystalline Ceramics without Final-Stage Grain Growth," *Nature*, 404[6774] 168-171 (2000).
- <sup>146</sup>R. J. Bratton, "Initial Sintering Kinetics of MgAl<sub>2</sub>O<sub>4</sub>," *Journal of the American Ceramic Society*, 52[8] 417-419 (1969).
- <sup>147</sup>R. J. Bratton, "Sintering and Grain-Growth Kinetics of MgAl<sub>2</sub>O<sub>4</sub>," *Journal of the American Ceramic Society*, 54[3] 141-143 (1971).
- <sup>148</sup>Y.-M. Chiang and W. D. Kingery, "Grain-Boundary Migration in Nonstoichiometric Solid Solutions of Magnesium Aluminate Spinel: I, Grain Growth Studies," *Journal of the American Ceramic Society*, 72[2] 271-277 (1989).
- <sup>149</sup>J. Swab, J. Yu, R. Gamble, and S. Kilczewski, "Analysis of the diametral compression method for determining the tensile strength of transparent magnesium aluminate spinel," *International Journal of Fracture*, 172[2] 187-192 (2011).
- <sup>150</sup>A. Goldstein, "Correlation Between MgAl<sub>2</sub>O<sub>4</sub>-Spinel Structure, Processing Factors and Functional Properties of Transparent Parts (Progress Review)," *Journal of the European Ceramic Society*, 32[11] 2869-2886 (2012).

- <sup>151</sup>A. Krell, K. Waetzig, and J. Klimke, "Influence of the Structure of MgO.nAl<sub>2</sub>O<sub>3</sub> Spinel Lattices on Transparent Ceramics Processing and Properties," *Journal of the European Ceramic Society*, 32[11] 2887-2898 (2012).
- <sup>152</sup>W.-K. Li, G.-D. Zhou, and T. Mak, "Advanced Structural Inorganic Chemistry," *Oxford University Press* (2008).
- <sup>153</sup>K. Bodišová, P. Šajgalík, D. Galusek, and P. Švančárek, "Two-Stage Sintering of Alumina with Submicrometer Grain Size," *Journal of the American Ceramic Society*, 90[1] 330-332 (2007).
- <sup>154</sup>K. Madhav Reddy, N. Kumar, and B. Basu, "Innovative multi-stage spark plasma sintering to obtain strong and tough ultrafine-grained ceramics," *Scripta Materialia*, 62[7] 435-438 (2010).
- <sup>155</sup>R. M. German, "A-Z of Powder Metallurgy," 1 ed. Elsevier, (2005).
- <sup>156</sup>K. Tsukuma, "Transparent MgAl<sub>2</sub>O<sub>4</sub> spinel ceramics produced by HIP post-sintering," *Journal of the Ceramic Society of Japan*, 114[10] 802-806 (2006).
- <sup>157</sup>S. Sweeney, M. Brun, T. Yosenick, A. Kebbede, and M. Manoharan, "High-strength transparent spinel with fine, unimodal grain size," *SPIE Defense, Security, and Sensing*, 7302, 73020G (2009).
- <sup>158</sup>A. LaRoche, J. Kutsch, K. Rozenberg, and L. Fehrenbacher, "Manufacturing Issues for Polycrystalline Transparent Spinel Domes," *SPIE Defense, Security, and Sensing*, 7302, 73020D (2009).
- <sup>159</sup>F. Béclin, J. Crampon, R. Duclos, and F. Valin, "Development of Microstructure in Hot Isostatically Pressed MgO. Al<sub>2</sub>O<sub>3</sub> Spinel," *Materials Science and Engineering: A*, 215[1] 164-167 (1996).
- <sup>160</sup>K. Inoue, "Electric-Discharge Sintering," *US Patent* No. 3241956 (1966).
- <sup>161</sup>K. Inoue, "Apparatus for Electrically Sintering Discrete Bodies," *US Patent* No. 3250892 (1966).
- <sup>162</sup>G. F. Taylor, "Apparatus For Making Hard Metal Compositions," *US Patent*, No. 1896854 (1933).
- <sup>163</sup>K. Yamazaki, S. Risbud, H. Aoyama, and K. Shoda, "PAS (plasma activated sintering): transient sintering process control for rapid consolidation of powders," *Journal of Materials Processing Technology*, 56[1] 955-965 (1996).
- <sup>164</sup>M. Tokita, "Mechanism of spark plasma sintering," *Proc. of the Inter. Sympo. on Microwave, Plasma and Thermochemical Processing of Advanced Materials*, S. Miyake and M. Samandi ed., Osaka Japan, JWRI Osaka University, 69-76 (1997).

- <sup>165</sup>V. Mamedov, "Spark plasma sintering as advanced PM sintering method," *Powder Metallurgy*, 45[4] 322-328 (2002).
- <sup>166</sup>W. Yucheng and F. Zhengyi, "Study of temperature field in spark plasma sintering," *Materials Science and Engineering: B*, 90[1] 34-37 (2002).
- <sup>167</sup>Z. Munir, U. Anselmi-Tamburini, and M. Ohyanagi, "The effect of electric field and pressure on the synthesis and consolidation of materials: A review of the spark plasma sintering method," *Journal of Materials Science*, 41[3] 763-777 (2006).
- <sup>168</sup>R. Chaim, "Densification Mechanisms in Spark Plasma Sintering of Nanocrystalline Ceramics," *Materials Science and Engineering: A*, 443[1] 25-32 (2007).
- <sup>169</sup>R. Aalund, "Spark Plasma Sintering," *Ceramic Industry* (2008).
- <sup>170</sup>Y. Furuya, R. Watanabe, H. Yaguchi, M. Saito, T. Kubo, T. Abe, and M. Omori, "Preparation of Smart Composites by SPS," pp. 42-45 in Proceedings of the Third Symposium on Spark Plasma Sintering, Kure, Japan.
- <sup>171</sup>Z. Shen, M. Johnsson, Z. Zhao, and M. Nygren, "Spark Plasma Sintering of Alumina," *Journal of the American Ceramic Society*, 85[8] 1921-1927 (2002).
- <sup>172</sup>D. M. Hulbert, A. Anders, J. Andersson, E. J. Lavernia, and A. K. Mukherjee, "A Discussion on the Absence of Plasma in Spark Plasma Sintering," *Scripta Materialia*, 60[10] 835-838 (2009).
- <sup>173</sup>W. Chen, U. Anselmi-Tamburini, J. Garay, J. Groza, and Z. A. Munir, "Fundamental Investigations on the Spark Plasma Sintering/Synthesis process: I. Effect of DC Pulsing on Reactivity," *Materials Science and Engineering: A*, 394[1] 132-138 (2005).
- <sup>174</sup>U. Anselmi-Tamburini, S. Gennari, J. E. Garay, and Z. A. Munir, "Fundamental Investigations on the Spark Plasma Sintering/Synthesis Process: II. Modeling of Current and Temperature Distributions," *Materials Science and Engineering: A*, 394[1-2] 139-148 (2005).
- <sup>175</sup>U. Anselmi-Tamburini, J. E. Garay, and Z. A. Munir, "Fundamental Investigations on the Spark Plasma Sintering/Synthesis Process: III. Current Effect on Reactivity," *Materials Science and Engineering: A*, 407[1-2] 24-30 (2005).
- <sup>176</sup>K. Morita, B.-N. Kim, K. Hiraga, and H. Yoshida, "Fabrication of high-strength transparent MgAl<sub>2</sub>O<sub>4</sub> spinel polycrystals by optimizing spark-plasma-sintering conditions," *J. Mater. Res.*, 24[9] 2863-2872 (2009).
- <sup>177</sup>M. Omori, "Sintering, Consolidation, Reaction and Crystal Growth by the Spark Plasma System (SPS)," *Materials Science and Engineering: A*, 287[2] 183-188 (2000).
- <sup>178</sup>J. F. Li, K. Wang, B. P. Zhang, and L. M. Zhang, "Ferroelectric and Piezoelectric Properties of Fine-Grained Na<sub>0.5</sub>K<sub>0.5</sub>NbO<sub>3</sub> Lead-Free Piezoelectric Ceramics Prepared

by Spark Plasma Sintering," *Journal of the American Ceramic Society*, 89[2] 706-709 (2006).

<sup>179</sup>T. Wada, K. Tsuji, T. Saito, and Y. Matsuo, "Ferroelectric NaNbO<sub>3</sub> Ceramics Fabricated by Spark Plasma Sintering," *Japanese journal of applied physics*, 42[9S] 6110 (2003).

<sup>180</sup>U. Anselmi-Tamburini, J. N. Woolman, and Z. A. Munir, "Transparent Nanometric Cubic and Tetragonal Zirconia Obtained by High-Pressure Pulsed Electric Current Sintering," *Advanced Functional Materials*, 17[16] 3267-3273 (2007).

<sup>181</sup>A. LaReoche, K. Rzenburg, J. Voyles, L. Fehrenbacher, and G. Gilde, "An Economic Comparison of Hot Pressing vs. Pressureless Sintering for Transparent Spinel Armor," *Advances in Ceramic Armor—IV, Ceramic Engineering and Science Proceedings*, 29[6] 55-62 (2009).

<sup>182</sup>K. Brower, J. C. Oxley, and M. Tewari, "Evidence for Homolytic Decomposition of Ammonium Nitrate at High Temperature," *The Journal of Physical Chemistry*, 93[10] 4029-4033 (1989).

<sup>183</sup>I. McCave, R. Bryant, H. Cook, and C. Coughanowr, "Evaluation of a Laser-Diffraction-Size Analyzer for Use with Natural Sediments," *Journal of Sedimentary Research*, 56[4] (1986).

<sup>184</sup>A. S. A. B.-. 13, "Standard Test Methods for Density of Compacted or Sintered Powder Metallurgy (PM) Products Using Archimedes' Principle," *ASTM International, West Conshohocken, PA* (2013).

<sup>185</sup>B. C. Smith, "Fundamentals of Fourier Transform Infrared Spectroscopy." CRC Press, (2009).

<sup>186</sup>M. Winterer, "Nanocrystalline Ceramics: Synthesis and Structure," Vol. 53. Springer, (2002).

<sup>187</sup>M. I. Mendelson, "Average Grain Size in Polycrystalline Ceramics," *Journal of the American Ceramic Society*, 52[8] 443-446 (1969).

<sup>188</sup>A. S. C.-. 13, "Test Method for Knoop Indentation Hardness of Advanced Ceramics," *ASTM International, West Conshohocken, PA* (2013).

<sup>189</sup>A. S. A. E.-. 11e1, "Test Method for Knoop and Vickers Hardness of Materials," *ASTM International, West Conshohocken, PA* (2012).

<sup>190</sup>A. E. Brown, "Rationale and Summary of Methods for Determining Ultrasonic Properties of Materials at Lawrence Livermore National Laboratory," *Lawrence Livermore National Laboratory* (1997).

<sup>191</sup>J. Luo, S. Adak, and R. Stevens, "Microstructure Evolution and Grain Growth in the Sintering of 3Y-TZP Ceramics," *Journal of Materials Science*, 33[22] 5301-5309 (1998).

- <sup>192</sup>A. S. B.-. 13, "Test Method for Density of Powder Metallurgy (PM) Materials Containing Less Than Two Percent Porosity," *ASTM International, West Conshohocken, PA* (2013).
- <sup>193</sup>A. S.-. 13, "Standard Test Methods for Determining Average Grain Size," *ASTM International, West Conshohocken, PA* (2013).
- <sup>194</sup>P. Kloczek, "Handbook of Infrared Optical Materials." CRC Press, (1991).
- <sup>195</sup>W. Tyler and A. Wilson Jr, "Thermal Conductivity, Electrical Resistivity, and Thermoelectric Power of Graphite," *Physical Review*, 89[4] 870 (1953).
- <sup>196</sup>R. Taylor, K. Gilchrist, and L. Poston, "Thermal Conductivity of Polycrystalline Graphite," *Carbon*, 6[4] 537-544 (1968).
- <sup>197</sup>C. Uher, "4.3. 2 Temperature Dependence of Thermal Conductivity of Graphite," pp. 430-439. in *Thermal Conductivity of Pure Metals and Alloys*. Springer, 1991.
- <sup>198</sup>J. S. Yoo, A. A. Bhattacharyya, and C. A. Radlowski, "De-SO<sub>x</sub> Catalyst: An XRD Study of Magnesium Aluminate Spinel and Its Solid Solutions," *Industrial & Engineering Chemistry Research*, 30[7] 1444-1448 (1991).
- <sup>199</sup>A. Fick, "V. On Liquid Diffusion," *The London, Edinburgh, and Dublin Philosophical Magazine and Journal of Science*, 10[63] 30-39 (1855).
- <sup>200</sup>J. Narayan, R. Weeks, and E. Sonder, "Aggregation of Defects and Thermal-Electric Breakdown in MgO," *Journal of Applied Physics*, 49[12] 5977-5981 (1978).
- <sup>201</sup>W. D. Kingery, "Plausible Concepts Necessary and Sufficient for Interpretation of Ceramic Grain-Boundary Phenomena: I, Grain-Boundary Characteristics, Structure, and Electrostatic Potential," *Journal of the American Ceramic Society*, 57[1] 1-8 (1974).
- <sup>202</sup>W. D. Kingery, "Plausible Concepts Necessary and Sufficient for Interpretation of Ceramic Grain-Boundary Phenomena: II, Solute Segregation, Grain-Boundary Diffusion, and General Discussion\*," *Journal of the American Ceramic Society*, 57[2] 74-83 (1974).
- <sup>203</sup>E. Van Cappellen and J. C. Doukhan, "Quantitative Transmission X-ray Microanalysis of Ionic Compounds," *Ultramicroscopy*, 53[4] 343-349 (1994).
- <sup>204</sup>G. Cliff and G. Lorimer, "The Quantitative Analysis of Thin Specimens," *Journal of Microscopy*, 103[2] 203-207 (1975).
- <sup>205</sup>K. Maca, M. Trunec, and R. Chmelik, "Processing and Properties of Fine-Grained Transparent MgAl<sub>2</sub>O<sub>4</sub> Ceramics," *Ceramics Silikaty*, 51[2] 94 (2007).
- <sup>206</sup>A. Chopelas and A. M. Hofmeister, "Vibrational Spectroscopy of Aluminate Spinel at 1 atm and of MgAl<sub>2</sub>O<sub>4</sub> to over 200 kbar," *Physics and Chemistry of Minerals*, 18[5] 279-293 (1991).